

Melt growth of oxide single crystals in controlled oxygen fugacity atmosphere

vorgelegt von
Diplom-Physiker Steffen Ganschow
geboren in Lutherstadt Wittenberg

von der Fakultät II - Mathematik und Naturwissenschaften
der Technischen Universität Berlin
zur Erlangung des akademischen Grades

Doktor der Naturwissenschaften
– Dr. rer. nat. –

genehmigte Dissertation

Promotionsausschuss:

Vorsitzender:	Prof. Dr. Thomas Friedrich
Gutachter:	Prof. Dr.-Ing. Matthias Bickermann
Gutachter:	Prof. Dr. Martin Lerch
Gutachter:	PD Dr. habil. Detlef Klimm

Tag der wissenschaftlichen Aussprache: 3. September 2015

Berlin 2015

Contents

1	Introduction	1
2	Thermodynamic background	7
2.1	Redox equilibria and predominance diagrams	7
2.2	Crucible materials	12
2.3	Growth atmospheres	14
3	Crystal growth from the melt	21
3.1	The Bridgman-Stockbarger technique	21
3.2	The Czochralski technique	22
3.3	The micro-pulling-down technique	24
3.4	Selected issues of melt growth of oxides	25
3.4.1	Transport of heat through the growing crystal	25
3.4.2	Transport of heat and matter in the fluid phase	28
3.4.3	Melt convection and interface flip in Czochralski pulling	29
3.4.4	Solute segregation and morphological stability	31
3.5	Comparison of growth techniques	40
4	Growth and characterization of wüstite crystals	43
4.1	The Fe–O system	44
4.2	Thermal analysis	47
4.2.1	Decomposition of iron oxalate	47
4.2.2	Melting of ferrous oxide	48
4.3	Crystal growth	49
4.4	Characterization by X-ray diffraction	51
4.5	Eutectoid decomposition of wüstite	55

4.6	Conclusions	60
5	Chromium distribution coefficient in ruby crystals	63
5.1	Phase diagram and chromium equilibrium distribution coefficient . . .	64
5.2	Experimental procedure	70
5.2.1	Crystal growth	70
5.2.2	Determination of chromium concentration	72
5.3	Chromium distribution coefficient and macrosegregation	75
5.4	Growth rate dependence of the effective distribution coefficient	77
5.5	Deviation from steady growth – formation of growth bands	82
5.6	Conclusions	88
6	Melt growth of zinc oxide	89
6.1	Zn–O and Ir–O predominance diagrams	92
6.2	Bridgman growth of ZnO	92
6.3	Alloying with Mg	96
6.4	Conclusions	98
7	Summary	101
	Bibliography	103

1 Introduction

Nonstoichiometry is a common phenomenon in crystalline solids often vitally determining their physical properties. In normal ambient conditions nonstoichiometry of metal oxides is often very small and hardly detectable. Situation may change with increasing temperature approaching the melting point of the regarded substance when the entropic contribution to the Gibbs energy becomes significant. However, some oxides of metals occurring in different oxidation states, among them oxides of transition and rare-earth metals, show considerable nonstoichiometry already at much lower temperature. Dependent on oxygen fugacity of the ambient those metals usually can form a number of oxides with different stoichiometries, structures, and properties. E.g. in the system iron–oxygen several solid oxides are known, FeO (wüstite), Fe₃O₄ (magnetite), and Fe₂O₃ (hematite = α -Fe₂O₃ or maghemite = γ -Fe₂O₃). Wüstite is antiferromagnetic and has a very wide existence range that at normal pressure does not cover the stoichiometric composition. Wüstite is thermodynamically stable only at elevated temperature, at 561°C it decomposes in a peritectoid reaction into iron (α -Fe) and magnetite. Growth issues of wüstite are discussed in Part 4 of this treatise. Magnetite and hematite are main constituents of iron ores and the major source of iron for steel industry, whereas maghemite, widely used for magnetic recording, is formed by oxidation of magnetite at temperatures below approximately 250°C.

In multinary oxides antisite defects can occur when cations of different type exchange positions. An extensively studied example is lithium niobate LiNbO₃ where some of the Nb⁵⁺ ions, ideally found in the center of oxygen octahedra, occupy lithium sites located at the faces of those octahedra [173]. The excess charge of a Nb⁵⁺ ion is compensated by four vacancies on lithium sites. As a result, the compound is lithium deficient, and its congruently melting composition is at 48.5 mol% Li₂O. This type of nonstoichiometry can be controlled—at least to some degree—by

the balance of the constituting metal oxides rather than by oxygen fugacity and shall not be considered in this work.

For predominantly ionic crystals like oxides the concept of stoichiometry implies the existence of cations and anions forming the crystal lattice mainly due to electrostatic forces. The total charge of the cations is compensated by the appropriate amount of anions, so that the ratio of the respective element concentrations is a rational number, e.g. $[\text{Al}^{3+}]/[\text{O}^{2-}] = 2/3$ for aluminum oxide, also expressed by the commonly used integer formulas, e.g. Al_2O_3 . Such an ideal stoichiometry relation may hold at low temperature where the large enthalpy of formation of point defects ΔH_f , usually of the order of electronvolts (or hundreds kJ/mol), efficiently opposes creation of defects. At higher temperature the entropic contribution to the Gibbs energy becomes more significant. The equilibrium concentration of isolated, non-interacting defects is proportional to $\exp\left(-\frac{\Delta H_f}{2kT}\right)$ with the Boltzmann constant k and the absolute temperature T . Although still very low even at elevated temperature, of the order of one defect per million lattice sites for Schottky defects in oxides at 1000°C , point defects take tremendous effect on some materials properties. Besides introducing additional energy levels in the band gap leading to thermally activated electron conductivity and coloration due to additional absorption usually in the visible spectral range (color centers), mainly transport properties are affected in which vacancies and interstitial atoms (ions) with increased mobility enhance diffusion processes. Practical applications of such behavior reach from the various types of semiconductor and optoelectronic devices to gas sensors and solid electrolytes e.g. in fuel cells.

Some transition metal oxides exhibit extraordinarily large deviations from stoichiometry. For iron-deficient wüstite, Fe_{1-x}O , the maximum deviation was found to be $x \approx 0.17$. Every vacancy in the cation sublattice is compensated by two interstitial Fe^{3+} so that there is more than one defect per regularly occupied lattice site. At such high defect concentrations it is more than likely that the defects are not longer isolated but start to interact forming complexes, e.g. Roth or Koch-Cohen clusters. An exothermic contribution to the Gibbs energy of the systems results from Coulomb forces between the charges of defects.

Naturally, in case of oxides the fugacity of oxygen p_{O_2} is the control governing nonstoichiometry and properties of involved compounds, as well as the behavior

of the system in its entirety. In the quoted example, Fe_2O_3 will be stable at high oxygen fugacity (vigorous oxidizing conditions). With decreasing p_{O_2} the other oxides, Fe_3O_4 and FeO will appear and disappear progressively until the stability region of metallic iron is entered for $p_{\text{O}_2} < 10^{-15}$ bar at 1000°C . However, in crystal growth literature stoichiometry discussion often is provided with the implicit understanding that oxygen stoichiometry of the regarded compound is ideal and the atmosphere appropriate to stabilize the desired phases, oxides and metal crucibles etc. Such atmosphere is usually termed “inert”. But already in one of the very first reports on melt growth of a binary oxide, CaWO_4 [114], the authors suggest that a “slight discoloration” of the crystals originated from “limited access of atmospheric oxygen” during growth and could be easily removed by post-growth annealing. It was also observed that addition of tiny amounts of oxygen to the growth atmosphere was able to suppress the formation of suboxides and reduce the density of Tyndall scatterers during growth of sapphire and ruby [42, 43]. The growth of $\text{Gd}_3\text{Ga}_5\text{O}_{12}$ (GGG) required more accurate adjustment of the atmosphere. At very low oxygen fugacity gallium suboxide is formed according to $\text{Ga}_2\text{O}_3 \rightleftharpoons \text{Ga}_2\text{O} + \text{O}_2$. Excessive evaporation of Ga_2O shifts melt composition and recondensation of Ga_2O on the hot surface of the growing crystals leads to formation of eutectic corroding the crystal and eventually violating the dynamic equilibrium at the three phase point melt-crystal-gas. Oxidizing atmosphere, in contrast, involves oxidation of iridium at the crucible surface. Iridium oxide is solved in the melt and eventually transported to the interface. When incorporated into the growing crystal iridium precipitations occur. An inert atmosphere of Ar or N_2 with addition of approximately 2% oxygen was found a good compromise in many cases [41, 31].

This treatise concatenates three different studies on melt growth of selected oxide materials. In the quoted cases the constituting metal oxides show a more or less limited existence range and growth atmosphere must be adjusted to fit this existence range over a wide temperature range spanning from approximately 500°C to the melting temperature of the considered compound. In this context often the ambiguous term “reactive atmosphere” is used in crystal growth literature. In fact, in most situations rather a really inert atmosphere, i.e. an atmosphere that does not change the oxidation state of any of the involved bodies (melt, crystal, construction parts etc.) or their constituent is sought.

Part 2 is a brief introduction of the thermodynamic basis of calculation of predominance diagrams extensively used throughout the treatise. Here it is assumed that the gas phase behaves ideally and that chemical reactions in the gas phase proceed at such high velocity that equilibrium is attained instantaneously. The first assumption appears reasonable since standard crystal growth conditions are far away from the critical point so that the ambient obeys the universal gas law. The numerical treatment essentially consists of solving sets of equations for the minimization of the Gibbs energy of the regarded system. Comprehensive thermodynamic databases allow to perform the necessary calculations offhand in very short time using a standard PC. The application range of some common crucible materials and gas mixtures will be calculated. Part 3 addresses crystal growth techniques used in the experiments and some major issues occurring during crystal growth from the melt. Experimental findings are discussed in parts 4 through 6 introducing melt growth of wüstite (FeO), ruby (Cr:Al₂O₃), and ZnO, respectively.

Melt growth of wüstite single crystals for reasons explained above bears two major challenges. First, oxygen fugacity must be controlled inside a narrow band during the entire growth process. That is additionally complicated by the fact that already grown parts of the crystal being at significantly lower temperature require a several orders of magnitude lower oxygen fugacity than the melt and parts near the interface that are at temperatures only slightly below the melting temperature. Second, the grown crystals must be cooled down, specifically when crossing the eutectoid temperature, very fast to avoid decomposition. In this work, an atmosphere containing CO₂ and CO in an appropriate molar ratio fitting the stability region of FeO over a wide temperature range was employed during pulling down of small-size crystals in steep temperature gradient conditions with very high velocity exceeding 10 mm/min.

During melt growth of ruby, chromium segregation can be reversed by adequate selection of the growth atmosphere. In an oxidizing atmosphere, chromium(III) oxide is the prevailing chromium oxide species in the melt but with degressive oxygen fugacity the share of chromium(II) oxide increases significantly. While Cr₂O₃ is preferentially incorporated into ruby with a distribution coefficient $k_{\text{Cr}_2\text{O}_3} > 1$, CrO is practically not incorporated at all, i.e. $k_{\text{CrO}} \ll 1$. During growth, the melt is depleted in Cr₂O₃ but enriched in CrO. An appropriate atmosphere can control

the fractions of both oxides in such a way that the rates of enrichment and depletion mutually compensate. The result is an effective distribution coefficient of chromium equal unity yielding crystals of extraordinary homogeneous micro- and macrodistribution.

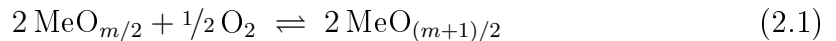
The last part of this treatise is focused on the feasibility of ZnO crystal growth from the melt. The high melting temperature of nearly 2000°C and thermal decomposition upon heating prevent crystal pulling following the standard procedure. According to a common acceptance, there is no metal crucible material available that would withstand the extremely aggressive conditions—high temperature and oxygen fugacity—at the melting point of zinc oxide. Accurate thermodynamic calculations suggest, however, compatibility of iridium with those conditions. This result was confirmed experimentally by melting and crystallizing ZnO in cylindrical iridium crucibles heated inductively. Severe evaporation from the ZnO melt greatly prevents visual feedback and hampers growth at the free melt surface, e.g. by a Czochralski pulling process. Using a Bridgman configuration ZnO crystals with diameters of up to 33 mm could be grown. Despite thermo-mechanical stress caused by the intimate contact between growing crystal and the crucible, crystalline perfection of the grown crystals was close to that reported for hydrothermally grown material.

2 Thermodynamic background

Melt growth of oxide single crystals usually entails high temperatures above 1000°C and low growth velocities. It appears reasonable to assume that under such conditions chemical reactions in the involved fluid phases are in equilibrium state at any instant of time. This assumption is substantiated by comparison of typical velocities of particles or control volumes. The mean speed of a gas molecule is of the order of km/s, and the typical velocity of the fluid flow is of the order of cm/s. Both are by several orders of magnitude larger than the typical growth velocity which is of the order of mm/h.

2.1 Redox equilibria and predominance diagrams

Oxidation and reduction of a metal oxide $\text{MeO}_{m/2}$ is governed by the redox equilibrium



with m denoting the formal oxidation number, i.e. the number of electrons per atom given off by the metal. The change in Gibbs energy associated with that reaction can be expressed as

$$\Delta G = \Delta G^\circ + RT \ln Q \quad (2.2)$$

where ΔG° is the standard Gibbs energy change and $Q = \prod_i a_i^{\nu_i}$ the reaction quotient, a_i denotes the activity of component i , and ν_i its stoichiometry coefficient in the reaction formula. Depending on the sign of ΔG the forward reaction ($\Delta G < 0$) or the reverse reaction ($\Delta G > 0$) will proceed spontaneously. Equilibrium is attained at $\Delta G = 0$ and the corresponding reaction quotient is the equilibrium constant $K = Q_{\text{eq}}$. If the involved condensed phases are pure phases then their activities *per*

definitionem are equal $a_i = 1$. Typical melt growth processes for oxides proceed at pressure-temperature conditions far from the critical point of most commonly employed gases. The growth atmosphere can therefore be regarded as an ideal gas and the activities of species are given by their partial pressures. The equilibrium constant for reaction (2.1) becomes

$$K = (p_{O_2}^*)^{1/2} \quad (2.3)$$

where the asterisk denotes the equilibrium value. From the definition of Gibbs energy follows that

$$\Delta G^\circ = \Delta H^\circ - T\Delta S^\circ. \quad (2.4)$$

Here, ΔH° and ΔS° denote the standard reaction enthalpy and entropy of reaction, respectively, both only weakly depending on temperature. Typical standard Gibbs energy curves for equilibria (2.1) are therefore nearly straight lines with kinks at phase transitions where molar heat capacities of the involved phases change abruptly. Fig. 2.1 exemplarily compares the standard Gibbs energy for the equilibrium between aluminum and aluminum oxide calculated (i) from the room temperature values of enthalpy and entropy, $\Delta G^\circ(T) = \Delta H^\circ(298 \text{ K}) + T \cdot \Delta S^\circ(298 \text{ K})$, represented by the straight line in the figure, and (ii) using the temperature-dependent values, $\Delta G^\circ(T) = \Delta H^\circ(T) + T \cdot \Delta S^\circ(T)$ (black dots). The deviation of the simplified (i) from the more precise calculation (ii) is less than 2% in the whole temperature range from room temperature to beyond 2500°C and appears tolerable in most cases.

A major contribution to the standard entropy of reaction (2.1) arises from the entropy of gaseous oxygen “consumed” during the reaction. The standard entropies of the involved condensed phases instead usually do not differ that much, so that their difference becomes small compared to the former. As a result, the slopes of $\Delta G^\circ(T)$ curves are similar for most metals/metal oxides but vary significantly in their location along the energy axis determined by the standard enthalpy at room temperature, $\Delta H^\circ(298 \text{ K})$. For the same reasoning, the standard entropy of reaction (2.1) is negative and the standard Gibbs energy therefore increases with temperature. Hence, the entropic contribution to ΔG° is responsible for the reduced stability of metal oxides at elevated temperature.

In extraction metallurgy plots of $\Delta G^\circ(T)$ are known as Ellingham diagrams. To avoid calculating the equilibrium oxygen fugacity according to

$$\ln(p_{\text{O}_2}^*/\text{bar}) = -\frac{2\Delta G^\circ}{RT} \quad (2.5)$$

for each value of ΔG° , often a nomographic scale is added to the Ellingham diagram. The other way around, scaling the ordinate of an Ellingham diagram by $2/RT$ leads to the same result and $p_{\text{O}_2}^*$ can be read directly from the y -axis. Ellingham diagrams can be calculated either manually from tabulated (e.g. [13]) values ΔH° and ΔS° or using appropriate software packages, e.g. [11, 10, 6] usually coming with extensive thermodynamic databases. Fig. 2.2 exemplarily shows the calculated predominance diagram of the Cu–O system. At melting of one of the involved condensed phases (marked by hollow dots in the figure) slope of the $\Delta G^\circ(T)$ curve changes because at phase transitions points difference in entropies between products and reactants changes abruptly.

For a regarded Me–O system, $p_{\text{O}_2}^*(T)$ curves for redox equilibria (2.1) involving consecutive oxidation states of the metal divide the whole (p_{O_2}, T) phase space into predominance domains. Within each domain p_{O_2} and T can be changed without changing the oxidation state of the metal. If, however, a $p_{\text{O}_2}^*(T)$ line is passed then either the reduction or oxidation reaction will proceed and $\text{MeO}_{(m-1)/2}$, respectively $\text{MeO}_{(m+1)/2}$ will be formed. Hence, to retain a desired oxidation state of metal Me, oxygen fugacity of the ambient must be tuned inside the corresponding predominance field for all temperatures, at least in thermal equilibrium.

If the system contains more than one metal then the above treatment is still a good approximation since the Gibbs energy change associated with the formation of compounds (e.g. solid solutions or intermediate phases) from the oxides is small compared to the change upon forming the oxides from the elements. For illustration, in Tab. 2.1 calculated values of the total Gibbs energy of the system $0.99 \text{ Al}_2\text{O}_3 + 0.01 \text{ Ti}_2\text{O}_3$ (Ti-doped sapphire) just below the melting temperature of Al_2O_3 are listed. The contribution that arises from formation of oxides is about 1000 times larger than that associated with the formation of a solid solution from the oxides and is therefore decisive for location of the corresponding redox equilibria.

According to Hess’s law of constant heat summation, from thermodynamic data

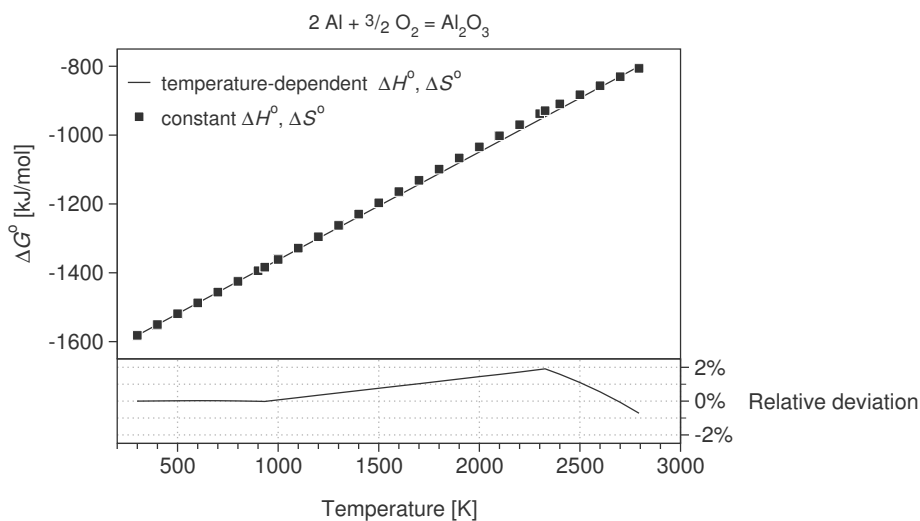
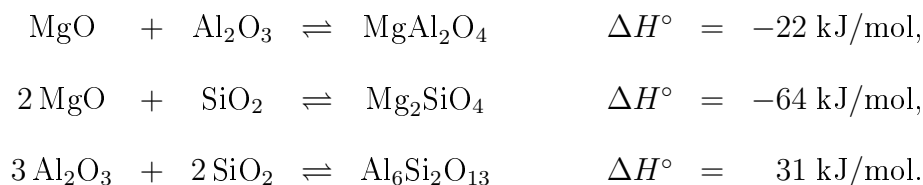


Figure 2.1: Standard Gibbs energy curves for the equilibrium $2 \text{ Al} + \frac{3}{2} \text{ O}_2 \rightleftharpoons \text{ Al}_2\text{O}_3$ calculated in different ways. Dots represent values calculated using the temperature-dependent values of the standard enthalpy and entropy. The solid line depicts $\Delta G^\circ(T)$ calculated from the room temperature values of standard reaction enthalpy and entropy.

of metal oxides and some well-known intermediate compounds in the ternary system $\text{Al}_2\text{O}_3\text{--MgO--SiO}_2$ (Tab. 2.2) the standard enthalpy of formation of these compounds from the oxides can be calculated



Again, these are small compared to the standard enthalpies of formation of the oxides from the elements. Therefore, for compounds consisting of two or more metal oxides, stability discussion can be reduced to the stability discussion of the contributing oxides.

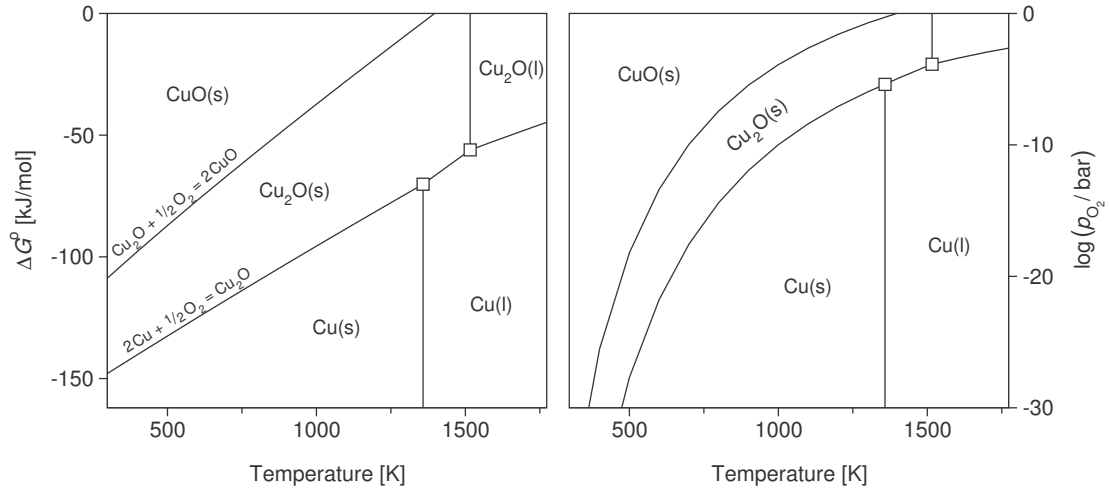


Figure 2.2: Calculated predominance diagram of the system Cu–O. Scaling by $2/RT$ translates the $\Delta G^\circ(T)$ diagram into a easy-to-read $p_{\text{O}_2}^*(T)$ diagram (right diagram). Rectangular dots indicate melting of one of the involved condensed phases.

	Gibbs energy [10^6 J/mol]
Pure elements Al, Ti, O	-1.17138
Pure oxides Al_2O_3 , Ti_2O_3	-2.09856
Solid solution $(\text{Al}_{0.99}\text{Ti}_{0.01})_2\text{O}_3$	-2.09953

Table 2.1: Total Gibbs energy of the system $1.98 \text{ Al} + 0.02 \text{ Ti} + 3 \text{ O}$ at 2050°C .

	ΔH° [kJ/mol]
Al ₂ O ₃	-1676
MgO	-601
SiO ₂	-911
MgAl ₂ O ₄ (spinel)	-2299
Mg ₂ SiO ₄ (forsterite)	-2177
Al ₆ Si ₂ O ₁₃ (mullite)	-6819

Table 2.2: Standard enthalpy of formation from elements for some compounds in the system Al₂O₃–MgO–SiO₂ at 25 °C.

2.2 Crucible materials

By far the largest part of single crystals grown on an industrial scale is grown from the melt contained in appropriate containers. That requires availability of a crucible material that is thermally and chemically stable at growth conditions. The crucible material must therefore (i) have a melting temperature higher than the material to be grown, (ii) not be corroded by the melt, and (iii) not react with the growth ambient. For oxides usually involving very high melting temperatures, crucibles made of precious metals have proved most practical. Using the above outlined treatment, the application conditions and ranges of those metals can be easily estimated.

Fig. 2.3 shows calculated predominance diagrams of the most prospective crucible materials for melt growth of oxides, that are platinum (melting temperature $T_m = 1772^\circ\text{C}$), iridium ($T_m = 2466^\circ\text{C}$), and tungsten ($T_m = 3422^\circ\text{C}$). Platinum is the first choice owing to its unequalled oxidation resistivity. Unfortunately, its application range is limited to temperatures $T \lesssim 1500^\circ\text{C}$. Above this temperature platinum becomes soft and the mechanical strength of crucibles and other constructive elements breaks down. For higher working temperatures often crucibles made of iridium are used. However, in oxygen-containing ambient iridium is much less stable than platinum and must be handled with care to avoid oxidation. At $\approx 1100^\circ\text{C}$ the equilibrium oxygen fugacity $p_{\text{O}_2}^*$ over Ir/IrO₂ reaches 10 mbar corresponding to

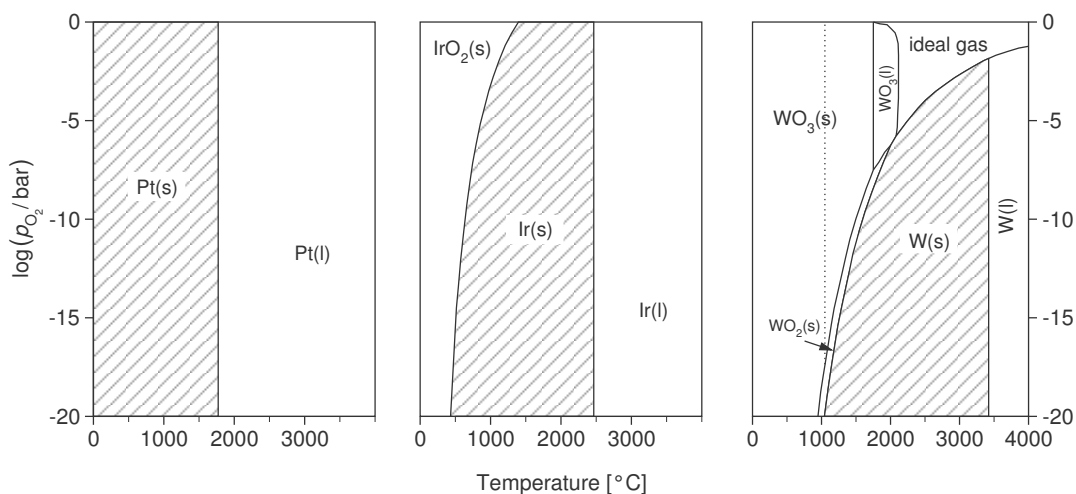


Figure 2.3: Predominance diagram for the systems Pt–O, Ir–O, and W–O. The shaded regions denote the stability range of the pure metals, i.e. the range employable for crystal growth.

1 vol% and around this temperature the danger of oxidation of iridium is greatest. Though at lower temperature $p_{\text{O}_2}^*(T)$ falls very quickly, the reaction is progressively retarded kinetically. One should realize that at room temperature in air the thermodynamically stable phase is IrO₂. With increasing temperature the relative stability of iridium metal increases. Above 1500 $^{\circ}\text{C}$ the predominance field of metallic iridium extends to 1 bar oxygen fugacity so that crucibles can be kept in fairly oxidizing atmosphere at sufficiently high temperature. The upper limit of application range of iridium crucibles is probably marked by rare-earth scandates REScO₃ with melting temperatures up to or slightly exceeding 2200 $^{\circ}\text{C}$ [171]. For even higher temperatures the assortment of suitable crucible materials shrinks dramatically. Thanks to its very high melting temperature often tungsten is employed. However, application of tungsten crucibles is strongly limited to virtually oxygen-free conditions (cf. Fig. 2.3).

2.3 Growth atmospheres

A typical crystal growth process from the melt covers a wide temperature range from room temperature to usually slightly above the melting temperature of the concerned compound. To keep a certain $\text{MeO}_{m/2}$ stable over the whole process, oxygen fugacity must be adjusted to be inside the corresponding predominance region at any temperature. Simple admixture of oxygen to an inert gas, e.g. nitrogen or argon, always results in a virtually temperature-independent oxygen fugacity represented by a horizontal line in the (T, p_{O_2}) predominance diagram. Such ambient can be appropriate only in exceptional cases or/and a relatively narrow temperature range. *In-situ* adjustments of the ambient's composition, e.g. by changing the flow rates of the process gases, are one possible route to generate an ambient with adapted temperature-dependent oxygen fugacity.

During crystal growth, while some parts (e.g. the crucible) are at a temperature near the melting point of the material grown, other parts (e.g. ceramic insulation or a metallic afterheater) may be at substantially lower temperature. Moreover, there may occur significant temperature gradients along the extensions of some constructive parts, e.g. the bottom of an inductively heated crucible is usually at least some 10 degrees colder than the side walls. Also, earlier grown parts of the crystal are at temperatures definitively below the melting temperature, often at temperatures low enough to reach another predominance field but still high enough to facilitate efficient diffusion in the solid. In all these cases, oxygen fugacity resulting from direct admixture of oxygen may be matching for some parts but lead to an unwanted oxidation or reduction of other parts. Alternatively, oxygen content of the gas atmosphere “automatically” increases in the heating-up phase of the growth process by thermal decomposition of e.g. carbon dioxide according to



The equilibrium constant of this reaction is

$$K_p = \frac{p_{\text{CO}} \cdot p_{\text{O}_2}^{1/2}}{p_{\text{CO}_2}}. \quad (2.7)$$

Temperature dependence of K_p can be calculated from the tabulated values of $\Delta G^\circ(T)$ using $K_p(T) = \exp(-\Delta G^\circ/RT)$. With α being the degree of dissociation, i.e. the mole fraction of decomposed CO_2 , and P the total pressure, fugacities of the involved gases equal

$$p_{\text{CO}_2} = \frac{1-\alpha}{1+\alpha/2} P \quad p_{\text{CO}} = \frac{\alpha}{1+\alpha/2} P \quad p_{\text{O}_2} = \frac{\alpha/2}{1+\alpha/2} P. \quad (2.8)$$

Insertion into Eq. 2.7 and transformation leads to

$$K_p^2 = \frac{\alpha^3}{2(1-\alpha)^2(1+\alpha/2)} P.$$

For $\alpha \ll 1$ the degree of dissociation is approximately

$$\alpha \approx \left(\frac{2 K_p^2}{P} \right)^{1/3}.$$

Tab. 2.3 lists calculated values of α for some temperatures. Knowing α , equilibrium fugacities of CO_2 , CO , and O_2 can be calculated using Eqns. 2.8. Composition of equilibrium (2.6) can be adjusted by using a CO_2/CO mixture instead of pure CO_2 . According to Le Chatelier's principle, addition of CO will shift equilibrium (2.6) to the left hand side and will result in a decrease of oxygen fugacity. By adjusting the $\text{CO}_2:\text{CO}$ ratio in the gas inlet, oxygen fugacity at a given temperature can be tuned over a few orders of magnitude (Fig. 2.4). For treatment of gas mixtures, besides reaction (2.6) also decomposition of carbon monoxide according to



has to be taken in to account. However, as can be seen in Fig. 2.4, oxygen fugacity resulting from decomposition of CO is negligibly small and can be discounted when the atmosphere contains significant amounts of CO_2 . At low and moderate temperatures both equilibria are far on the left-hand side resulting in a very low oxygen fugacity. Such behavior is extremely advantageous with respect to the stability diagram of Ir (Fig. 2.3) being the practically most versatile crucible material for application up to and beyond 2000°C . With increasing temperature both equilibria

T/K	500	1000	1500	2000
α	2.6×10^{-17}	1.7×10^{-7}	3.6×10^{-4}	1.6×10^{-2}

Table 2.3: Temperature dependence of the dissociation degree α for equilibrium in Eq. 2.6 at 1 bar total pressure.

shift towards the product side and the p_{O_2} curve of $\text{CO}_2:\text{CO}$ mixture approaches that of pure carbon dioxide. The increasing with temperature oxygen fugacity of such gas mixture counteracts thermal decomposition of metal oxides at high temperature. As will be demonstrated in the later sections, the range of oxygen fugacity that can be realized using CO/CO_2 mixtures is large enough to meet the demands of diverse oxide systems.

The system CO_2/CO is only one example of a convenient growth atmosphere. Selecting appropriate redox pairs, e.g. $\text{H}_2\text{O}/\text{H}_2$ or NO_2/NO , or combinations of redox pairs, the level of oxygen fugacity and slope of the $p_{\text{O}_2}(T)$ curve can be adapted to the specific needs. Limiting aspects may be safety considerations (toxicity, explosiveness) or solubility of species in the melt or present solid phases. The system $\text{H}_2\text{O}/\text{H}_2$ may be of particular interest since the water component can be easily added to pure hydrogen by flowing the gas over a temperature controlled water bath. Fig. 2.5 shows $p_{\text{O}_2}(T)$ curves for different $\text{H}_2\text{O}/\text{H}_2$ mixtures. In practical growth processes, however, the highly water-enriched atmospheres will not be available due to problems of water condensation at temperatures below 100°C . Comparing both systems (Figs. 2.4 and 2.5) it becomes apparent that the advantage of the CO_2/CO system is the wider range of fugacity attainable. $\text{H}_2\text{O}/\text{H}_2$ instead has a stronger temperature dependence and significantly lower oxygen pressure at low temperatures that might be favorable to avoid post-growth oxidation e.g. of transition metals.

Additional benefits that arise from the use of redox pairs as ambient are (i) possibility of attaining very low oxygen fugacity and (ii) resistivity of oxygen fugacity against perturbations or unknown oxygen sources.

Adjusting very low oxygen fugacities, below 10^{-6} bar, by direct injection of oxygen to the growth atmosphere is extremely challenging since it requires flow rates different by orders of magnitude for different types of gases. Residual impurities of available gases, leakage of recipient and installation, and residual gas adsorbed at in-

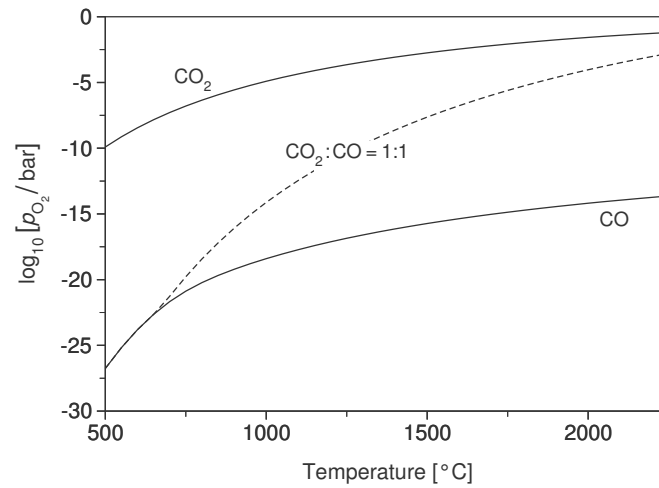


Figure 2.4: Oxygen fugacity of pure CO₂, pure CO, and of a equimolar mixture of both (at room temperature).

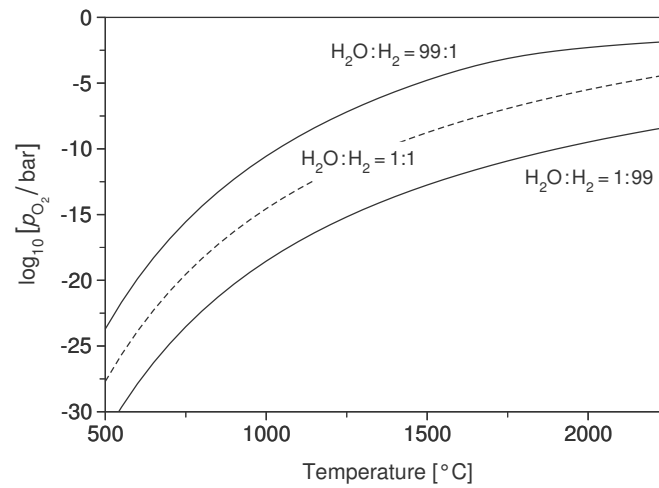


Figure 2.5: Oxygen fugacity of different H₂O/H₂ mixtures vs. temperature.

ner walls of the latter, contribute to an unavoidable p_{O_2} background. Gaseous redox pairs easily can hold oxygen fugacity way below this background level as evidenced by Figs. 2.4 and 2.5.

Application of appropriate gaseous redox pairs is also beneficial with respect to the stability of the atmosphere against fluctuations e.g. of gas flows and unexpected sources of oxygen. In case of an inert gas, e.g. argon, additional oxygen entering the system directly increases oxygen pressure. Therefore, if the atmosphere does not contain reactive components (what is usually meant by “inert” atmosphere) and oxygen fugacity is intended to be low, then vast flows of the process gas are required to sufficiently dilute unwanted oxygen. If, however, the growth atmosphere exploits reactive components based on redox pairs, the additional oxygen is buffered by the redox equilibrium. According to Le Chatelier’s principle an increase of oxygen shifts equilibrium until the equilibrium constant (Eq. 2.7) is attained again. The new equilibrium state is characterized by a smaller degree of dissociation of CO_2 partially compensating the additional oxygen. Fig. 2.6 shows the calculated oxygen fugacity at 1 bar and $2000^\circ C$ of three CO/CO_2 mixtures. In case of pure CO , oxygen injection steadily increases oxygen fugacity but at much lower level than injected. The largest part of that additional oxygen reacts with CO that is available at great excess to form CO_2 . In case of CO_2 or 1:1 mixture of CO and CO_2 addition of oxygen only marginally changes oxygen fugacity. Only for an unlikely high level of contamination above 1% high the impact becomes appreciable. Addition of 1% oxygen to an equimolar mixture of CO and CO_2 causes an only negligible increase of oxygen fugacity from 9.3×10^{-5} bar to 1.1×10^{-4} bar, because at $2000^\circ C$ carbon dioxide is dissociated to an extent that allows to “absorb” additional oxygen by shifting the equilibrium (Eq. 2.6).

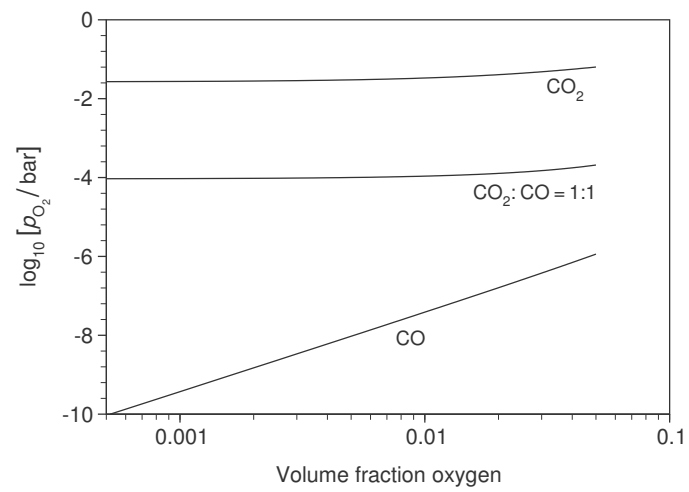


Figure 2.6: Impact of an oxygen contamination, e.g. due to leakage, on oxygen fugacity for different atmospheres (at 2000 °C).

3 Crystal growth from the melt

Today, the by far largest part of crystals used in technical or laboratory applications is grown from the melt. The indisputable front runner with respect to produced mass and market value is silicon, mainly for application in microelectronics. Compared with other methods, e.g. growth from vapor or solution, many melt growth techniques reached a stage of development that allows for fabrication of large crystals of excellent structural and chemical quality at acceptable costs. However, some obstacles may impede melt growth, e.g. destructive phase transitions between melting point and room temperature, vitreous solidification, or massive sublimation below the melting temperature. In those (and a few more) cases growth from the gas phase, solution, or even from solid state may be the better choice.

Naturally, crystal growth from the melt happens close to the melting temperature of the regarded material. Technical difficulties of generating and controlling of high temperatures delayed development of melt growth for many materials to the end of the 19th century. Around the turn of the century Auguste Verneuil developed a flame fusion process later named after him and presented first melt grown ruby crystals. During the following thirty years all basic melt growth techniques were invented including free growth from a (cooled) seed into the melt (Nacken [111] and Kyropoulos [90]), pulling from the melt (Czochralski method [45]), directional solidification in a crucible (Bridgman-Stockbarger technique [29, 30]), and zone melting [82].

3.1 The Bridgman-Stockbarger technique

With respect to practical implementation, solidification of melt contained in a cylindrically shaped crucible is one of the simplest arrangements for growing crystals from the liquid phase. The crucible is placed in the thermal field of the furnace in such way that – after initial melting and homogenization of the entire load – crystalliza-

tion occurs first at the bottom part and proceeds upwards until all melt is solidified. The velocity at which the melting isotherm moves through the crucible corresponds to the growth velocity. Displacement of the melting isotherm can be achieved by translating either the crucible or the thermal field as a whole. The technique involving a stationary crucible was introduced by Tammann and further developed by Stöber (Tammann-Stöber technique). Bridgman used a growth technique in which the crucible was slowly moved downwards in a vertical temperature gradient (Fig. 3.1) that was further developed to growth of large alkali halide crystals by Stockbarger (Bridgman-Stockbarger technique).

In most arrangements the crucible is cylindrically shaped with a conical bottom and a tube-like tip that allows mounting of a small seed crystal (Fig. 3.1). On top it can be closed by a cap, lid or seal to reduce the loss of volatile components of the melt. In terms of process control the main disadvantage of the technique is the missing simple feedback that could be used to determine the interface location and therewith the interface displacement or growth velocity. Close contact of the crystal with crucible walls generates mechanical stress during cooling, often seriously reducing structural quality. Recent development of the Bridgman technique, the so-called detached or dewetted growth, initiated by growth experiments under microgravity conditions, aimed at prevention of crystal adhesion to the crucible wall [53, 176]. Under terrestrial conditions detachment of the crystal can be obtained e.g. by controlling the pressure in the ampoule near the growing crystal [131, 12].

3.2 The Czochralski technique

The most widely used growth technique with respect to the amount of material and number of different substances grown is the pulling technique named after Jan Czochralski. This technique originally invented to measure the crystallization speed of metals [45] turned out an extremely versatile technique for the growth of bulk single crystals.

The material is melted in a crucible of usually cylindrical shape and heated radially either by resistance or induction heating (Fig. 3.2). Once the material in the crucible is molten and homogenized, a small seed crystal is immersed into the melt from the top. The temperature of the melt is adjusted by the operator so that a steady-state

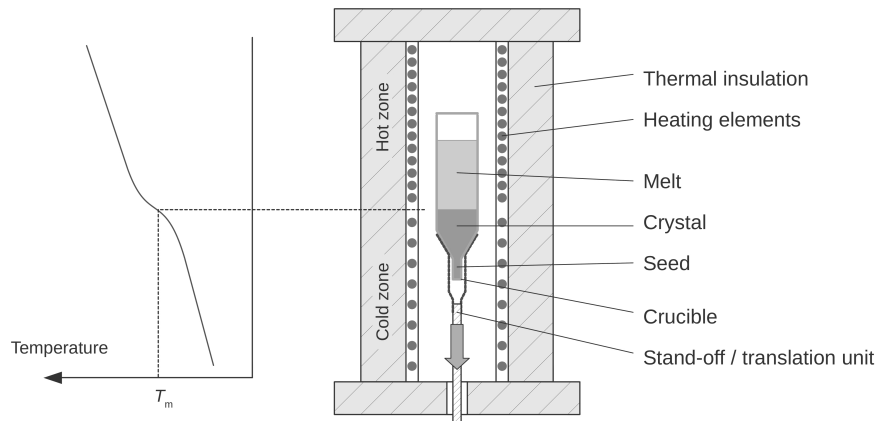


Figure 3.1: Sketch of the Bridgman growth technique and temperature distribution in the growth furnace.

is achieved in which the seed/crystal does not grow uncontrolled nor melt off. Upon subsequent slow pulling upwards, the portion of melt attached to the seed is lifted above the melt level where the actual temperature is below the freezing temperature and crystallization starts. The amount of material that crystallizes in a given time interval, i.e. the mass growth rate, depends on the degree of supercooling and can be controlled by adjustments of the heating power. Widely used automatic diameter control (ADC) techniques rely mainly on measurements of the crystal or crucible mass and controlling the mass growth rate in a closed loop system. The typical bottle-like shape of Czochralski grown boules stems from the common procedure of growing a small diameter crystal right from the seed allowing defects to grow out and following increase of the diameter to the desired value. During growth, the crystal is rotated (i) to compensate azimuthal inhomogeneities of the thermal field, and (ii) to affect mixing of the melt by triggering fluid convection as briefly discussed in the Sect. 3.4.3. After the crystal has reached its designated length, it is withdrawn from the melt. Still inside the thermal enclosure above the crucible usually formed by various types of afterheaters and insulations it is slowly cooled down to room temperature and harvested.

The absence of direct contact of the growing and cooling-down crystal with the crucible generally leads to an excellent structural perfection, i.e. low dislocation density and low thermal stress as often demanded by applications in electronic or

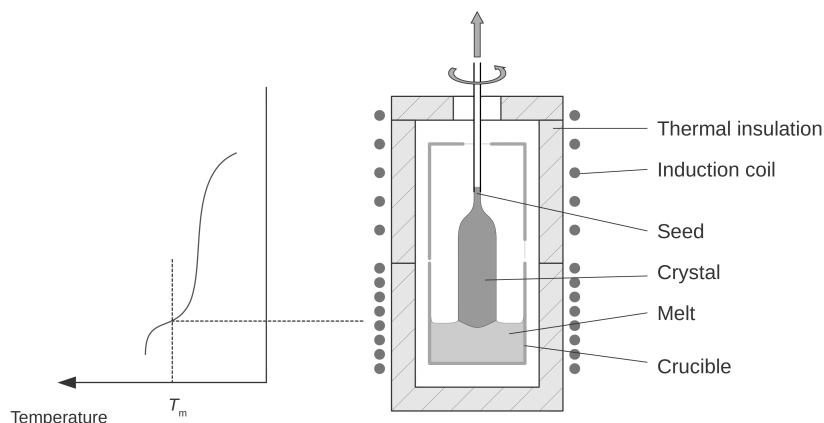


Figure 3.2: Sketch of the Czochralski growth technique with induction heating and desirable temperature distribution.

optical devices. Also, easy visual feedback by nearly vertical or radial surveillance is beneficial since it allows early recognition of macroscopic defects and eventually immediate corrective measures up to new startup without cooling the whole system.

3.3 The micro-pulling-down technique

The micro-pulling-down technique is a rather new growth technique that became progressively popular after a series of reports concerning the growth of lithium and potassium lithium niobate crystals [187, 188, 189] and $\text{Si}_{1-x}\text{Ge}_x$ solid solutions [145, 169]. This technique is a miniaturized variant of the Edge-defined Film-Fed Growth (EFG) or Stepanov method, depending on the melt's wetting behavior, with pulling in the downward direction. It harkens back to the work of Mimura et al. [105] who successfully pulled thallium bromiodide ($\text{Tl}(\text{Br},\text{I})$, KRS-5) meter-long crystal fibers with diameter below 1 mm for infrared optical waveguides.

The material to be grown is melted in a crucible with a capillary orifice in the bottom (Fig. 3.3). The diameter of the capillary is small, usually below 1 mm, that the melt does not leak through even under the hydrostatic pressure of the overlying melt column. In the common case of a melt wetting the crucible a small drop appears below at the lower end of the capillary as soon as the material is

molten. A seed crystal is touched from the bottom and a tiny molten zone develops between capillary and seed. Driving the seed downwards starts the crystallization process. Typical pulling rates range from 0.1 mm/min for multicomponent crystals to > 10 mm/min for simpler substances, e.g. element crystals or simple oxides. Seeding and growth are observed through a small opening in the thermal insulation surrounding the crucible, and the operator exercises control over the process by manual adjustments of heating power and/or pulling rate.

The micro pulling down process is characterized by capillary stability, i.e., the immunity of the process against fluctuations of the growth angle. Capillary stability assures constant diameter growth without corrective adjustments e.g. of heating power or pulling rate. Meniscus shape and capillary stability during EFG was analyzed by Tatarchenko et al. [163, 165, 164, 9] and Surek et al. [158, 159, 160]. From these works it can be concluded that in case of wetting melt capillary stability occurs if the fiber diameter is at least roughly half the outer capillary diameter,

The combination of steep temperature gradients, typically a few 100...1000 K/cm or even more [170, 99], that result in an extraordinary morphological stability of the interface (cf. Sect. 3.4.4), and adjustable length of the capillary in which solute transport is diffusion-limited predestine the micro-pulling-down technique for the growth of solid solutions where segregation related phenomena may have a great impact on crystal quality.

3.4 Selected issues of melt growth of oxides

3.4.1 Transport of heat through the growing crystal

The most important phenomenological process during melt growth is transport of heat by conduction, convection (in particular in fluid phases), and radiation (for at least partially transparent media and high melting temperatures). At the crystallization front (“interface”) the heat balance must be satisfied, i.e. the heat flux away from the interface through the crystal \dot{Q}_S must compensate the heat flux from the liquid \dot{Q}_L and the latent heat released during crystallization with velocity v

$$\dot{Q}_S = \dot{Q}_L + v\rho\Delta h \quad (3.1)$$

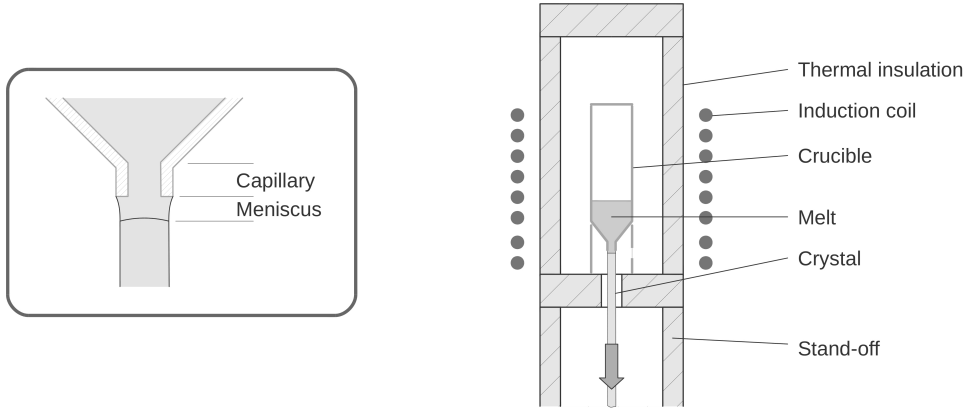


Figure 3.3: Sketch of the micro pulling down technique. The left-hand inset shows a close up of the lower end of the crucible capillary, i.e. the growth region.

wherein ρ is the density of the solid and Δh the enthalpy of fusion. The most interesting technological parameter with great impact on crystal quality and economic efficiency of the whole process is growth velocity. From the above equation follows that

$$v = \frac{\dot{Q}_S - \dot{Q}_L}{\rho \Delta h}. \quad (3.2)$$

Growth velocity is maximized (i) by increasing heat flux through the growing crystal, or (ii) by reducing heat flux in the liquid phase towards the interface. Natural and forced convection in the melt can reduce the latter drastically, so that the maximum growth rate is roughly dependent on heat transport through the crystal only,

$$v_{\max} \approx \frac{\dot{Q}_S}{\rho \Delta h}. \quad (3.3)$$

Heat transfer through the solid body occurs by conduction and radiation. The conductive heat flow depends linearly on the thermal gradient

$$\dot{Q}_{S,\text{cond}} = -\lambda \frac{\partial T}{\partial z} \quad (3.4)$$

with λ being the thermal conductivity, and z the coordinate along the crystal

T in °C	1000	1500	2000
$\dot{Q}_{S,\text{cond}}$	3.67	2.25	0.83
$\dot{Q}_{S,\text{rad}}$	1.25	3.48	7.48

Table 3.1: Estimated conductive (Eq. 3.4) and radiative (Eq. 3.5) heat fluxes (in W/cm^2) through Al_2O_3 at different temperatures for a thermal gradient of 20 K/cm and an ambient temperature 100 K below the temperature of the radiating interface. Thermal conductivity was linearly interpolated between 32.5 $\text{W}/(\text{m}\cdot\text{K})$ at room temperature and 3.4 $\text{W}/(\text{m}\cdot\text{K})$ at melting temperature [52]. The interface emissivity was taken 0.3.

axis. The radiative flux equals

$$\dot{Q}_{S,\text{rad}} = \varepsilon\sigma(T^4 - T_a^4), \quad (3.5)$$

where σ denotes the Stefan-Boltzmann constant, ε the emissivity of the radiating surface, T and T_a the temperature of the interface and of the ambient, respectively. Radiative heat flux grows strongly with temperature whereas the conductive flux decreases due to the temperature dependence of the heat conductivity at temperatures well above the Debye temperature, $\lambda \propto 1/T$. Tab. 3.1 compares estimated conductive and radiative heat fluxes for Al_2O_3 for different temperatures in thermal conditions typical for oxide growth. As a rule of thumb, below 1500 °C heat conduction, above that temperature radiation is the prevailing mechanism of heat transport. Notably, optical absorption, especially in the near infrared spectral region characteristic for several rare-earth ions, may reduce radiative heat flux significantly. Infrared absorption is regarded one of the necessary conditions for footing or spiraling frequently observed during Czochralski growth of high melting point oxides [22, 172, 151].

Eq. 3.3 allows to estimate the upper limit of the maximum growth rate. For LiNbO_3 — a typical low melting point oxide ($T_f = 1253^\circ\text{C}$, $\Delta h = 456 \text{ J/g}$, $\rho = 4.66 \text{ g}/\text{cm}^3$, $\lambda = 3.9 \text{ W}/(\text{m}\cdot\text{K})$; data from [85]) — one calculates $v_{\text{max}} \approx 13 \text{ mm/h}$ for a temperature gradient of 20 K/cm if only conductive transport is considered (Eq. 3.4). For highly transparent, high melting point oxides, e.g. Al_2O_3 ($T_f = 2053^\circ\text{C}$, $\Delta h = 1110 \text{ J/g}$, $\rho = 3.97 \text{ g}/\text{cm}^3$, $\varepsilon = 0.3$; data from [52]) assuming an

	T_m	α	ν	Pr	Sc	Refs.
	[°C]	[cm ² /s]	[cm ² /s]			
Gd ₃ Ga ₅ O ₁₂	1750	0.015	0.07	4.7	3500	[50, 142]
Y ₃ Al ₅ O ₁₂	1970	0.014	0.13	9.3	6500	[60]
Al ₂ O ₃	2050	0.01	0.188	19	9400	[137, 91, 52]
LiNbO ₃	1253	0.0084	0.11	13	5500	[7, 168]

Table 3.2: Melting temperature (T_m), and approximate values of thermal diffusivity (α), kinematic viscosity (ν), Prandtl (Pr) and Schmidt (Sc) numbers of some oxide melts. The diffusion coefficient was assumed to be $D = 2 \times 10^{-5}$ cm²/s.

ambient temperature of 100 K below the interface temperature, a maximum growth rate $v_{\max} \approx 65$ mm/h is obtained. In practice, however, the maximum growth rate is rather limited by solute-related effects like segregation and morphological stability of the interface (see Sect. 3.4.4).

3.4.2 Transport of heat and matter in the fluid phase

Inside the melt, transport of heat may occur by conduction or convection. The Prandtl number Pr defined as the ratio of momentum diffusivity (i.e. the kinematic viscosity ν) to thermal diffusivity α ,

$$Pr = \frac{\nu}{\alpha}, \quad (3.6)$$

gives an estimate of the relative magnitude of viscous to thermal diffusion rates. Thermal diffusivity is the ratio of thermal conductivity and heat capacity per unit volume, $\alpha = \lambda/(\rho c_p)$, with the density ρ and specific heat capacity c_p . Table 3.2 compiles properties of various oxide melts including melts with high (Al₂O₃) and with rather low melting temperatures (LiNbO₃). For all these melts, since $Pr > 1$, heat transport happens mostly due to convection.

The analogon of the Prandtl number for transport of matter is the Schmidt num-

ber that is defined as

$$Sc = \frac{\nu}{D}, \quad (3.7)$$

with the diffusion coefficient D of the respective species. The values listed in Tab. 3.2 are for a diffusion coefficient $D = 2 \times 10^{-5} \text{ cm}^2/\text{s}$. For Al_2O_3 melt, Rosenberger and Müller [137] published a value of $2.2 \times 10^{-4} \text{ cm}^2/\text{s}$ giving Schmidt numbers more than one order of magnitude smaller than in Table 3.2 but still of the order of a few hundreds. Since $Sc \gg 1$ it is well-founded that also species transport occurs practically exclusively by convection and that melt mixing by diffusion can be neglected.

3.4.3 Melt convection and interface flip in Czochralski pulling

Three types of convection are observed in oxide melts, namely (i) natural or buoyancy convection, (ii) forced convection, and (iii) thermocapillary or Marangoni convection. The latter is driven by the temperature dependence of the surface tension γ and temperature gradients along the melt surface. Marangoni convection occurs within a thin layer at the free melt surface only and is responsible for so-called spoke patterns frequently observed on melt surfaces but does not contribute significantly to the transport in the bulk melt. Buoyancy convection is caused by density differences owing to thermal expansion of the melt. Hot melt rises at the crucible walls and descends in its center (Fig. 3.4a). The strength of buoyancy convection is characterized by the Grashof number which approximates the ratio of the buoyancy to viscous force acting on a fluid

$$Gr = \frac{g\beta\Delta TR^3}{\nu^2} \quad (3.8)$$

with g denoting gravitational acceleration, β the thermal expansion coefficient, R and ΔT the crucible radius and the radial temperature difference, respectively.

The term forced convection refers to all types of fluid flows that are triggered by an external action like crystal or crucible rotation, vibrations, external magnetic fields and others. For growing oxides, only forced convection driven by crystal rotation gained practical importance. Driving force for rotationally forced convection can be

expressed by the rotational Reynolds number

$$Re = \frac{\omega d^2}{\nu} \quad (3.9)$$

where d is the crystal diameter and ω the crystal rotation rate. Fluid beneath the rotating crystal is accelerated centrifugally and a convection roll is generated aspirating melt vertically in the center and spinning outwards near the melt surface. Both, natural and forced convection occur concurrently and it is commonly accepted that the change from predominantly buoyancy to forced convection is the reason for one of the most spectacular phenomena during Czochralski growth of oxides called the interface flip. At low Reynolds numbers fluid flow is dominated by buoyancy convection (Fig. 3.4a). In this flow regime the solid-liquid interface tends to be strongly bended and convex towards the melt, especially for transparent high-melting point oxides. With increasing rotation rate and/or crystal diameter, i.e. with increasing Reynolds number, stimulus for forced convection increases and a rotationally vortex develops beneath the crystal with flow direction opposite to that of the buoyancy vortex. Above a critical Reynolds number Re_c (or a critical range) global fluid flow collapses and forced convection becomes dominant (Fig. 3.4b). Hot melt is transported to the growth interface and fluid temperature at the interface increases greatly. This leads to back-melting of the interface that becomes less convex, nearly flat, or even concave. The interface flip has been studied extensively for the growth of several rare-earth gallium and aluminum garnets, e.g. $Gd_3Ga_5O_{12}$ (GGG), $Y_3Al_5O_{12}$ (YAG), or bismuth silicate $Bi_{12}SiO_{20}$ (BSO), where facets on the convex interface lead to strained crystals of minor optical quality (e.g. [43, 28, 179, 37, 161, 104, 126, 15, 185, 62, 190]). A crude criterion for the onset of the transition was proposed by Carruthers [37] by equating the Grashof number with the square of the Reynolds number

$$Gr = Re^2. \quad (3.10)$$

From the definitions of Gr and Re follows that the critical crystal diameter d_c for which the transition from predominantly buoyancy to predominantly forced convec-

tion and, consequently, the interface flip is expected to occur

$$d_c = \frac{g\beta\Delta TR^3}{(\pi\omega)^{1/2}} \quad (3.11)$$

is inversely proportional to the square root of the crystal rotation rate and increases with the third power of the crucible dimension. This result has been confirmed experimentally by several groups [108, 161, 104]. Other groups instead found significant deviations, especially for larger crucible diameter [104, 107, 86]. Xiao & Derby made a systematic numerical analysis of heat transfer and interface inversion [184, 185]. They found that radiant heat transport through the transparent crystal greatly promotes deep (convex) interfaces, decreasing temperature gradient in the crystal, and greater gradients in the melt. They investigated the influence of thermal geometry (low or high thermal gradient systems) and transparency of the growing crystal on the critical rotation (critical Reynolds number) at which interface inversion occurs and ascertained a rough agreement with Eq. 3.10.

Growth of large crystal boules entails significant changes in thermal gradients with process duration. As larger fractions of the melt are solidified, the area of the exposed inner crucible wall acting like an active afterheater increases. At the same time the ambient temperature “seen” by the crystal increases and thermal gradients decrease. This is evidenced by growing facets on both, the interface and the mantle surface of the growing crystal [64]. With decreasing (radial) temperature gradient strength of buoyancy convection (the Grashof number) decreases and forced convection easily becomes dominant. As a consequence, interface flip can occur even for constant, initially undercritical rotation when the crystal surpasses a certain length.

3.4.4 Solute segregation and morphological stability

Solute inhomogeneities arising from segregation upon solidification are imperfections inherent to multicomponent crystals grown from the melt. If liquid and solid have different chemical compositions, the liquid is continuously enriched in the excess component leading, in turn, to a continuously increasing concentration of that component also in the crystal. This macrosegregation is usually undesired but can

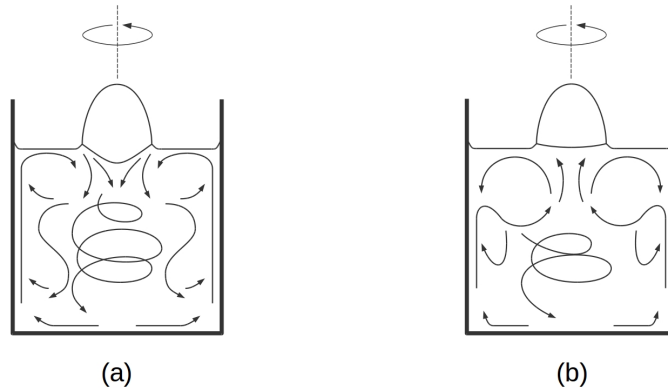


Figure 3.4: Bulk flow modes observed in experiments simulating oxide melts (after [21]). Crystal rotation rate is low in the left, high in the right figure.

be utilized in applications requiring a gradient in the material's properties, e.g. a lattice constant gradient for X-ray and γ -ray diffraction optics [2]. Short-term variations of growth velocity caused by thermal or solute fluctuations in the fluid phase trigger formation of striations, i.e. short period variations of crystal composition or dopant concentration. Here, growth velocity dependence of the interface and effective distribution coefficients are of crucial importance. Although generally seriously degrading crystal quality, also well-defined striations may be beneficial in some applications, e.g. for domain reversal in periodically poled lithium niobate [106, 98, 16]. Associated with segregation is the formation of a solute boundary layer and solute gradients at the interface. Imminent danger of ultimate break-down of crystal quality arises from the phenomenon of constitutional supercooling briefly discussed in the last part of this subsection.

Equilibrium and interface distribution coefficient In multicomponent systems, two phases in thermodynamic equilibrium in general will have different chemical compositions. For melt growth processes, the equilibrium distribution coefficient k_0 of a solute, e.g. a dopant or main constituent, is defined as the ratio of solute

concentration in solid phase, C_S , and in liquid phase, C_L ,

$$k_0 = \left. \frac{C_S}{C_L} \right|_{\text{equilibrium}} . \quad (3.12)$$

If the composition–temperature phase diagram of the regarded system is known then k_0 can be simply read from the diagram. A quantitative expression can also be derived from the equilibrium condition, i.e. the equality of the chemical potential of the solute in both phases. In case of ideal solution in liquid and solid phases an approximate expression for the distribution coefficient is given by ([180] p. 117)

$$\ln k_0 \approx \frac{\Delta h_m}{T_m} \frac{(T_m - T)}{RT} \quad (3.13)$$

where Δh_m and T_m denote the melting enthalpy and melting temperature of the pure solute, respectively.

The equilibrium distribution coefficient applies to equilibrium state only. In equilibrium the thermodynamic driving force for growth, i.e. supercooling ΔT or supersaturation ΔC , vanishes and no (net) growth occurs. The equilibrium distribution coefficient defined by Eq. 3.12 is therefore unsuitable to describe incorporation of solute into the *growing* crystal. It is convenient to define a *kinetic* or *interface* distribution coefficient being the ratio of solid and liquid solute concentrations at the interface

$$k^* = \frac{C_S}{C_L^*} \quad (3.14)$$

that is not subject to that restriction. The interface distribution coefficient depends upon parameters like growth velocity, (crystallographic) growth direction, or supersaturation. According to the accepted notion, atomically flat interfaces grow due to incorporation of an adsorbed layer on the interface by rapid lateral growth after nucleation requiring larger supercooling. Rapid growth hampers rearrangement of solute atoms, and as a result, for large supercooling k^* may significantly differ from k_0 whereby $k_0 \leq k^* \leq 1$ for the case of rejected solute. Atomically rough interfaces in contrast usually follow the melting temperature isotherm. Supercooling on such faces is often negligibly small and the interface distribution coefficient approximates the equilibrium value. Therefore

$$\begin{aligned} k^* &\rightarrow k_0 && \text{for } \Delta T \rightarrow 0 \\ k^* &\rightarrow 1 && \text{for } \Delta T \rightarrow \infty. \end{aligned} \tag{3.15}$$

Effective distribution coefficient Upon crystallization, if solute is rejected from the interface ($k^* < 1$, the opposite case $k^* > 1$ can be treated in an analogue way) the melt is continuously enriched in that solute. If the melt is well mixed, e.g. by convection, then the rejected solute is homogeneously distributed in the bulk of the melt thus increasing C_L . However, a thin fluid layer adjacent to the interface termed diffusion boundary layer is not affected by bulk convection (non-slip condition) and solute transport within this layer is assumed solely diffusive. If growth proceeds fast and solute is rejected from the interface at a higher rate than it can diffuse into the bulk of the melt then solute concentration at the interface C_L^* rises above C_L and a solute concentration gradient is built up ahead of the interface (Fig. 3.5). The effective distribution coefficient k is defined as the ratio of concentration of solute in the solid to that in the bulk liquid

$$k = \frac{C_S}{C_L}. \tag{3.16}$$

Since $C_L^* > C_L$ the effective distribution coefficient is always larger than the interface distribution coefficient, $k > k^*$. During steady state growth, rejection of solute from the interface is compensated by the flux of solute down the concentration gradient in the liquid at the interface

$$C_L^*(1 - k^*)f = -D \left. \frac{\partial C_L}{\partial z} \right|_{z=0} \tag{3.17}$$

wherein f denotes the growth velocity, i.e. the displacement rate of the interface, and z the distance from the interface into the liquid. Burton, Prim & Slichter (BPS) solved the diffusion equations and found that the effective distribution coefficient [35]

$$k = \frac{k^*}{k^* + (1 - k^*) \cdot \exp(-f\delta/D)}. \tag{3.18}$$

where δ is defined as the distance from the interface at which solute concentration drops from its interface value C_L^* to its bulk value C_L (Fig. 3.5). For small growth velocity $f \rightarrow 0$ the effective distribution coefficient approaches the value of the interface distribution coefficient, for very large velocities instead unity.

Usually δ is interpreted to be the thickness of the fictive solute diffusion boundary layer in which the fluid is assumed to be motionless (stagnant film model). This flimsy assumption has provoked a number of critical reviews, e.g. [181, 182, 183, 56, 128]. Wilson [182] proposed a definition of δ based upon the solute concentration profile in the liquid at the interface

$$\bar{\delta} = \frac{C_L - C_{L\infty}}{(\partial C_L / \partial z)_{z=0}} \quad (3.19)$$

and found good agreement with BPS's results for very low growth velocities. For Czochralski growth from large Schmidt number melts BPS derived the approximation

$$\delta = 1.6 D^{1/3} \nu^{1/6} \omega^{-1/2} \quad (3.20)$$

with ω denoting the angular velocity of crystal rotation. Assuming a crystal rotation rate of 10 rpm yields an angular velocity of $\omega = 2\pi \cdot 10/60 \text{ s} \approx 1/\text{s}$. Typical data for oxides growth (Table 3.2) yield a value of $\delta \approx 0.33 \text{ mm}$. However, from Eq. 3.20 it is clear that crystal rotation constituting the impetus for forced convection has a great impact on the boundary layer thickness and, consequently, the effective distribution coefficient.

Ostrogorsky and Müller [128] proposed an improved model taking into account convective solute transfer in the fluid phase and replacing δ with realistic physical parameters. If the tangential velocity of the fluid flow at the edge of the solute boundary layer is much larger than growth rate, like it is the case e.g. for Czochralski processes, the effective distribution coefficient can be expressed by

$$k = \frac{1 + \xi}{1 + \xi/k^*} \quad (3.21)$$

where

$$\xi = 4a \frac{(\omega D)^{1/2}}{f} \left(\frac{D}{\nu} \right)^{2n - \frac{1}{2}}. \quad (3.22)$$

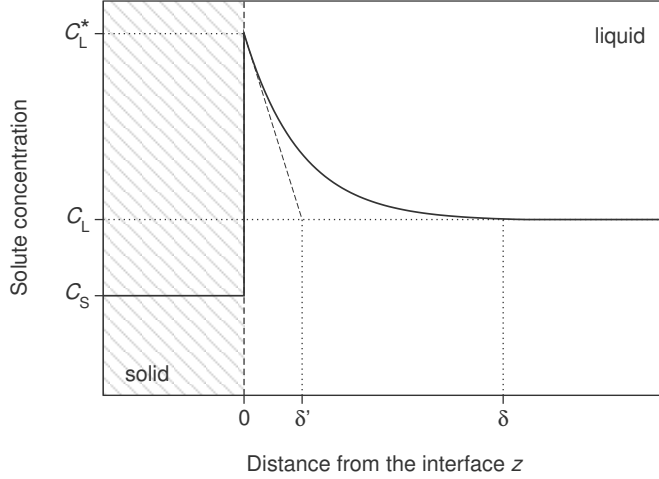


Figure 3.5: Solute distribution in the liquid phase near the growth interface for $k^* < 1$.

The parameter depends on the assumed shape of solute concentration in the liquid. For a linear approximation $a = 1/6$. The parameter n is weakly dependent on the Schmidt number Sc . For fluids having $1 \leq Sc \leq \infty$ the exponent is $1/2 \leq n \leq 1/3$. Within this model, the thickness of the solute boundary layer is given by

$$\delta = 4 (\nu/\omega)^{1/2} (D/\nu)^n. \quad (3.23)$$

Fig. 3.6 shows the growth velocity dependence of k according to the two models for $k^* = 0.1$ and $k^* = 2$. The solid curves correspond to the BPS model, the dashed and dotted curves follow the model of Ostrogorsky & Müller for $n = 1/2$ and $n = 1/3$ (case for very large Schmidt numbers), respectively. The curves exhibit the same behavior for the cases of very low or very high growth velocities approximating k^* for $f \rightarrow 0$ and 1 for $f \rightarrow \infty$. For intermediate velocities, the model of Ostrogorsky & Müller involves a rise extending over a much wider range of growth velocities. Interestingly, for $n = 1/2$ this model predicts a significant variation of k for growth velocities typical for Czochralski growth of oxides. In the BPS model k starts rising at much higher growth velocities, exceeding those typically applied to oxides, but rises very quickly then to approach values near unity at lower velocities than predicted by the model

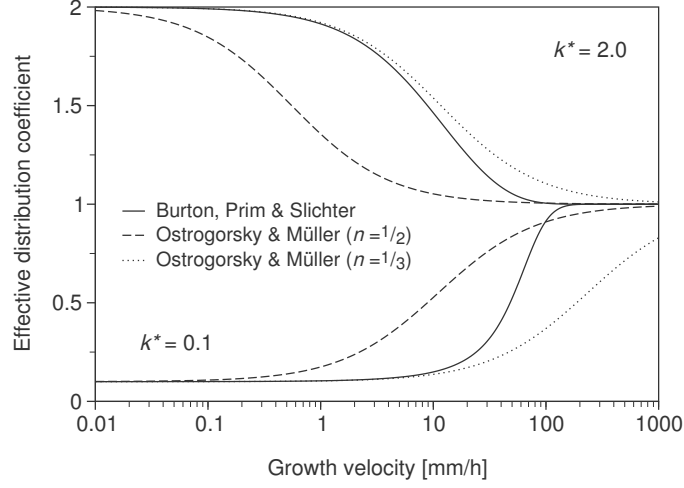


Figure 3.6: Dependence of the effective distribution coefficient on growth velocity for $k^* = 0.1$, respectively $k^* = 2.0$, according to the BPS model (solid lines) and Ostrogorsky & Müller model with $n = 1/2$ (dashed lines) and with $n = 1/3$ (dotted blue lines).

of Ostrogorsky & Müller.

Distribution of solute in the growing crystal Proceeding rejection of solute from the interface leads to an increasing solute concentration in the bulk of the melt. Conservation of solute requires that the amount of solute released when the crystal grows by an infinitesimal volume dV_S must increase solute concentration in the remaining melt volume V_L by an amount dC_L so that

$$(C_L - C_S)dV_S = V_L dC_L. \quad (3.24)$$

This equation can be transformed and easily integrated for $k = \text{const}$ yielding an expression for the solute distribution profile in the grown crystal

$$C_S(g) = k C_{L0}(1 - g)^{k-1} \quad (3.25)$$

with C_{L0} being the solute concentration in the initial melt and g the solidified

fraction of the melt which can be translated e.g. to an axial position. In crystal growth literature Eq. 3.25 often is called Scheil or Scheil-Gulliver equation (mainly in the Anglo-American community). However, it was first derived by Hayes and Chipman [72] three years before the often cited work in which Scheil covers solute distribution in solid solutions with *variable*, composition-dependent distribution coefficient [148].

According to the assumption, Eq. 3.25 is valid for steady state growth with constant effective distribution coefficient. This is strictly true only for a perfectly mixed melt when the thickness of the boundary layer $\delta = 0$ and $k = k^*$ over the entire crystallization process. In reality, after growth was initiated a boundary layer will develop and k will increase from k^* to some final value $k^* \leq k \leq 1$ depending on growth velocity. In the limiting case of a completely unstirred melt (in practice it is sufficient that fluid convection does not interfere the solute concentration profile ahead the interface) the effective distribution coefficient will rise to $k = 1$ resulting in a crystal with homogeneous solute concentration equal that in the melt. Steady state will emerge after a transient after a time [27, p. 155]

$$\tau \simeq \delta^2/D, \quad (3.26)$$

that is of the order of a few ten seconds for most melt growth processes. Fig. 3.7 shows the solute concentration profile in the crystal for a process with $k^* = 0.1$ for (i) the case of perfect mixing of the melt ($k = k^*$, dotted curve), (ii) the case of unstirred melt (purely diffusive solute transport, $k = 1$, solid curve), and (iii) the most practical case of partial mixing ($k^* < k < 1$, dashed curve). The left part of the graph shows the initial transient in time scale.

Constitutional supercooling The distribution of solute in the boundary layer can affect the stability of the growth interface. In case of $k^* < 1$ (again, the case of $k^* > 1$ can be treated in an analogue way) the increased solute concentration at the interface and in the boundary layer entails a lowering of the equilibrium solidification temperature T_e according to the drop of the liquidus line in the phase diagram as shown in Fig. 3.8. During growth, the actual temperature of the interface must match T_e reduced by the necessary supercooling. If the temperature gradient in

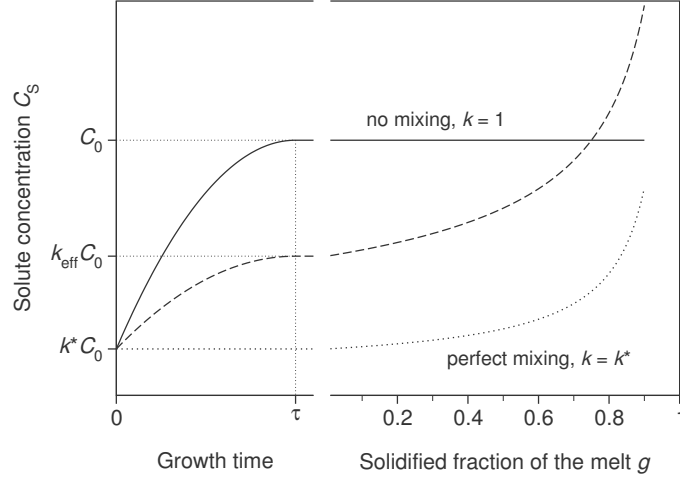


Figure 3.7: Solute concentration in the solid for the cases of perfect mixing (dotted line), partial mixing (dashed line), and no mixing (solid line) of the melt for $k^* = 0.1$. The transient time τ is of the order of seconds corresponding to $g \sim 10^{-4}$.

the liquid is small (curve 'b' in the figure) then the effective supercooling $\Delta T(z) = T(z) - T_e(z)$ increases into the melt. Small projections reaching this constitutionally supercooled region will grow rapidly giving rise to cellular growth spelling fatal degradation of crystal quality. If, however, the actual temperature follows curve 'a' (steep gradient regime) then supercooling decreases with z and the interface remains stable.

Obviously, the constitutional supercooling can be avoided if the temperature gradient in the melt at the interface is larger than the gradient of the equilibrium solidification temperature which is related to the solute concentration gradient via the slope of the liquidus curve m

$$G_0^T = \left(\frac{\partial T}{\partial z} \right)_{z=0} \geq m \left(\frac{\partial C_L}{\partial z} \right)_{z=0}. \quad (3.27)$$

Employing the previously derived expression for the compositional profile in the

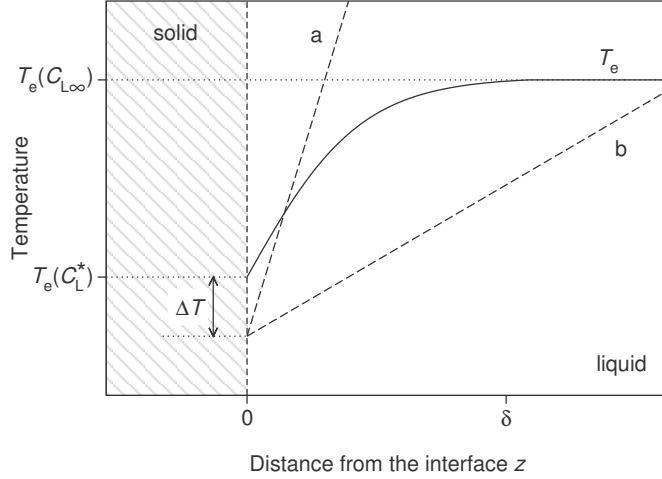


Figure 3.8: Equilibrium solidification temperature T_e (solid line) and actual temperature (dashed lines) near the growth interface. In case of low thermal gradient in the melt (curve 'b') supercooling ΔT may increase into the melt leading to a constitutionally supercooled region.

boundary layer, inequality (3.27) can be brought into the handy form [36, p. 334]:

$$\frac{G_0^T}{f} \geq -\frac{1-k^*}{k^*} \frac{mC_L}{D} k, \quad (3.28)$$

known as the Tiller criterion¹. Readily, low temperature gradient and fast pulling, a steep liquidus and high solute concentration in the liquid promote constitutional supercooling. Melt mixing instead increases morphological stability of the interface, since $k \leq 1$.

3.5 Comparison of growth techniques

With respect to solute segregation and related phenomena, among the selected growth techniques the Czochralski and Bridgman techniques are comparable. The crucial influence of fluid convection in oxide melts prevents formation of an ex-

¹Setting $k = 1$ yields the original form of the criterion as derived by Tiller et al. [166] for purely diffusive solute transport (no-mixing case).

tended solute boundary layer at the interface. The melt can therefore be considered as perfectly mixed and solute profile in the grown crystals described by the Scheil distribution (Eq. 3.25) with an effective distribution coefficient not significantly differing from the interface distribution coefficient for commonly applied pulling velocities. Thermal gradients in the liquid phase near the interface are of the order of 10...100 K/cm [43, 134, 49, 24]. Using the Tiller criterion, the maximum stable growth rate for the exemplary case of ruby growth, $(1 - x) \text{Al}_2\text{O}_3 - x \text{Cr}_2\text{O}_3$ with $x = 0.006$ (cf. Sect. 5.1), $m = 330 \text{ K/1}$, $k^* = 2$, and $G_0^T \approx 50 \text{ K/cm}$, can be estimated to be roughly 3 mm/h.

Solute segregation during the micro pulling down growth differs essentially from the two bulk growth techniques. The capillary separates melt in the tiny zone between interface and capillary bottom from that in the bulk of the crucible. Both regions taken by themselves are well mixed, the latter mainly by buoyancy convection, the former by Marangoni convection owing to steep temperature gradient along the free melt surface (Fig. 3.9). In case of a very small meniscus height, the Marangoni roll is too small to entrain all the whole molten zone leading to a radially different solute transport behavior frequently observed in micro pulling down growth [63]. The convection-free capillary constitutes a kind of artificial diffusion layer. Since usually its length is much greater than the thickness of any solute boundary layer developing at the growing interface, axial segregation is completely controlled by the length of the capillary L . For typical growth parameters and with δ replaced by L , the exponential term in the BPS formula (Eq. 3.18) becomes

$$\frac{f\delta}{D} = \frac{fL}{D} \approx \frac{0.5 \text{ mm/min} \cdot 2 \text{ mm}}{10^{-5} \text{ cm}^2/\text{s}} \approx 16.7. \quad (3.29)$$

The effective distribution coefficient becomes greater than 0.99 even for interface distribution coefficients k^* as low as 10^{-4} .

Additionally, the very steep temperature gradients associated with the micro-pulling-down technique ensure an exceptional morphological stability of the interface. Using the same phase diagram data as above but steeper temperature gradient of 500 K/cm, the maximum stable velocity according to Tiller becomes $\approx 45 \text{ mm/h}$ (0.75 mm/h).

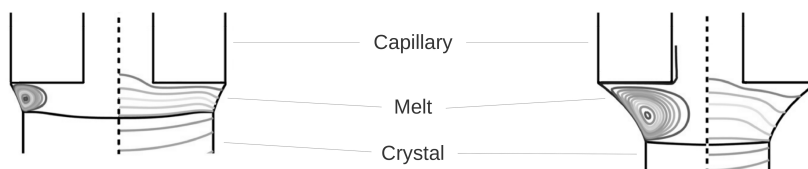


Figure 3.9: Enlarged view of the melt zone near the interface in the micro pulling down technique. Shaded lines are streamlines, respectively isotherms (interval ≈ 16 K) for two different growth velocities, 1 mm/min (left) and 5.0 mm/min (right) taken from the simulation of Samanta et al. [144] for the growth of sapphire.

	Bridgman & Czochralski	Micro pulling down
G_0^T	10...100 K/cm	100...1000 K/cm
f_{\max}	3 mm/h	0.75 mm/min
k	$\approx k^*$	≈ 1

Table 3.3: Temperature gradient in the liquid at the interface (G_0^T), effective distribution coefficient (k), and maximum stable growth according to the Tiller criterion (f_{\max}) for the growth of ruby ($\text{Cr}:\text{Al}_2\text{O}_3$) crystals.

4 Growth and characterization of wüstite crystals

Wüstite is the mineral name for iron(II) oxide, FeO , one end-member of magnesiowüstite (Mg,Fe)O solid solution, one of the main constituents of the lowermost mantle of our planet. The core–mantle boundary, the so-called D'' layer, is regarded as the chemically most active region of the Earth. Here, liquid iron from the core reacts with crystalline $(\text{Mg,Fe})\text{SiO}_3$ and magnesiowüstite to form MgSiO_3 and Stishovite (high temperature modification of SiO_2), and FeSi and FeO metallic alloys. This way iron permeates upward in the mantle and oxygen enters the core. This model explains the density of the outer core which is about 10% lower than that of pure iron under the given (p, T) -conditions [136, 78]. The heterogeneous D'' layer has a variable thickness of only 200...300 kilometers but affects global phenomena like wobbling of Earth's rotation axis, the geomagnetic field, and drift of large tectonic plates [78, 79]. Since the Earth's interior defies from direct observation, laboratory experiments on specimen in anvil cells with conditions similar to those in depths of a few thousand kilometers are of great value for geophysical sciences. Data gathered from experiments on artificial specimen greatly help to validate and improve models of the Earth's interior.

Formation and decomposition of wüstite also play an important role in hot-rolling steel shaping processes. Hot-rolled steel products are usually covered with an oxide scale that has to be removed before welding or brazing. Thickness and structure of the layers the scale is formed of depends on the cooling conditions at the exit of the rolling line. Being the first oxide layer that is formed on the surface of hot steel exposed to air, formation and decomposition of wüstite is of crucial importance for understanding the formation of the oxide scale [14, 67].

Single crystals of wüstite have been grown by various techniques. Burmeister [34]

used a Czochralski technique to pull crystals from a cold crucible. Due to the high intrinsic conductivity the material was melted without external heat sources. The crystal was pulled with nearly 1 cm/h into a cavity of temperature well above the eutectoid decomposition. After the growth the crystal was cooled down to room temperature within minutes. Following such procedure Burmeister obtained wüstite single crystals a few millimeters in diameter and up to 5 cm long. The author argues that at relatively short growth duration the amount of oxygen purging the cavity could lead only to a very marginal shift of composition of the grown crystals. In etching experiments he observed, however, beginning magnetite formation at grain boundaries. A tri-arc furnace was used by Hayakawa et al. [71] to melt wüstite in Ar ambient and pull crystals used for lattice parameter measurements at high temperatures. Wet chemical analysis indicated the composition of the grown crystals was $\text{Fe}_{0.905\dots0.908}\text{O}$. Bowen & Kingery [20] grew crystalline wüstite films by chemical vapor deposition on MgO substrates. The transport agent was HCl at low pressure (50 Torr), the deposition temperature between 640 and 900 °C, and growth rates reached 20 $\mu\text{m}/\text{h}$. Differences in thermal expansion between crystal and substrate were held responsible for the relatively high dislocation density of those films reaching $10^6/\text{cm}^2$. A Verneuil process was used by Chen & Peterson [40] to grow crystals for use in diffusion experiments. To avoid possible contamination originated from a container, Berthon et al. developed an optical float zone growth of wüstite [17] to grow crystals of different Fe:O ratios with a rate reaching 1 cm/h. The large temperature gradient associated with optical heating proved beneficial for suppression of eutectoid decomposition occurring at 570 °C.

4.1 The Fe–O system

The phase diagram of the Fe–O system has been reported by Darken and Gurry [46, 47] in the 1940s (Fig. 4.1). Three solid oxide phases were found to occur in this system, hematite, Fe_2O_3 , magnetite, Fe_3O_4 , and wüstite, FeO. Determination of the expansion of the wüstite field has been subject to a larger number of detailed experimental studies, e.g. [46, 25, 66, 162]. Available data were evaluated and used to develop a self-consistent thermodynamic model of the system [157]. Interestingly, the wüstite field although being exceptionally wide, ranging from approximately

45.5 at% Fe ($\text{Fe}_{0.835}\text{O}$) at 1419°C on the iron-poor side to 48.8 at% Fe ($\text{Fe}_{0.954}\text{O}$) on the iron-rich side, does not cover the stoichiometric composition FeO. At normal pressure, the phase field narrows with decreasing temperature until eutectoid decomposition at $T_e \approx 561^\circ\text{C}$ according to



Stoichiometric wüstite was obtained at pressures above 36 kbar and 770°C by reacting non-stoichiometric wüstite, $\text{Fe}_{0.950}\text{O}$, with metallic iron [83]. Thermodynamic calculations [57] confirm the effect of pressure on the extent of the wüstite field by shifting the eutectoid point towards lower temperature and higher iron content.

Wüstite crystallizes in a defect rock salt type structure. Deviations from stoichiometry result from cation vacancies V''_{Fe} whose charge is compensated by two Fe^{3+} ions on (octahedrally coordinated) lattice sites. For each vacancy a Frenkel defect is created by transferring a Fe^{3+} to a tetrahedral interstitial site leaving a double charged vacancy



thus doubling the number of vacancies resulting from non-stoichiometry. In view of their high concentration it is more than likely that the individual defects interact with each other forming clusters. Roth [138] proposed a model of 2:1 cluster consisting of two vacancies in the vicinity of a trivalent iron in a tetrahedral vacancy. Better agreement with experimental data was obtained if aggregates based on 4:1 clusters were assumed, e.g. the so-called Koch-Cohen cluster [87] is composed of 4 interstitial irons and 13 vacancies. Different types of clusters may coexist with the predominant cluster depending on composition and temperature, e.g. for near-stoichiometric samples at high temperature larger clusters dissociate into 4:1 units. It is quite possible that regions of different short-range ordering correspond to subfields within the wüstite field proposed by some authors [162, 109, 44].

An alternative representation of the Fe–O system is the predominance diagram drawn in Fig. 4.2 also containing plots of oxygen fugacity for different gas mixtures. It is evident that an extremely low oxygen fugacity is required to stabilize iron(II) oxide, 10^{-8} bar at melting temperature, and well below 10^{-20} bar at 700 °C. This is way lower than the total pressure in interstellar space!

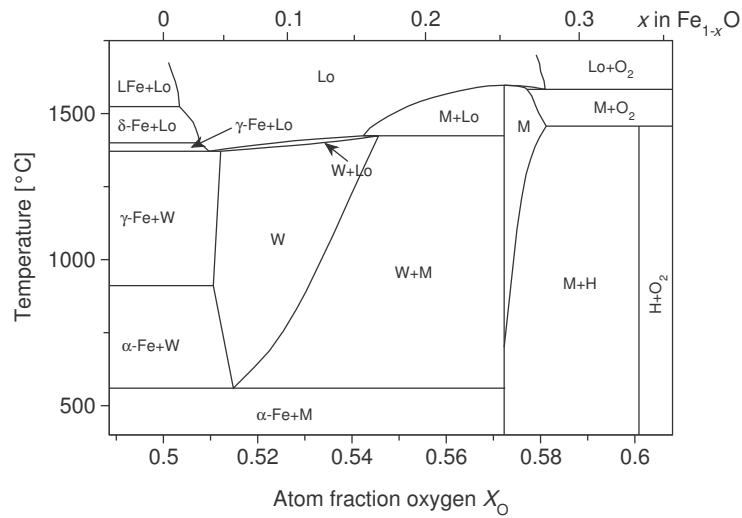


Figure 4.1: Phase diagram of the Fe–O system (after Darken and Gurry [47]). W = wüstite, M = magnetite, H = hematite, Lo = liquid oxide, LFe = liquid iron, α , γ , δ = iron modifications.

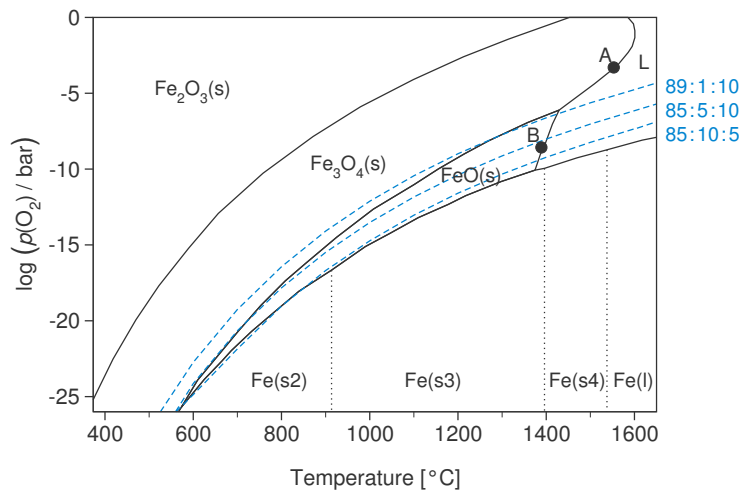


Figure 4.2: Calculated predominance diagram of the Fe–O system. The blue dashed lines correspond to calculated oxygen fugacities of different gas mixtures with compositions given as $p_{Ar} : p_{CO} : p_{CO_2}$ near the right edge of the graph. Dots annotated “A” and “B” point the measured melting temperatures of iron oxide in different atmospheres (refers to Sect. 4.2).

4.2 Thermal analysis

The most obvious raw material for the growth of wüstite crystals, iron(II) (“ferrous”) oxide, is commercially not available. Iron oxide is sold only in the form of iron(III) (“ferric”) oxide or as a mixture of both, ferrous and ferric oxides. For the experiments described here, i.e. for the growth of wüstite, either iron oxide could be used and treated in the proper atmosphere to adjust the Fe : O ratio. But with respect to other running projects dealing with the growth of multinary compounds containing Fe²⁺ ions, e.g. olivine, (Mg,Fe)₂SiO₄, where precise stoichiometry of the raw material has to be known at moment of preparing the oxide mixture, iron(II) oxalate appeared to be the most convenient chemical. The advantages over e.g. iron(II,III) oxide are obvious; iron occurs exclusively as Fe²⁺ and the volatile constituents can be easily removed by thermolysis.

Before running the growth experiments, the raw material, iron(II) oxalate dihydrate, FeC₂O₄ · 2H₂O (Alfa Aesar, Puratronic[®], 99.999%), was examined by differential thermal analysis (DTA) with simultaneous gravimetry (TG) using a Netzsch STA 409C (DTA/TG) or Netzsch STA 449C “Jupiter” (Differential Scanning Calorimetry (DSC)/TG) apparatus in different atmospheres. The measurements were carried out with heating/cooling rates of ±10 K/min in flowing atmosphere (20...50 ml/min).

4.2.1 Decomposition of iron oxalate

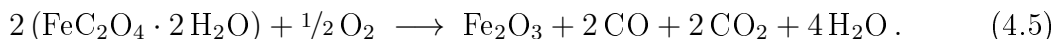
Upon heating, iron oxalate dihydrate splits off water at temperatures around 200 °C (Fig. 4.3). Further heating in an virtually oxygen-free environment leads to decomposition into iron(II) oxide, carbon monoxide, and carbon dioxide. The decomposition can be described by the reaction equation



Mass change of the sample can be easily calculated knowing the molar masses m_i of the involved species,

$$\Delta m_{(1)} = \left(1 - \frac{m_{\text{FeO}}}{m_{\text{FeC}_2\text{O}_4} + 2m_{\text{H}_2\text{O}}} \right) \times 100\% = 60.06\%. \quad (4.4)$$

If thermolysis is performed in an oxygen-containing ambient, e.g. air, then iron(III) oxide may be formed instead according to



In this case the expected mass change of the measured sample will be less, namely

$$\Delta m_{(2)} = \left(1 - \frac{m_{\text{Fe}_2\text{O}_3}}{2(m_{\text{FeC}_2\text{O}_4} + 2m_{\text{H}_2\text{O}})} \right) \times 100 = 55.62\%. \quad (4.6)$$

The experimentally obtained values confirm that the decomposition of iron(II) oxalate indeed follows reaction (4.3) in an oxygen-free ambient. If processed in air, reaction (4.5) leading to the formation of Fe_2O_3 , i.e. decomposition of iron oxalate and oxidation of the resulting FeO , takes place [18].

4.2.2 Melting of ferrous oxide

After decomposition the material was further heated until melting was observed. In high purity (5N) argon, during the first heating cycle an endothermic peak occurred at 1379°C (Fig. 4.4) attributed to melting of the sample. The onset of this peak is not perfectly shaped. During the first melting of a powder sample a “delayed” melting could possibly occur due to bad thermal contact of sample and crucible. Taking into account the small shoulder at the peak’s left flank, the onset temperature could be 1372°C as well. According to the phase diagram in Fig. 4.1 melting temperature of FeO is in the range $1365^\circ\text{C} \leq T_{\text{m}}^{\text{FeO}} \leq 1420^\circ\text{C}$, depending on the oxygen content, hence this first peak can be attributed to the melting of FeO . In subsequent heating cycles the measured melting temperature increased stepwise until a temperature of $\approx 1560^\circ\text{C}$ was reached. This is definitively higher than the maximum melting temperature of any wüstite composition and approaches the melting temperature of magnetite, $T_{\text{m}}^{\text{Fe}_3\text{O}_4} \approx 1592^\circ\text{C}$. The conclusion must be drawn that during the measurement the sample is slowly oxidized. Oxygen fugacity of pure Ar is $p_{\text{O}_2}(\text{Ar}) = 0$ for all temperatures. However, residual impurity of the used gas may be a continuous source of oxygen. If air is assumed to be the main impurity then oxygen fugacity of 5N Ar reaches a level of 2×10^{-6} bar. According to the predominance diagram the observed melting temperature of 1560°C corresponds to a higher

oxygen fugacity, namely $\approx 5 \times 10^{-4}$ bar (point “A” in Fig. 4.2). Consequently, there must be another yielding source of oxygen, most likely gas adsorbed at the inner walls of the apparatus or thermal setup including sample holder, efficient enough to drive the observed oxidation process.

The same measurements were carried out in a reactive atmosphere composed of 85 vol% Ar, 5 vol% CO, and 10 vol% CO₂, chosen on the basis of the predominance diagram (Fig. 4.2). A gas mixture containing CO₂ and CO in 10:1 ratio in Ar touches the FeO predominance field at high temperatures but is generally too oxidizing at lower temperatures: In such mixture Fe₃O₄ will be formed already at temperatures above the eutectoid decomposition of wüstite. A mixture with CO₂:CO of 5:10 comes up to the lower border of the FeO predominance field and implies the danger of formation of metallic iron that easily alloys any metal crucible. A good compromise appears to be an atmosphere containing CO₂:CO in a ratio of 10:5 in Ar — the oxygen fugacity of such an atmosphere lies well inside the FeO predominance field over a wide temperature range. Indeed, as evidenced by DTA melting experiments (Fig. 4.5), such a gas mixture stabilizes ferrous oxide. During numerous melting cycles the melting temperature remained unchanged indicating an unchanged composition of the material. The average measured melting temperature of wüstite $T_m^{\text{FeO}} \approx 1389^\circ\text{C}$ nearly perfectly agrees with that read from the predominance diagram, i.e. the interception of the FeO(s)–L line with the $p_{\text{O}_2}(T)$ curve of the used gas mixture (point “B” in Fig. 4.2).

4.3 Crystal growth

Owing to large temperature gradients, the micro-pulling-down technique appeared predestined for the growth of wüstite single crystals. High cooling rates associated with high pulling speeds are expected to be crucial for conservation of the wüstite phase that is unstable at room temperature. The starting material was melted in an inductively heated platinum crucible with an inner diameter of 13 mm and total height of 35 mm. The orifice at the tip of the conical bottom had an inner diameter of about 0.8 mm. The crucible was covered on top with a platinum lid and placed on an alumina pedestal. Porous alumina tubes were used for thermal insulation. The experiments were carried out in a water-cooled vacuum chamber evacuated to

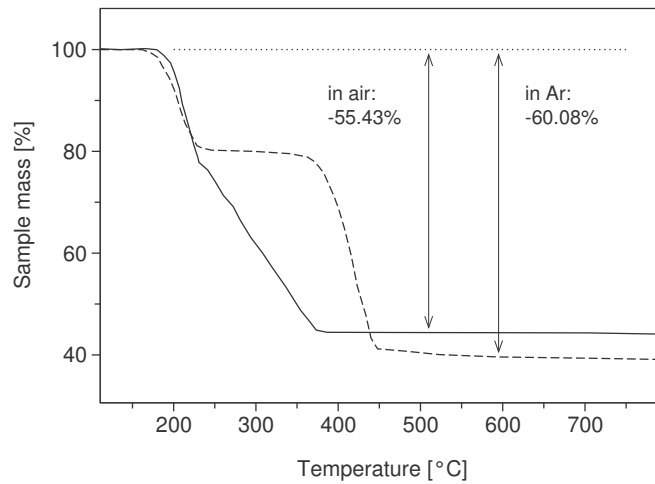


Figure 4.3: TG curves of $\text{FeC}_2\text{O}_4 \cdot 2\text{H}_2\text{O}$ thermolysis in air (solid curve) and 99.999% Ar (dashed curve). The first step around 200°C corresponds to the loss of water, the second step above 400°C to the decomposition of oxalate and the associated release of CO/CO_2 according to Eqns. (4.3) and (4.5).

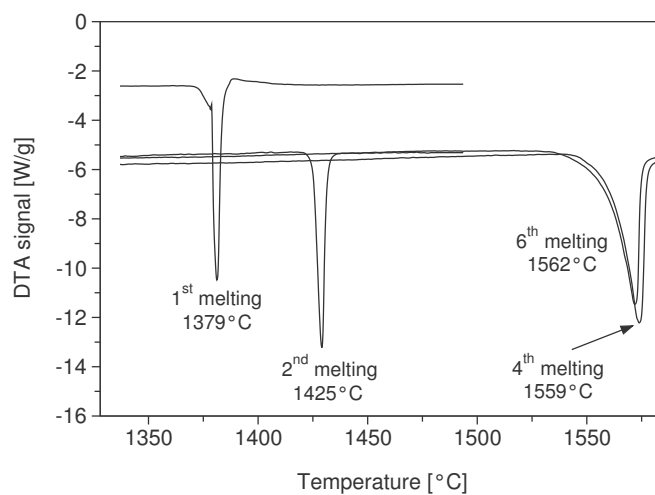


Figure 4.4: DTA curves of successive melting cycles of ferrous oxide in 99.999% Ar.

$< 10^{-2}$ mbar and refilled to normal pressure with a gas mixture of 5 vol% CO + 10 vol% CO₂ + 85 vol% Ar.

First crystals were grown on YAG (Y₃Al₅O₁₂) or sapphire (Al₂O₃) seeds. As soon as sufficient solidified material was produced, randomly oriented FeO chips were used as seeds. The crystals were pulled at rates between 0.5 and 50 mm/min. Like many other oxide melts, the FeO melt wets platinum almost perfectly. At lower pulling rates ($v \lesssim 1$ mm/min), the diameter of the growing crystal was easily maintained at around 2 mm by changing the power supplied to the crucible. Showing the typical behavior of wetting melts, the diameter of the growing crystal increased at higher pulling rates and increasing heating power. At pulling rates exceeding 10 mm/min, the diameter self-adjusted to some value that was probably determined by limited mass flow through the capillary. For the given crucible geometry and a crystal diameter of 5 mm, the flow velocity in the capillary was about 40 times larger than the pulling rate, i.e., up to 800 mm/min. This is more than twice as much as the maximum value reported previously [39]. At this stage, changing the heating power hardly affects the growth because of the thermal inertia of the set-up and the vast amount of latent heat released during solidification.

The grown crystals were of practically black color with metal-reminding shiny surface. Crystals grown at low pulling rate had a rod-like shape and exhibited well developed facets. The typical habit of crystals grown at high pulling rates is shown in the right-hand photo in Fig. 4.6. Although grown in a rather uncontrolled fashion in terms of diameter control, also these crystals show extended facets on their outer surface indicating at least decent crystalline perfection.

4.4 Characterization by X-ray diffraction

X-ray powder diffraction analysis was used to determine phase constitution of the grown crystals. Samples were fine ground in an agate mortar and their powder patterns recorded in Bragg-Brentano geometry using Cu-K α radiation. Built-in routines of the data recording and analysis software were used to correct for the $\alpha_1\alpha_2$ doublet (Rachinger correction).

All patterns except that of the crystal grown at highest pulling rate (50 mm/min) contained additional peaks caused by the presence of magnetite (Fig. 4.7). Simul-

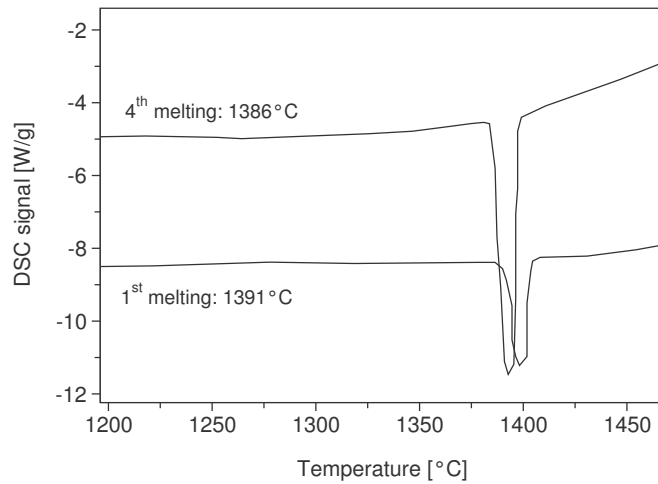


Figure 4.5: DSC curves of a first and fourth melting cycle of ferrous oxide in a mixture consisting of 85 vol% Ar, 5 vol% CO, and 10 vol% CO₂. The difference in the onset lies within the experimental error.

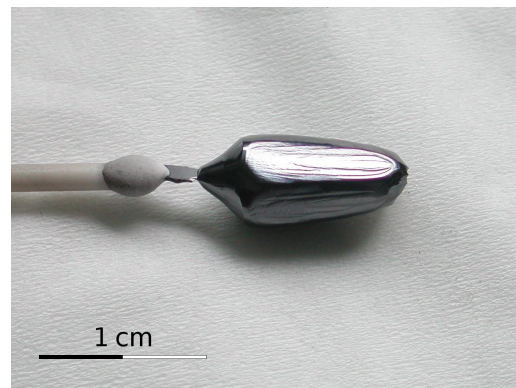


Figure 4.6: Wüstite crystals grown at low pulling rate (1.0 mm/min, left) and high pulling rate (50 mm/min, right).

taneously, the wüstite reflections were split into two separate reflections of similar intensity, one occurring at lower, the second at higher diffraction angle.

The crystal grown at 50 mm/min was single phase wüstite. Using the empirical relation reported by Levin & Wagner [95] its composition Fe_{1-x}O can be calculated:

$$a/\text{Å} = 4.3370 - 0.5290 \cdot x. \quad (4.7)$$

The four strongest wüstite reflections (111, 200, 220, and 311) were fitted with simple Gauss functions to extract their diffraction angles 2Θ . Spacing of the corresponding lattice planes, d_{hkl} , can be calculated from Bragg's law

$$d_{hkl} = \frac{\lambda}{2 \sin \Theta} \quad (4.8)$$

where λ is the wavelength of the incident X-ray beam, here 1.54056 Å. For cubic crystals

$$d_{hkl} = \frac{a}{\sqrt{h^2 + k^2 + l^2}}. \quad (4.9)$$

In Fig. 4.8 the measured d_{hkl} are plotted versus $(\sqrt{h^2 + k^2 + l^2})^{-1}$. The wüstite lattice parameter is obtained from a simple slope fit through the data points, $a = (4.3074 \pm 0.0009)$ Å, and corresponds to wüstite of composition $\text{Fe}_{1-(0.056 \pm 0.002)}\text{O}$. From routinely performed test of the diffractometer routinely using silicon standard samples the experimental error of the diffraction angle measurements is estimated to $\delta(2\Theta) \lesssim 0.03^\circ$ for small diffraction angles and decreases for larger angles. Significant uncertainty of the determined wüstite composition may originate from the choice of the composition–lattice parameter relation. Hayakawa et al. [71] listed a handful of sources that “agree reasonably well” with different sources yielding values of x between 0.0606 and 0.0524, so that the standard deviation of the average value is $\sigma_x = 3.3 \times 10^{-3}$ for medium wüstite concentrations. For iron-rich and iron-deficient wüstite compositions the differences between the various sources become larger. Therefore the above named relation established by Levin & Wagner will be used to convert between lattice parameter and composition.

In crystals grown at lower pulling rate, below 10 mm/min, (i) magnetite reflections and (ii) splitting of all wüstite reflections was observed. Lattice parameter and

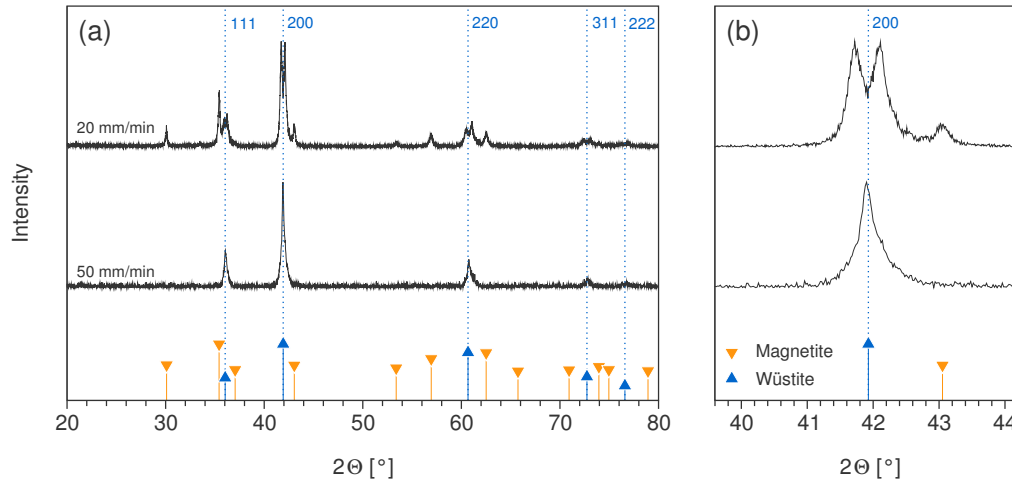


Figure 4.7: X-ray powder diffraction patterns of wüstite crystals grown at different pulling rates. A closer look (b) uncovers splitting of wüstite reflections into two separate peaks. Diffraction angles and relative intensities of magnetite (red dots, PDF no. 019-0629) and wüstite (PDF no. 006-0615) from the Powder Diffraction File [77].

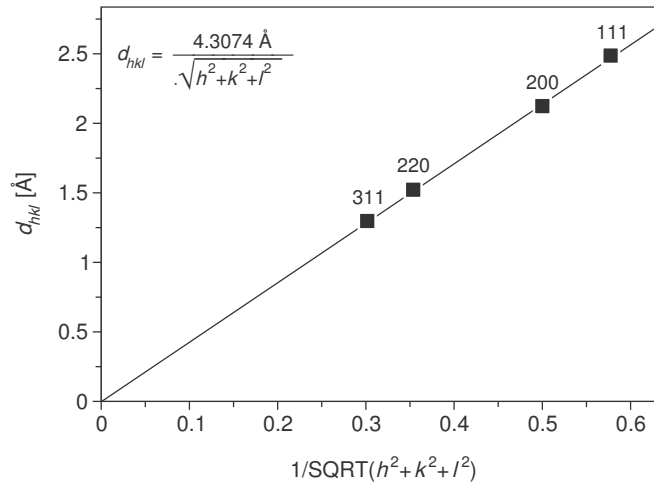


Figure 4.8: Measured lattice plane spacing as a function of $1/\sqrt{h^2+k^2+l^2}$ for the most intense wüstite diffraction peaks. The slope of the linear fit is the wüstite lattice parameter a .

composition of the contained wüstite phases can be calculated following the above procedure, the results are summarized in Table 4.1. As above, the given uncertainty of the lattice parameter is the statistical error of the regression; that of composition is roughly double the lattice constant uncertainty. Fig. 4.9 depicts the situation in terms of location relative to the wüstite field. Readily, composition of the single phase wüstite crystal (sample W-5) is near the eutectoid composition as expected from the predominance diagram. Wüstite compositions in crystals containing two wüstite phases are one iron-poor and the other iron-rich. The latter is nearly stoichiometric and located outside the wüstite field. This observation is in agreement with reports by Otsuka et al. [129] on isothermal decomposition of thermally grown wüstite scales.

4.5 Eutectoid decomposition of wüstite

When wüstite of eutectoid composition, i.e. $x = x_e \approx 0.054$, is cooled slowly below the eutectoid temperature $T_e \approx 561^\circ\text{C}$ it decomposes directly into a mixture of magnetite and α -iron. For calculating the amounts of the individual phases it is convenient to express composition in terms of atomic fraction of oxygen, X , that is connected with the parameter x in Fe_{1-x}O by the simple relation

$$X = \frac{1}{2-x}. \quad (4.10)$$

The magnetite fraction in the resulting two-phase mixture can be calculated using the lever rule

$$Y = \frac{X_e - X_{\text{Fe}}}{X_{\text{Fe}_3\text{O}_4} - X_{\text{Fe}}}. \quad (4.11)$$

Since $X_{\text{Fe}} = 0$

$$Y = \frac{X_e}{X_{\text{Fe}_3\text{O}_4}} = \frac{0.5139}{0.5714} = 89.9\%. \quad (4.12)$$

If wüstite of hypo-eutectoid ($x < x_e$) or hyper-eutectoid ($x > x_e$) composition is slowly cooled, decomposition starts with precipitation of either α -Fe or magnetite when the wüstite field is exited. Upon further cooling precipitation keeps going on, but the wüstite composition continuously changes until the eutectoid composition x_e is reached. The wüstite of eutectoid composition undergoes complete decompo-

Sample	Pulling rate [mm/min]	Wüstite I		Wüstite II	
		$a/\text{Å}$	x	$a/\text{Å}$	x
W-1	0.50	4.3282 ± 0.0010	0.017	4.2920 ± 0.0011	0.085
W-3	0.50	4.3285 ± 0.0012	0.016	4.2884 ± 0.0004	0.092
W-5	50.0	4.3074 ± 0.0009	0.056	—	—
W-6	10.0	4.3251 ± 0.0013	0.023	4.2860 ± 0.0017	0.096

Table 4.1: Lattice constant and composition of the wüstite phases detected in the grown crystals.

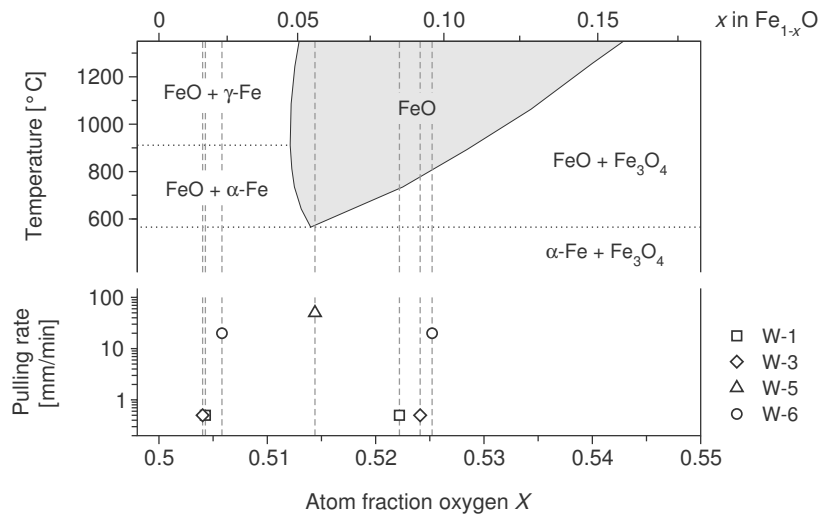


Figure 4.9: Detail of the Fe–O phase diagram showing the wüstite existence field (gray shaded area) and composition of the grown crystals (colored dashed lines).

sition into α -Fe and magnetite. Magnetite fraction in the final solid depends upon the initial composition and ranges from 89.5% for iron-rich to 93.4% for iron-poor wüstite. Due to the small fraction of α -Fe in the eutectoid mixture and the relatively low sensitivity of X-ray powder diffraction technique, α -Fe reflections will be observable in powder patterns only in an advanced stage of transformation, that is if nearly all of the wüstite is transformed. In this study that was not the case even for the lowest pulling rate.

Kinetics of the eutectoid decomposition of wüstite has been subject of number of investigations, e.g. [38, 74, 76, 156, 67, 167, 129], mainly by X-ray diffraction, magnetic measurements and/or electron microscopy examination. Direct transformation of wüstite into magnetite and α -Fe mixture of lamellar, pearlite-like texture was observed at temperatures not far below the eutectoid temperature with a maximum transformation velocity around 480 °C [76, 129]. At lower temperatures but above 200 °C precipitation of magnetite occurs, also for hypo-eutectoid samples, accompanied by an increase of the wüstite lattice parameter and, hence, iron content. Stølen et al. [156] ascertained the maximum composition of the iron-rich wüstite to be nearly stoichiometric, $\text{Fe}_{0.99}\text{O}$. The metastable iron-rich wüstite decomposes slowly according to reaction Eq. 4.1. Below approximately 200 °C the transformation practically comes to a halt. According to newer results obtained by *in-situ* measurements [129], at moderate supercooling below the eutectoid temperature (around 400 °C), transformation starts from a shift of the wüstite composition towards lower iron content accompanied by the occurrence of a new wüstite phase of increased iron content, both coexisting over quite an extended range of time. The new wüstite grows at the cost of the parent wüstite and starts to decompose into magnetite and α -Fe only after the parent wüstite is consumed entirely.

According to these observations, two different reaction mechanisms for disproportionation of wüstite are discussed in literature. The spinodal type decomposition [5] involves a three stage mechanism beginning from the formation of two wüstite phases, one being iron-rich, the other iron-poor. During the second stage, the latter decomposes into magnetite and iron-rich wüstite. This process seems to occur faster for lower temperature due to the diminishing effect of disorder entropy on Gibbs energy. Finally, a stable mixture of α -Fe and magnetite is formed from the iron-rich metastable wüstite in a third stage. Every single stage lowers the Gibbs en-

ergy of the system thus providing the thermodynamic driving force for the process. The second mechanism assumes direct precipitation of magnetite with simultaneous change of wüstite composition towards the stoichiometric composition in a first step, and transformation of the formed iron-rich wüstite into α -Fe and magnetite as final step. Main argument for one or the other model is occurrence of a second wüstite phase of lower iron concentration [156] as observed e.g. by Andersson and Sletness [5] and Otsuka et al. [129]. However, reasoning is handicapped by transient emergence of metastable configurations, and most studies bear on snap-reading. Only Otsuka et al. report on *in-situ* measurement. In their published spectra a shift of the parent wüstite's reflections towards larger diffraction angles (corresponding to a decrease in iron) is evident before the second wüstite phase occurs. However, for unknown reasons they did not comment this fact. The experiments described here clearly support the spinodal type decomposition model.

Preferred precipitation of magnetite can be elucidated considering kinetics of the possible nucleation processes. The number of stable nuclei created per unit time and unit volume, N , is proportional to

$$N \propto \exp\left(-\frac{W^* + Q}{kT}\right) \quad (4.13)$$

where W^* is the energy barrier to nucleation, Q the activation energy for diffusion in the solid, and k the Boltzmann constant. W^* is the work necessary to form a critical nucleus of radius r^* , i.e. the maximum value of the $W(r)$ curve. Dependence of W on the radius r considers the change in Gibbs energy per volume, ΔG_V , strain associated with the change in volume, and work necessary to form the interface between the two phases. For a spherical nucleus

$$W = -\frac{4}{3}\pi r^3(\Delta G_V - \epsilon) + 4\pi r^2\sigma \quad (4.14)$$

where σ is the specific interfacial energy. The strain energy ϵ is proportional to the bulk modulus K and strain γ , $\epsilon \propto K\gamma^2$. The size of the critical nucleus and the height of the barrier W^* is obtained by setting the derivative dW/dr to zero,

solving for r , and inserting r^* into 4.14

$$W^* = \frac{16}{3}\pi \frac{\sigma^3}{(\Delta G_V - \epsilon)^2}. \quad (4.15)$$

From a common tangent construction to the free energy vs. composition curves it can be estimated [67] that ΔG_V should be significantly larger for the formation of a magnetite nucleus in a wüstite matrix compared to the a α -Fe nucleus. Furthermore it is reasonable to assume that surface energy associated with a magnetite nucleus is small since this nucleation is coherent. From these consideration follows that most likely the nucleation barrier W^* is much smaller for magnetite than for α -Fe, and consequently stable magnetite nuclei are formed at higher frequency.

In Fig. 4.10 the isothermal transformation diagram (or time-temperature-transformation diagram) of the FeO decomposition is reproduced after Gleeson et al. [67]. Dashed lines mark beginning (1% line) and completion of transformation (100% line). On the left of the 1% line no transformation occurs, right of the 100% line all solid is transformed. Dotted lines denote the same boundaries but determined on the basis of electron microscope examination instead of optical microscopy. The solid line depicts the trajectory of sample cooled at a rate of 2 K/s. It is evident that this cooling rate is the lowest for which decomposition can be suppressed. Assuming that the crystal is pulled through a static temperature field generated by the heating elements, the thermal gradient inside the material, G_T , can be estimated knowing that for a pulling rate of 50 mm/min practically no transformation occurs, but for a rate of 10 mm/min it does:

$$50 \text{ mm/min} \cdot G_T > 2 \text{ K/s}$$

$$10 \text{ mm/min} \cdot G_T < 2 \text{ K/s}$$

so that

$$24 \text{ K/cm} < G_T < 120 \text{ K/cm}.$$

It is commonly believed that the (axial) temperature gradient for this growth technique is in the range of at least a few 100 K/cm [140, 141]. Some authors even quote values beyond 1000 K/cm [170]. At least for the inductively heated variant

involving relatively massive thermal insulation such high values appear rather questionable. Maier [99] used a thermocouple “seed” to monitor temperature at the tip of the growing crystal in a setup very similar to the one used here. From these measurements he derived temperature gradients in front of the interface of 400 K/cm and 230 K/cm for the growth of Cr:Al₂O₃ (ruby) and Yb:Y₃Al₅O₁₂, two compounds with melting temperatures around 2000 °C. In view of these values the estimation of G_T for the case of wüstite with considerably lower melting temperature is very reasonable.

4.6 Conclusions

Thermal analysis evidenced that a gas mixture of 5 vol% CO + 10 vol% CO₂ + 85 vol% Ar yields an oxygen fugacity nearly perfectly fitting the existence field of wüstite over an extended temperature range. In such atmosphere, wüstite crystals of near-eutectoid composition were successfully grown using the micro-pulling-down technique. Powder diffraction patterns of these crystals show reflections caused by the presence of magnetite stemming from partial disproportionation below the eutectoid temperature. Two distinct wüstite phases, one being nearly stoichiometric, the other iron-deficient were identified in those crystals. There is no evidence that these two wüstite phases form at the same time, rather but the occurrence of iron-poor wüstite supports the model involving spinodal decomposition of wüstite before the eutectoid transformation.

Disproportionation of wüstite can be avoided by sufficiently fast cooling of the grown crystals. From kinetic studies a minimum cooling rate of about 2 K/s can be estimated to suppress disproportionation entirely. In the experiments, a pulling rate of 50 mm/min was enough to satisfy this requirement. But also crystals grown at much lower pulling rates below 1.0 mm/min consist predominately of wüstite phase.

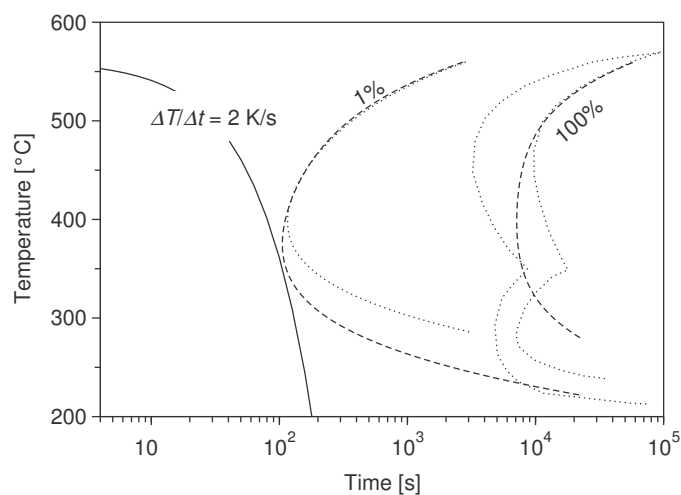


Figure 4.10: Isothermal transformation diagram of FeO decomposition (after Gleeson et al. [67]). Dashed lines were determined by optical, dotted lines by electron microscope examination. The solid line depicts the cooling trajectory for a sample cooled at constant rate of 2 K/s.

5 Chromium distribution coefficient in ruby crystals

Chromium doped corundum, $\text{Cr}^{3+}:\text{Al}_2\text{O}_3$, commonly called “ruby”, is probably the first material grown in single crystalline form on an industrial scale. In the late 19th century Auguste Verneuil developed a flame-fusion technique yielding mm-sized crystals that were presented at the Paris World Fair in 1900. Details of the growth process were published in 1902, and industrial production started before the end of the first decade of the 20th century in Verneuil’s laboratory in Paris and concurrently in Monthey, Switzerland [112, 113, 147]. A few years later, in 1907, the worldwide ruby production passed the 1 ton barrier [70]. Flame-fusion grown ruby crystals were used for gems, watch and high precision instrument bearings, later also for thread guides in weaving machines, phonograph needles and balls in ball-point pens etc. The stormy development of laser technology kicked off by Maiman’s achievement – the first ever lasing action in a ruby single crystal in 1960 [102, 101] – created a demand for crystals of much higher quality and size than could be achieved by Verneuil’s method. In the preceding decade the Czochralski pulling method had taken great technological progress, triggered by the probably most revolutionary invention of the 20th century – the semiconductor transistor [58]. Based on the experiences gained during the development of a growth process for semiconducting materials, first germanium and later silicon, it could be demonstrated that the Czochralski growth process yielded crystals of greatly reduced residual stress and improved homogeneity as compared to Verneuil crystals [103, 139].

The crystal growth literature contains numerous reports on successful growth of ruby single crystals using various techniques including the Czochralski [130, 123, 89, 88, 133], Verneuil [89, 4, 68, 153] and other melt growth techniques [55, 143, 155, 100], the hydrothermal method [118, 178], high-temperature solution (flux) growth [117,

96, 3, 94], and growth from the gas phase [122]. However, detailed reports on chromium segregation are only rarely found and the values of the distribution coefficient given by different groups vary in a wide range [89, 155, 51, 100]. Kvapil et al. [89] investigated the chromium distribution in Verneuil- and Czochralski-grown rubies and found that the chromium distribution coefficient is critically dependent on oxygen fugacity during growth. For Czochralski pulling in an atmosphere containing 1...2%¹ oxygen chromium was preferentially incorporated with a maximum distribution coefficient $k \approx 1.2$. Both higher and lower oxygen contents led to a lower distribution coefficient. In reducing conditions realized by addition of 2% hydrogen to the protective argon atmosphere the distribution coefficient stepped down to $k \approx 0.2 \dots 0.3$. Quantitative analysis was handicapped by excessive evaporation of chromium species under such conditions.

5.1 Phase diagram and chromium equilibrium distribution coefficient

From the experimentally determined phase diagram of the $\text{Al}_2\text{O}_3\text{-Cr}_2\text{O}_3$ system going back to the 1930s [32, 1, Fig. 309] and reproduced in Fig. 5.1, valuable information about the equilibrium distribution coefficient can be extracted. According to this study, Al_2O_3 and Cr_2O_3 form liquid and solid solutions in the whole concentration range with a Cr_2O_3 equilibrium distribution coefficient $k_0 > 1$. With increasing chromium concentration in the melt, the distribution coefficient decreases monotonously from its maximum value of about 2.2 for low chromium concentrations to unity on the Cr_2O_3 rich side of the system. As stated by the authors, the experiments were done in an “oxidizing” atmosphere, most likely air. Chromium(III) oxide, Cr_2O_3 , must therefore be assumed to be the dominating chromium species in the melt (see below). In most melt growth processes, however, oxygen fugacity is set significantly lower, $p_{\text{O}_2} \lesssim 10^{-2}$ bar in order to prevent the crucible typically made of iridium, molybdenum, or tungsten from oxidation. Under these conditions

¹In the original work an oxygen concentration of 0.01...0.02% is given. Having in mind (i) that addition of a few percent oxygen to protective gas was a very common practice (e.g. [42][23][31]) in crystal growth of oxides and (ii) the accuracy of flow meters available, in all probability the authors meant 1...2%.

one must take into account occurrence of other chromium oxidation states.

The relevant region of the calculated predominance diagram of the Cr–O system is drawn in Fig. 5.2 and considers the following redox equilibria:



At the melting temperature of corundum (2054°C, dashed vertical line in Fig. 5.2), Cr_2O_3 is stable in a wide range of oxygen fugacity expanding with lessening temperature. The large predominance field Cr_2O_3 makes immediately clear why ruby can be grown in adequate quality without special care for the atmosphere. At low oxygen fugacity and high temperatures, however, chromium(II) oxide, CrO, may be formed. Although not yet prepared as a pure stable bulk phase, it is proven that occurrence of CrO reduces the melting temperature of chromium oxide containing melts drastically [127, 110, 48]. The range of oxygen fugacity applicable in crystal growth is limited by the predominance field of chromium metal which would alloy the crucible. This can practically be excluded as long as $p_{\text{O}_2} > 10^{-8}$ bar.

A peculiarity visible in the upper, high oxygen fugacity part of the diagram should be noted here. As discussed in Sect. 2.1, for metals and metal oxides the temperature-dependent contribution to the Gibbs energy change upon oxidation arises from the “consumption” of gaseous oxygen. The entropy change ΔS for oxidation is therefore negative. Since

$$\Delta G = \Delta H - T\Delta S \quad (5.2)$$

rising temperature favors the reverse reaction, i.e. the reduction. According to the available thermodynamic data, for reaction (5.1e) this holds only for relatively low temperatures of very few 100°C. At elevated temperatures around 700°C the sign of ΔS changes, and with further increasing temperature oxidation becomes favored again. As a consequence, at high temperatures the CrO_2 field predominance

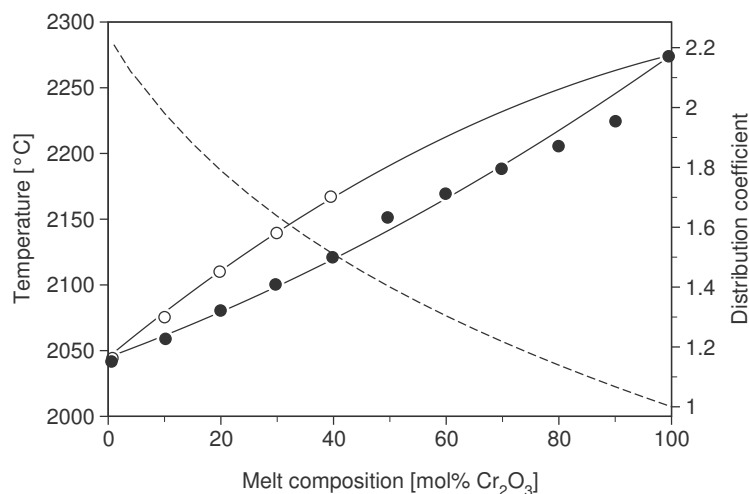


Figure 5.1: $\text{Al}_2\text{O}_3\text{-Cr}_2\text{O}_3$ phase diagram after Bunting [32]. The author’s original data points were fitted with parabolas to calculate the (equilibrium) distribution coefficient according to the definition $k_0 = c_s/c_L$ (dashed line).

diagram expands to lower oxygen fugacity (dotted line in Fig. 5.2). Decomposition of CrO_2 upon heating to about 300°C in ambient air was confirmed experimentally by Singh et al. [154]. But there is no reliable report on the occurrence of the reverse reaction which should take place around 1600°C . On the other hand, Kvapil et al. [89] measured a decreasing chromium distribution coefficient for growth ambient containing more than 2% oxygen. Presence of significant amounts of CrO_2 in the melt must be expected to effectively reduce the chromium distribution coefficient. But more likely, the appearance of CrO_2 predominance field at such temperatures is a result of invalid or incomplete data for $\text{CrO}_2(\text{s})$ in the database.

When restricting the treatment to the $\text{Al}_2\text{O}_3\text{-Cr}_2\text{O}_3$ binary diagram, the only chromium species “allowed” to occur is Cr_2O_3 . To include other potentially occurring chromium oxides the system must be extended to include those species. Under typical conditions for melt growth of ruby, i.e. working temperature $T \gtrsim 2050^\circ\text{C}$ and oxygen fugacity $10^{-8} < p_{\text{O}_2}/\text{bar} < 10^{-2}$, the formation of chromium oxides others than Cr_2O_3 and CrO can be excluded. Hence, consideration of the ternary $\text{Al}_2\text{O}_3\text{-Cr}_2\text{O}_3\text{-CrO}$ system, where oxygen fugacity is implicitly variable, accommodates all

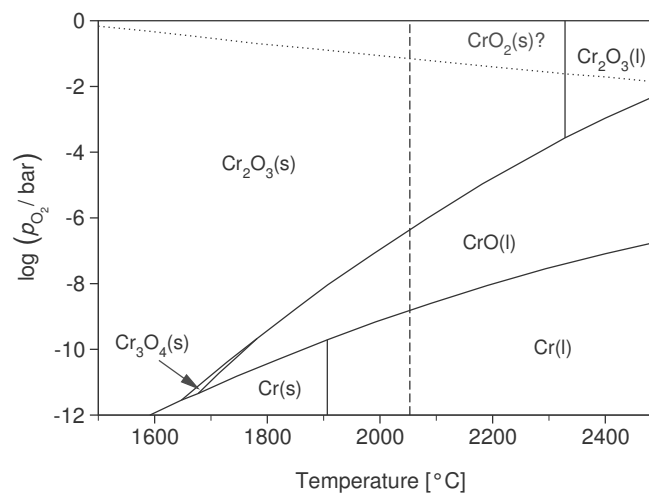


Figure 5.2: Calculated predominance diagram of the Cr–O system. The dashed vertical line represents the melting temperature of Al_2O_3 , i.e. the approximate working temperature during crystal growth. Existence and expansion of the $\text{CrO}_2(\text{s})$ stability field at high temperature is questionable and is probably caused by incorrect thermodynamic data of that phase.

practical melt growth situations.

The phase diagram of the $\text{Al}_2\text{O}_3\text{-Cr}_2\text{O}_3\text{-CrO}$ system can be calculated using the FactSageTM software [11]. The associated data base contains a self-consistent set of thermodynamic data of phases including solid and liquid solutions occurring in the system. The Gibbs energy minimization algorithms of the software allows to calculate and visualize arbitrary representations of the phase diagram, in particular, sections of constant oxygen fugacity through the ternary system. Such sections depicting conditions for growth experiments in different atmospheres are shown in Fig. 5.3. The corresponding liquidus and solidus lines for $p_{\text{O}_2} = 10^{-2}$ bar, 10^{-5} bar, and 10^{-8} bar are drawn in different colors. In an atmosphere containing about 1% of oxygen (blue curve) the experimentally determined phase diagram (Fig. 5.1) of the $\text{Cr}_2\text{O}_3\text{-Al}_2\text{O}_3$ system with a Cr_2O_3 melting temperature of 2257°C and distribution coefficient $k_0 > 1$ is well reproduced. With decreasing oxygen fugacity the melt contains more and more CrO, the melting temperature of the chromium oxide lessens significantly, whereas that of Al_2O_3 remains constant at 2054°C . Between 10^{-4} and 10^{-5} bar oxygen fugacity the slopes of liquidus and solidus curves change sign near pure Al_2O_3 . For lower p_{O_2} addition of chromium oxide to the melt decreases its freezing temperature. It follows that the chromium distribution coefficient is

$$k_0 \begin{cases} > 1 & \text{for } p_{\text{O}_2} \gtrsim 10^{-5} \text{ bar} \\ < 1 & \text{for } p_{\text{O}_2} \lesssim 10^{-5} \text{ bar} \end{cases}$$

Values of the distribution coefficient can be obtained from the sections through the ternary system by reading off coordinates of the calculated liquidus and solidus lines and pairing according to temperature. In Fig. 5.4 the yielded dependence of the equilibrium distribution coefficient on oxygen fugacity is shown. The data points arrange in a nearly linear fashion with a slightly smaller slope for higher p_{O_2} . For the critical oxygen fugacity $p_{\text{O}_2}^*$ at which segregation vanishes, i.e. for which $k_0 = 1$, a value of approximately 2.5×10^{-5} bar can be read off the graph. Crystals grown in such ambient can be expected to show a perfectly even chromium distribution.

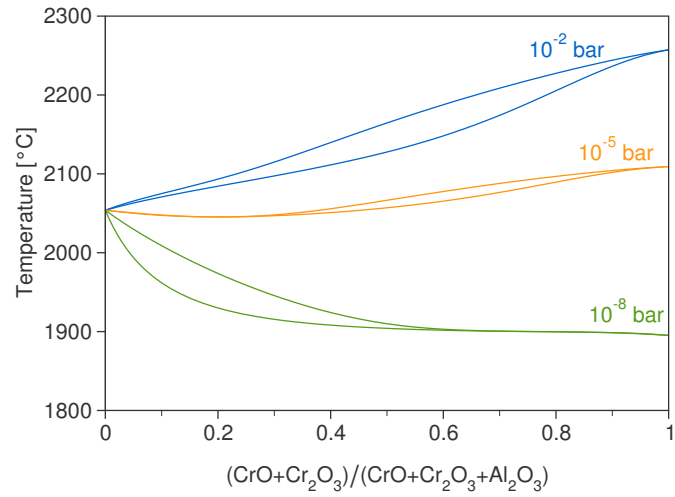


Figure 5.3: Calculated cuts of constant oxygen fugacity through the CrO–Cr₂O₃–Al₂O₃ ternary system.

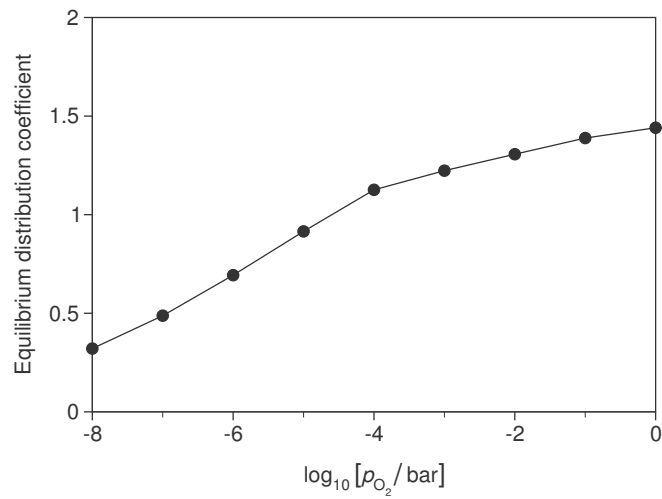


Figure 5.4: Calculated dependence of the chromium equilibrium distribution coefficient k_0 on oxygen fugacity in the growth ambient, p_{O_2} .

5.2 Experimental procedure

5.2.1 Crystal growth

Ruby single crystals were grown using the Czochralski technique. A cylindrical iridium crucible of 41 mm outer diameter and height was heated by the alternating field of a water-cooled copper coil driven by a *rf* generator working at 20 kHz (Fig. 5.5). The crucible was placed inside a ceramic crucible made of porous alumina lined with zirconia felt. On top of the crucible an active afterheater, i.e. cylindrical iridium tube coupling to extra windings of the induction coil, was placed and additionally surrounded by alumina ceramics. This arrangement allows to instantiate low thermal gradients in the enclosed cavity above the melt [135, 64]. Small openings in afterheater and ceramics were left for visual observation necessary during the seeding stage.

After exhausting the growth chamber and refilling with the process gas, the crucible containing the raw material, premelted Al_2O_3 granulate (crushed Verneuil boules supplied by Spolchemie (CZ), purity better 4N) with addition of ≈ 0.5 wt% Cr_2O_3 (Alfa Aesar, 4N7), was slowly heated until the material was entirely melted. After a period of homogenization, an oriented Al_2O_3 seed was slowly approached and dipped into the melt. Melt temperature was then chosen by altering the generator power to slightly melt the seed in order to remove parasitic crystallites eventually giving rise to multi-grain growth. Growth as started by pulling the seed upwards at a rate of typically 2.0 mm/h and switching on the automatic diameter control (ADC) utility. The latter controlled the mass growth rate by continuously weighing the crystal, calculating the weight derivative, and adjusting the generator power to follow the predefined diameter vs. length program. During the process, the mechanical pulling speed was corrected for the melt level fall by the control software so that the vertical velocity at which the crystal-melt interface moved was constantly equal the desired value. After the final crystal length was reached, the crystal was withdrawn from melt and kept a few millimeters above the melt. Then the entire system was slowly cooled to room temperature in 9 (small crystals) to 15 hours.

Following different objectives, three series of crystals were grown:

Series A: Small crystals with a diameter not exceeding 8 mm with masses below

2 g. Owing to the small solidified fraction ($g < 2\%$) chromium concentration of the melt can be considered unchanged and equal the initial value C_{L0} given by the amount of chromium oxide added to the melt. The experiments were conducted in different growth atmospheres with different oxygen fugacities at working temperature (Table 5.1) and aimed at the confirmation of the calculated $k(p_{O_2})$ dependence in Fig. 5.4.

Series B: A small diameter (8 mm) crystal pulled with piecewise different speed. After pulling a length of approximately 20 mm at constant pulling speed the process was paused and continued with altered pulling speed. The crystal was used to assess the growth speed dependence of the chromium effective distribution coefficient. The growth atmosphere contained 90 vol% N_2 and 10 vol% CO_2 giving in an oxygen fugacity at working temperature of ca. 5.7×10^{-3} bar. Chromium concentration in the starting melt was approximately 0.57 wt%.

Series C: Full-sized crystals of 18 mm diameter and masses up to 90 g corresponding to a solidified fraction of the melt up to 75%. These crystals were grown to examine the impact of oxygen fugacity on chromium distribution along the pulling direction. While growing the cylindrical constant-diameter part of the crystals a growth rate variation was triggered by manually reducing the heating power by about 0.7%. The system reacted with an increased mass growth rate that reached typically the fourfold of the steady state value just before the intervention (Fig. 5.14). The automatic diameter control utility of the growth station restored the original growth rate usually within a time span of 30 minutes. During the process, the crucible's outside wall temperature was monitored by a two-color pyrometer.

An example of a ruby crystal of series C is shown in Fig. 5.6. The last-grown part of the crystal is decorated by a spiral-shaped chain of iridium particles stemming from the crucible. The crucible wall is the hottest part in the inductively heated setup. Here iridium is dissolved and transported away caught by the melt convection towards the axis of symmetry and the interface of the growing crystal. The interface is the coldest part in the melt and here iridium precipitates from the supersaturated

	Atmosphere composition [vol%]	p_{O_2} [bar]	C_{L0} [wt%]
Series A			
SAP10-A	100% N ₂	ca. 2×10^{-6}	0.55
SAP10-B	90% Ar + 8% CO + 2% CO ₂	1.1×10^{-5}	0.54
SAP10-C	90% N ₂ + 10% CO ₂	5.7×10^{-3}	0.55
SAP10-D	95% Ar + 5% H ₂ + 6 mbar H ₂ O	8.3×10^{-8}	0.53
Series B			
SAP16	90% N ₂ + 10% CO ₂	5.7×10^{-3}	0.57
Series C			
SAP11	100% N ₂	ca. 2×10^{-6}	0.57
SAP12	92.85% Ar + 5% CO + 2.15% CO ₂	3.3×10^{-5}	0.57
SAP13	75% N ₂ + 25% CO ₂	1.1×10^{-2}	0.38

Table 5.1: Growth atmosphere composition, resulting oxygen fugacity at working temperature (2054°C), and chromium content of the initial melt (C_{L0}).

melt. Often this process is assisted by the presence of oxygen either released from melt components (as it is the case for gallium-containing compounds) or contained in the ambient and the formation of iridium oxide [31].

5.2.2 Determination of chromium concentration

For samples from series A, chemical element analysis was carried out using an inductively coupled plasma optical emission spectrometer (ICP OES) IRIS Intrepid HR Duo (Thermo Electron). The spectrometer was calibrated with simple synthetic solution standards. Samples were ball-milled and analyzed after microwave digestion in a mixture of phosphoric and sulfuric acid at 250°C. The relative standard deviation (RSD) of the analysis was of the order of 2%.

Spatial distribution of chromium in the grown crystals was measured by X-ray fluorescence (XRF) analysis using a FischerScope XRAY XAN spectrometer with a rhodium target tube and nickel primary filter. An accelerating voltage of 50 kV

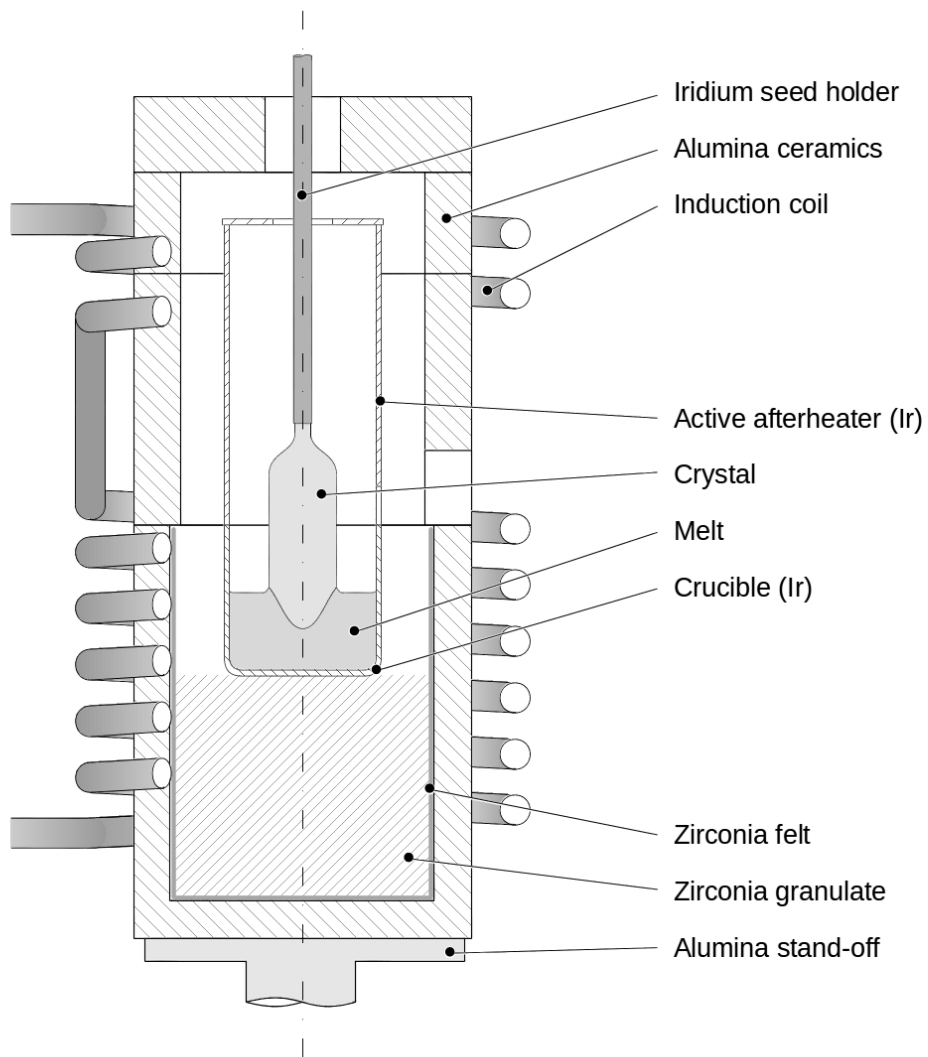


Figure 5.5: Setup for the growth of ruby crystals.



Figure 5.6: Ruby crystal grown by the Czochralski technique. The background grid is $5 \times 5 \text{ mm}^2$.

was applied, the spot size of primary radiation was 1.0 mm, and the net measuring time was 40 s. For quantitative analysis a calibration curve was recorded with four samples of known chromium concentration that had been measured before using ICP OES. Dependence of the Cr- $K\alpha_1$ fluorescence intensity at 5.41 keV on chromium content was measured and fitted with a simple slope function (Fig. 5.7). The obtained calibration function is

$$[\text{Cr}]/\text{wt}\% = \frac{I_{5.41 \text{ keV}}}{8.72 \text{ cps}}. \quad (5.3)$$

High spatial resolution chromium profiles shown in Sect. 5.5 were obtained by electron probe microanalysis (EPMA). A JEOL hyperprobe with Schottky field emission source and equipped with four wavelength-dispersive spectrometers at the electron microscope center at the Technical University Berlin was used in the measurements. Specimen were excited by an electron beam accelerated to 20 keV at probe current of 200 nA. The measuring time per pixel was 70...80 s, the distance between two pixels 10 μm at a beam diameter of approximately 0.1 μm . The spectrometer was calibrated with the same samples as the XRF spectrometer.

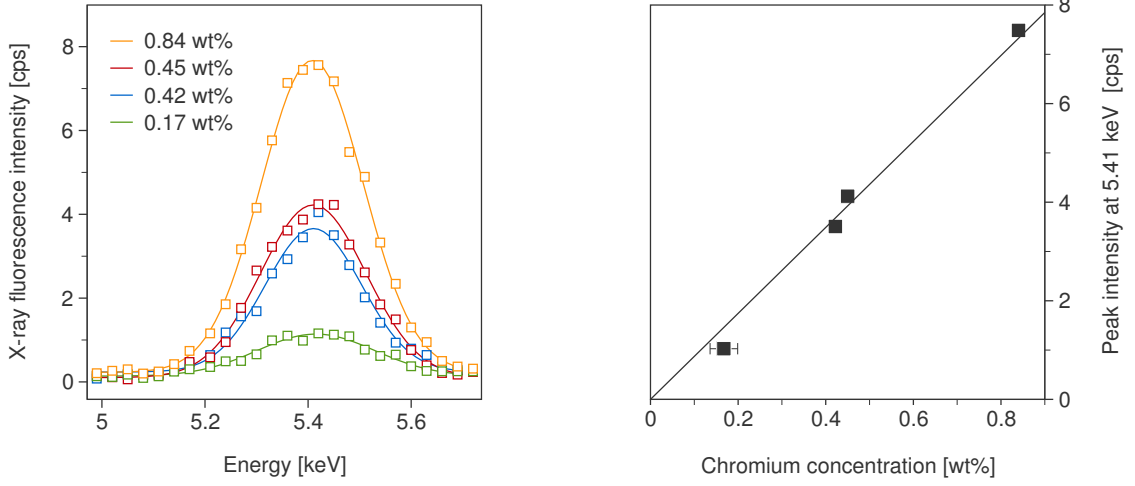


Figure 5.7: Chromium $K\alpha_1$ fluorescence for different chromium concentrations measured by ICP OES (left) and derived calibration curve (right).

5.3 Chromium distribution coefficient and macrosegregation

In case of an effective distribution coefficient k independent of solute concentration, the distribution of solute in the grown crystal, $C_S(g)$, is described by the Scheil equation (3.25)

$$C_S(g) = k C_{L0}(1 - g)^{k-1}. \quad (5.4)$$

with C_{L0} denoting the solute concentration in the initial melt, and g the solidified fraction of the melt. The effective distribution coefficient can be obtained by fitting the Scheil distribution to experimental solute concentration profiles along the crystal axis. From Eq. 5.4 it becomes immediately clear that for small crystals, i.e. for small crystallized fractions $g \ll 1$, the distribution coefficient can also be calculated from

$$k = \frac{C_S}{C_{L0}}. \quad (5.5)$$

Here, solid concentration of an arbitrary point in the solid can be taken, since Eq. 5.4 also implies that for small g the solute is virtually homogeneously distributed

	SAP10-A	SAP10-B	SAP10-C	SAP10-D
p_{O_2} at 2054°C [bar]	2×10^{-6}	1.1×10^{-5}	5.7×10^{-3}	8.3×10^{-8}
C_{L0} [wt%]	0.55	0.54	0.55	0.53
C_{S} [wt%]	0.42	0.45	0.84	0.17
k	0.77	0.83	1.55	0.32

Table 5.2: Measured chromium concentrations in small ruby crystals of series A and distribution coefficients calculated using Eq. 5.5. Uncertainty in k is determined by the uncertainty of the ICP OES measurement that is below 2.5%.

in the solid. Tab. 5.2 compiles liquid and solid chromium concentrations in the grown ruby crystals of series A. The values for the effective distribution coefficient were calculated according to Eq. 5.5. These data are plotted as dark boxes in Fig. 5.10. Uncertainty in k is smaller than the symbols.

The measured chromium distribution in the regular size crystals (series C) along with distribution profiles according to Eq. (5.4) for values of k giving the best fit to the data points (solid lines) are shown in Fig. 5.8. For crystals grown at intermediate (3.3×10^{-5} bar) and high (1.1×10^{-2} bar) oxygen fugacities, chromium distribution complies with the model, and the effective distribution coefficients obtained appear reliable. The experimental values for k are somewhat higher than expected from the theoretical dependence of k on p_{O_2} . Most likely, the actual oxygen fugacity during growth is slightly higher than resulting from the atmosphere composition, due to residual oxygen and/or moisture in the growth chamber, and higher oxygen fugacity favors the formation of the preferably incorporated Cr_2O_3 .

The crystal grown in low oxygen fugacity (2×10^{-6} bar) shows an unexpected chromium distribution. The calculated distribution coefficient is $k \approx 0.76 < 1$. Consequently the chromium content should increase monotonously with the solidified fraction of the melt. The measured chromium concentration, however, decreases slightly in the first-grown part of the crystal, and rises abruptly during further growth ($g > 0.4$). The turning point coincides with the onset of instability of the growth interface, i.e. the back-melting of the originally convex to partially flat interface, entailing inclusions and voids, and will not be considered in here.

Diminution of the chromium content in the first-grown part is probably caused by evaporation of chromium from the melt that becomes significant at low oxygen fugacity. Fig. 5.9 shows calculated vapor pressures of the most volatile chromium and aluminum species in dependence on p_{O_2} at the working temperature of 2054°C. At low oxygen fugacity ($p_{\text{O}_2} \lesssim 10^{-5}$ bar), the high vapor pressure of chromium metal contributes to the evaporation of chromium from the melt. Compared with chromium, the vapor pressures of the analogue aluminum species are nearly two orders of magnitude lower and can be neglected.

For this particular crystal the chromium distribution coefficient was calculated as the ratio of chromium concentration in the first-grown part of the crystal where impact of evaporation is least. The dashed red line in Fig. 5.8 shows the expected chromium profile for an effective distribution coefficient $k = 0.78$ calculated according to Eq. 5.5.

Fig. 5.10 compares chromium distribution coefficients obtained experimentally with those calculated from the ternary phase diagram. Dark boxes represent values calculated from the measured chromium content of the first-grown part of the crystal according to Eq. 5.5. Data stemming from fitting measured axial chromium distributions with the Scheil equation (Eq. 5.4) are indicated by gray boxes. The agreement with the calculated values is excellent for lower oxygen fugacity and $k < 1$. Obviously bending of the calculated $k(p_{\text{O}_2})$ curve is responsible for the deviation at higher oxygen fugacity. Agreement would improve significantly if the nearly linear dependence of k on $\log p_{\text{O}_2}$ was extrapolated from the low to the high p_{O_2} side of the graph (dashed line in Fig. 5.10).

5.4 Growth rate dependence of the effective distribution coefficient

It was explicated (Sect. 3.4.4) that the effective distribution coefficient of a dopant, here chromium, critically depends on growth velocity f . Quantitative description of different models include transport properties of the melt like viscosity ν and the diffusion coefficient D . Some of these quantities are hardly accessible by direct measurements either owing to challenging thermal conditions, i.e. the high melting

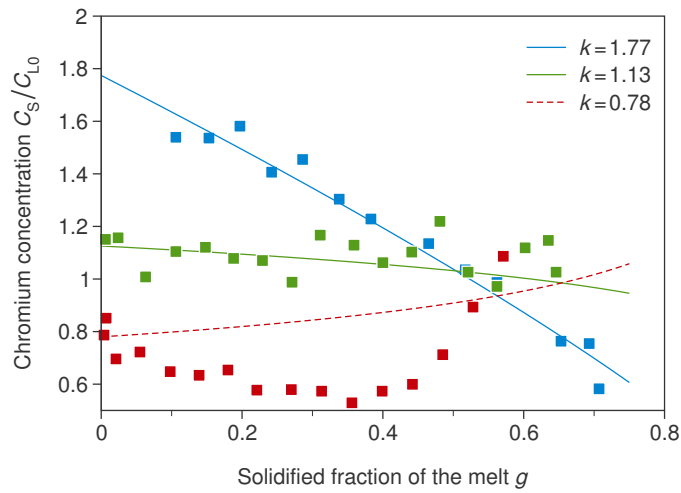


Figure 5.8: Axial chromium distribution in ruby crystals grown in different atmospheres.

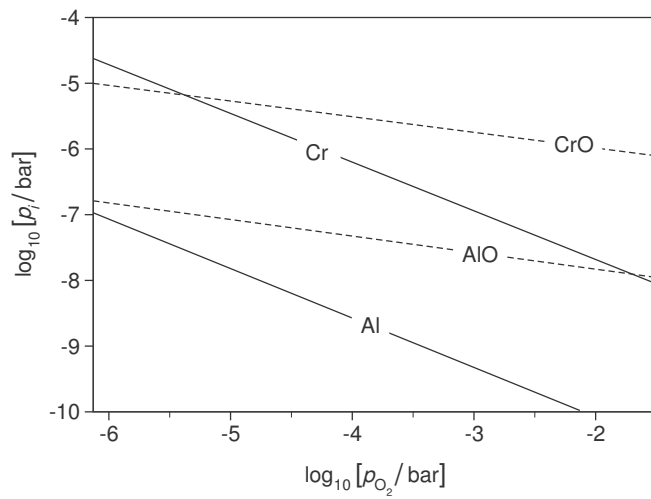


Figure 5.9: Calculated vapor pressure p_i of the most volatile chromium and aluminum species at 2054°C in dependence on oxygen fugacity p_{O_2} .

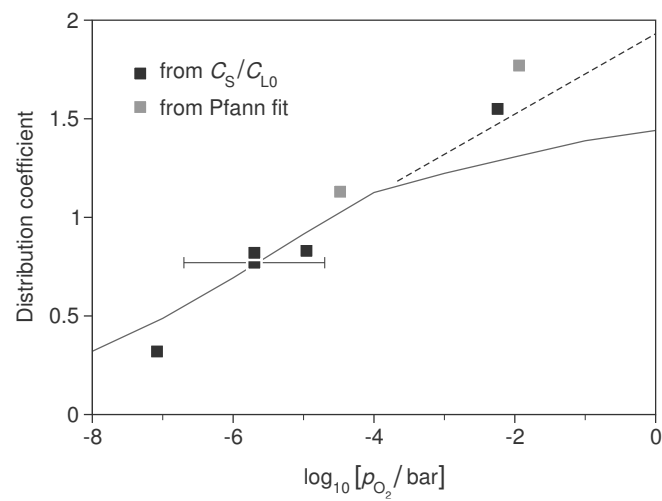


Figure 5.10: Comparison of the experimentally obtained (effective) chromium distribution coefficients for different oxygen fugacities with the values calculated from the ternary phase diagram (solid curve). Dark boxes refer to values calculated from the composition of the first-grown parts only according to Eq. 5.5, light boxes to values from Scheil fits (Eq. 5.4) to the measured axial chromium distribution. The error bar is a rough estimate for the case where p_{O_2} is fixed by residual oxygen content of the process gas. For all other experiments the error is significantly lower.

temperature of Al_2O_3 , or due to the conventional character of their definition, e.g. the diffusion boundary layer thickness δ . Goal of the growth experiment in series B was to experimentally determine the quantitative relation between the applied pulling speed and the effective distribution coefficient for a fixed growth atmosphere.

Fig. 5.11 shows chromium distribution along the growth axis in a crystal grown with piecewise different pulling rate, measured by X-ray fluorescence analysis. The mass of each segment was about 4 g, corresponding to solidified fraction of the melt of $g < 4\%$. For such small fractions and an effective distribution coefficient in the range $k = 1.1 \dots 1.5$, chromium concentration in the melt and in the crystal should change by not more than 2 or 3 per cent as reflected by the slight decrease of chromium concentration along each segment (Fig. 5.11). In the segment grown with lowest pulling rate (segment III), the decrease is larger than expected. With the same approximate length like all other segments, duration of this segment was significantly longer and, probably, evaporation of chromium oxide from the melt contributed to the concentration decrease to a larger degree.

For each segment i , incorporated chromium concentrations at the beginning and at the end of the segment, $C_{\text{SA}}(i)$ and $C_{\text{SB}}(i)$, were extrapolated from the linear fit through the measured chromium distribution. For the first segment, chromium concentration in the liquid, $C_{\text{LA}}(\text{I})$, was known from the starting melt composition. At the beginning of each subsequent segment C_{LA} was obtained from the concentration in the liquid at the end of the preceding segment, $C_{\text{LA}}(i) = C_{\text{LB}}(i-1)$. The effective distribution coefficient was calculated from the measured chromium concentration in the crystal at the beginning of each segment, $k(i) = C_{\text{SA}}(i)/C_{\text{LA}}(i)$, and used to calculate the concentration in the liquid at the end of the segment, $C_{\text{LB}}(i) = C_{\text{SB}}(i)/k(i)$. The values $k(i)$ obtained by this procedure are listed in Tab. 5.3.

The dependence of k on pulling rate is plotted in Fig. 5.12 along with the predicted curves according to the Ostrogorsky & Müller model (Eq. 3.21 in Sect. 3.4.4) using thermophysical data from Table 3.2 for $n = 1/2$ (dotted curve) and $n = 1/3$ (dashed curve). Neither calculated curve persuasively agrees with the experimental data points. Readily much better agreement can be obtained for n between $1/2$ and $1/3$. An intermediate value is also reasonable with respect to the Schmidt number of the Al_2O_3 melt, being $1 \ll Sc_{\text{Al}_2\text{O}_3} \approx 9400 \ll \infty$. Data fitting was done to obtain the

f [mm/h]	1.0	3.0	0.5	5.0
k	1.41 ± 0.04	1.29 ± 0.09	1.39 ± 0.26	1.14 ± 0.29

Table 5.3: Experimentally obtained values of the chromium effective distribution coefficient k for different pulling velocities f . The estimated experimental error increases with the number of the segment due to the iterative calculation procedure.

value of n giving best agreement with the experimental data yielding $n = 0.421$ (solid curve in Fig. 5.12).

According to the model of Burton, Prim, and Slichter (Sect. 3.4.4) dependence of the effective distribution coefficient on growth velocity in the BPS model is given by Eq. 3.18. This famous equation can be rewritten in a logarithmic fashion

$$\ln\left(1 - \frac{1}{k}\right) = \ln\left(1 - \frac{1}{k^*}\right) - \frac{\delta}{D} f. \quad (5.6)$$

Plotting measured (f, k) pairs yields a linear function with slope δ/D and ordinate axis intercept depending on the interface distribution coefficient (Fig. 5.13). From the linear fit to the data points the convecto-diffusive parameter is obtained.

$$\frac{\delta}{D} = (0.19 \pm 0.04) \text{ h/mm}$$

Calculating δ/D from BPS's approximation formula (Eq. 3.20) using thermophysical properties listed in Tab. 3.2 gives a somewhat lower value of ≈ 0.046 h/mm. Keszei et al. [84] found 0.2 h/mm for Nd and 0.09 h/mm for Cr during the Czochralski growth of $\text{Gd}_3\text{Ga}_5\text{O}_{12}$ (GGG). According to Eq. 3.20 these values must be corrected by a factor of $\sqrt{7}$ to account for the higher crystal rotation rate of 70 rpm. That gives slightly higher values, namely 0.53 h/mm for Nd and 0.24 h/mm for Cr, that are, however, still in satisfactory agreement with those obtained here.

From the regression constant the interface distribution coefficient for zero growth rate can be calculated.

$$k^*(f = 0) = 1.52 \pm 0.06$$

This value coincides with the value of the *effective* distribution coefficient k ob-

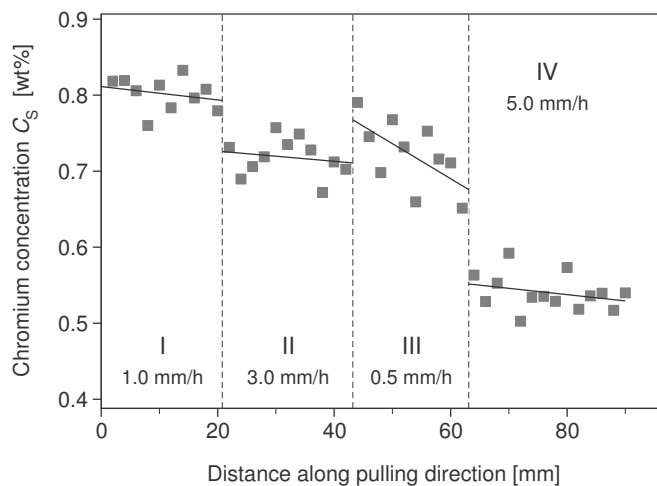


Figure 5.11: Chromium distribution along the pulling axis in a small diameter crystal grown with different pulling rates. For each segment, the actual profile was fitted with a linear function from which the distribution coefficient and the chromium concentration in the melt at the end of the segment was calculated.

tained from the crystal of series A grown in an identical atmosphere. As depicted in Fig. 3.6, growth velocity dependence of k is marginal for small velocities $\lesssim 1$ mm/h and both values should be expected to be similar $k \approx k^*$.

5.5 Deviation from steady growth – formation of growth bands

Fig. 5.14 shows the response of the growth system upon abrupt reduction of the heating power. In the figure, power and growth rate curves are time-related. Beginning of the curve displaying the crucible temperature was set manually. The original pyrometer readings (gray curve) were smoothed by calculating the running average over 20 values (solid black curve).

The absolute value of the measured crucible temperature measurement may be debatable; its rapid fall by about 5 K upon the heating power reduction, however,

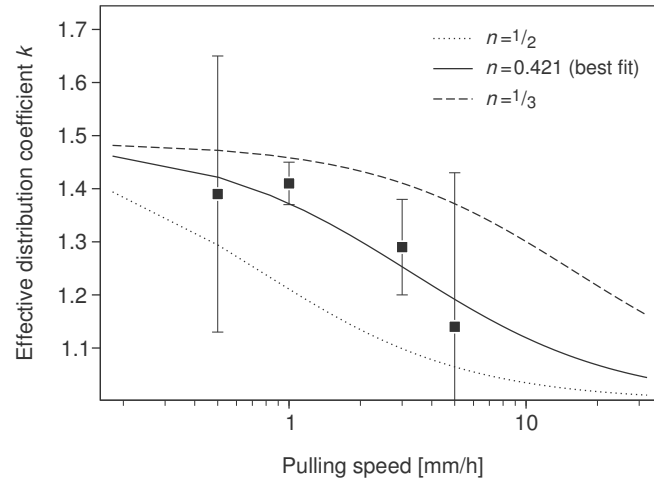


Figure 5.12: Experimentally obtained growth velocity dependence of the chromium effective distribution coefficient in ruby and data fitting according to the model of Ostrogorsky & Müller.

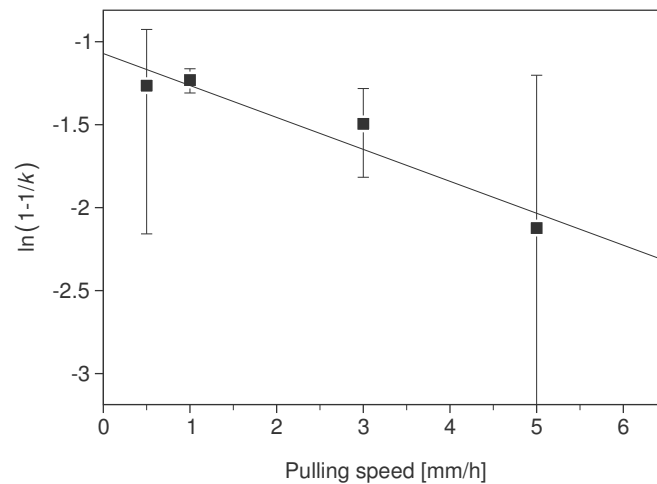


Figure 5.13: Growth velocity dependence of the chromium effective distribution coefficient in ruby. The solid line represents the linear fit through the experimental data points.

is obvious. The growth rate reacts nearly instantaneously reaching a maximum already after 5 minutes. The automatic diameter control efficiently compensates for the perturbation so that after 20...25 minutes the original state is restored. At its maximum the mass growth rate gains $R_{\max} > 10$ g/h, i.e. more than the fourfold of the original value. Since the diameter of the growing crystals changes only marginally, the observed increase of the mass growth rate must be mainly due to an increased velocity of the interface displacement.

The increased growth rate breaks the steady state characterized by the balance of solute fluxes at the interface (Eq. 3.17). The melt at the interface is further enriched (for $k^* < 1$), respectively depleted ($k^* > 1$), in chromium and a new steady state will be approached with steeper solute concentration gradient in the liquid. If growth rate falls back to its original value after a short time, then the original steady state will be restored. In the meantime more ($k^* < 1$) or less ($k^* > 1$) solute is incorporated into the growing crystal constituting a band of higher or lower chromium concentration evidenced by stronger or weaker coloration in Fig. 5.15. Fig. 5.16 shows the chromium concentration profiles $C_S(x)$ normal to the interface for the three crystals of series C grown in different atmospheres yielding different chromium distribution coefficients, measured by EPMA. Concentration scale is identical for all three curves and it is evident that the perturbation has only small impact for the crystal grown in an atmosphere yielding $k \approx 1$. All solid concentrations converge towards the respective concentration in the bulk liquid C_L which corresponds to an effective distribution coefficient tending to unity, $k \rightarrow 1$.

In the following, three different models of the effective distribution coefficient will be applied to estimate the deviation of chromium concentration in the bands from the steady state value quantitatively, i.e. the steady-state models by Burton, Prim, and Slichter (BPS) and Ostrogorsky & Müller introduced in Sect. 3.4.4 and an analytical model developed by Garandet for the description of microsegregation upon non-steady growth conditions [65]. Results from the previous section, i.e. the value of δ/D and the exponent n will be inserted in the analysis.

Chromium segregation during steady-state growth before the growth rate perturbation is characterized by a steady-state value of the effective distribution coefficient k that can be obtained from chromium concentration in the bulk liquid, C_L , and in the just grown piece of crystal, C_S . Since duration of the perturbation is small,

chromium concentration in the bulk liquid may be assumed to be invariable. This reasonable assumptions allows to calculate an effective distribution coefficient k' at maximum growth velocity from the measured maximum ($k < 1$) of minimum ($k > 1$) chromium concentration in the crystal C'_S

$$k' = \frac{C'_S}{C_L} = \frac{C'_S}{kC_S}. \quad (5.7)$$

Due to the convex shape of the growth interface (Fig. 5.15) the microscopic interface velocity V_i included in the segregation models is not identical with the vertical growth velocity V . From geometrical consideration follows that $V_i = V \cos(\alpha/2)$ with α being the interface angle that is 180° for a flat interface.

The Garandet model breaks with the stagnant film concept enunciated by Burton, Prim, and Slichter. Instead, it introduces an effective diffusive velocity $V_{\text{eff}}(t) = D/\delta(t)$ with $\delta(t)$ being the distance δ from the interface at which V_{eff} balances the overall fluid motion $V_i - W(z)$. $W(z)$ stands for the effective convection velocity at distance z ahead the interface. Assuming that W depends on time only via the $\delta(t)$ and that growth velocity is given by $V_i(t) = \bar{V}_i(1 + m(t))$ where m is a modulation around an average velocity \bar{V}_i such that back-melting is excluded ($m(t) > -1$ at any instant of time) the incorporated solute concentration becomes

$$C(t) = C_{\text{SS}} \left(\frac{(1 - k^*)\bar{\Delta}(1 - \bar{\Delta})}{1 - (1 - k^*)\bar{\Delta}} \cdot m(t) + 1 \right) \quad (5.8)$$

where C_{SS} is the solute concentration incorporated during steady state growth, and $\bar{\Delta}$ a convecto-diffusive parameter measuring the contributions of convection and diffusion to the mass transport $\bar{\Delta} = \bar{V}_i/V_{\text{eff}} = \bar{V}_i\bar{\delta}/D$. Here, $\bar{\delta}$ respectively $\bar{\delta}/D$ is the steady-state value determined in the previous section.

Tab. 5.4 compiles the estimated maximum (or minimum if $k > 1$) chromium concentrations in the bands generated by the short-term growth rate variation. Readily, all three models yield at least satisfactory agreement with the experiment with standard deviations below 0.03 wt%. The models explicitly assume that the change of growth velocity occurs so slowly that the system is able to follow. In case of faster changes the microscopic growth rate does not control the microsegregation in a manner adequately accounted for by neither the BPS nor Ostrogorsky & Müller model.

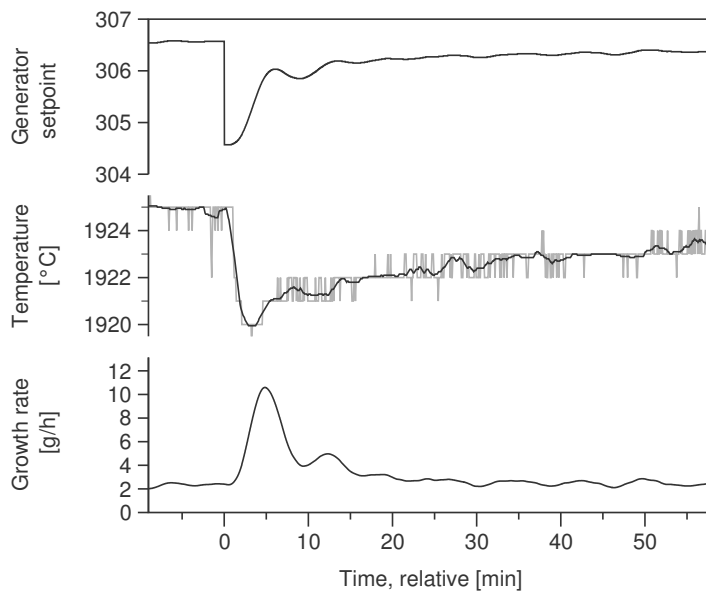


Figure 5.14: An abrupt reduction of the heating power (generator setpoint) by 2 units entails drop of the crucible temperature of approximately 5 K and an increase of crystal mass growth rate by a factor of 5. The temperature curve was manually shifted that the onset of the temperature drop occurs *after* the setpoint change and *before* the growth rate change.

It has been shown [56] that BPS regularly overestimates distribution variations. Garandet instead extended his perturbation approach and proposed a solution of the time-dependent mass transfer equation capable to describe solute segregation upon short-period growth rate fluctuations, e.g. those associated with crystal rotation or pulling device vibrations [65]. Both models require a good estimate for the convecto-diffusive parameter δ/D to yield quantitatively reliable results. The Ostrogorsky & Müller model yields a good approximation without assessing such parameter; the exponent in Eq. 3.22 can be estimated from the melt's Schmidt number.

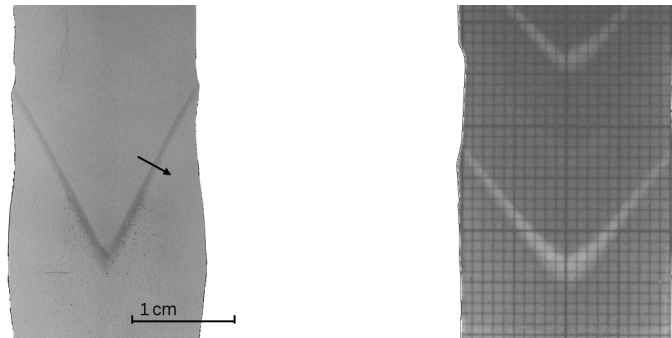


Figure 5.15: Photographs of both-sides polished longitudinal cuts through ruby crystals. The coloration stems from chromium, the higher the chromium contents the darker the image. The temporarily increased growth rate decorates the interface with a band of higher (for $k < 1$, left) respectively lower ($k > 1$, right) chromium concentration. The arrow in the left-hand figure indicates the approximate location of the EPMA line-scans.

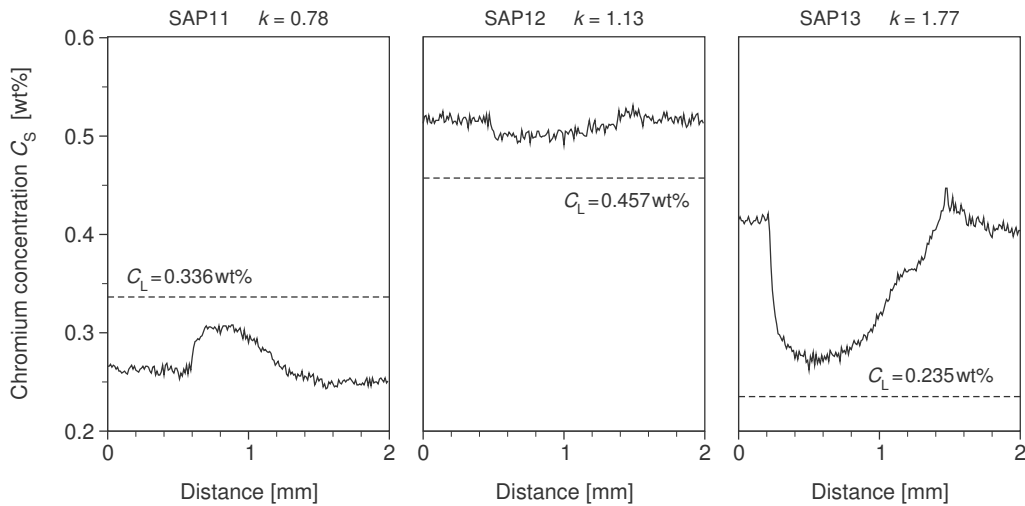


Figure 5.16: Chromium concentration C_S measured over the generated bands for different effective distribution coefficients. Dashed lines represent chromium concentration in the bulk melt, C_L , at the moment the band was formed.

	Burton, Prim, and Slichter	Ostrogorsky & Müller	Garandet	Measured
SAP11	0.291	0.286	0.296	0.308
SAP12	0.484	0.490	0.468	0.500
SAP13	0.308	0.326	0.233	0.272

Table 5.4: Chromium concentrations (in wt%) at maximum deviation from the steady state value estimated with different models of the effective distribution coefficient in comparison with the measured.

5.6 Conclusions

It was shown that chromium effective distribution coefficient in melt-grown ruby crystals depends on oxygen fugacity in the growth ambient via the activities of CrO and Cr₂O₃ species in the liquid. The latter is preferentially incorporated in the growing crystals with an interface distribution coefficient significantly larger than unity whereas there is no evidence that the divalent chromium species is incorporated at all. The effective distribution coefficient of chromium can be controlled by adjusting the fraction of chromium in trivalent state. From the phase diagram of the CrO–Cr₂O₃–Al₂O₃ system, the oxygen fugacity that causes chromium segregation to vanish, can be calculated as $p_{\text{O}_2} \approx 2.5 \times 10^{-5}$ bar. This value could be confirmed by growth experiments yielding ruby crystals with nearly homogeneous chromium (macro)distribution. When growing in such optimized ambient consisting of 5 vol% CO and 2.15 vol% CO₂ in argon the system is also immune to fluctuations of growth conditions affecting the effective distribution coefficient. Three models for the latter, (i) the classical stagnant film approach by Burton, Prim, and Slichter, (ii) the model by Ostrogorsky and Müller based on an integral boundary layer analysis, and (iii) a perturbation approach by Garandet, were found to quantitatively predict the magnitude of chromium deviation upon an artificially introduced growth rate variation.

6 Melt growth of zinc oxide

The wide direct band gap of 3.3 eV and large exciton binding energy of 60 meV make zinc oxide (ZnO) a promising material for optoelectronic applications. ZnO crystallizes in a distorted wurtzite structure; its piezoelectricity and dependence of electrical conductivity on ambient conditions can be exploited in sensor appliances. However, broad application of single crystalline ZnO is handicapped by the still insufficient p-type doping and the lack of cheap and high-grade substrates for the growth of epitaxial layers.

The triple point of ZnO is at 1975°C and 1.06 bar making it impossible to melt ZnO at ambient pressure. At melting temperature ZnO evaporates under dissociation into elements



resulting in an equilibrium oxygen partial pressure of 0.35 bar. These extreme conditions prevented successful melting experiments for a very long time: It's not surprising that crystal growers elaborated other growth methods, primarily growth from hydrothermal solution and from the vapor phase.

Helbig [73] denoted that pure physical vapor transport of ZnO would not gain sufficiently high growth rates except for hardly controllable (T, p) conditions. Most approaches are therefore based on the idea of using a chemical transport agent as previously described by Scharowsky [146]. Zinc is evaporated from a source stock of either metallic zinc (as in the work of Scharowsky) or zinc oxide in a stream of nitrogen with addition of hydrogen [73, 146, 97, 120, 69], chlorine or carbon [121], and transported to a second reaction chamber where ZnO deposition proceeds by oxidation at usually lower temperature. Recent works yielded 2-inch-diameter ZnO crystals of about 1 cm thickness grown within a week [97].

Aiming at higher growth rates, Wanklyn [177] used phosphate and vanadate fluxes

in the temperature range between 900 and 1300 °C and obtained cm-sized ZnO platelets of thickness below 0.5 mm. Nielsen and Dearborn [119] dissolved zinc oxide in molten PbF_2 contained in sealed crucibles and grew crystals of a few centimeters in their largest dimension. Fischer and Sinn [59] obtained millimeter-sized ZnO crystals from PbF_2/PbO fluxes. Taking up the work of Wanklyn, Chinese groups investigated numerous ternary systems in search of better solvents, among them phosphate systems, e.g. $\text{ZnO-P}_2\text{O}_5\text{-B}_2\text{O}_3$, $\text{ZnO-P}_2\text{O}_5\text{-MoO}_3$, $\text{ZnO-P}_2\text{O}_5\text{-K}_2\text{O}$ [80, 81, 75] and identified a few potentially suitable candidates. Unfortunately, no growth experiments were reported so far using these solvents.

The hydrothermal growth of zinc oxide exploits the chemical equilibria of ZnO with zinc hydroxide, Zn(OH)_2 , and zincate ions $[\text{Zn(OH)}_4]^{2-}$ that are soluble in alkaline aqueous solutions at hydrothermal conditions (several 100 bars total pressure and several 100 °C). As for the growth via chemical vapor transport, temperature dependence of the underlying equilibria is used to transport species from a feed-stock (usually at higher temperature) to the growth region where the solution is supersaturated thus giving the driving force for growth. First literature reports on hydrothermal growth of zinc oxide reach back the early 1950s [174]. In his paper on the hydrothermal growth of quartz, Walker also made a short note on chances of growing other materials using this technique and mentioned successful growth of small ZnO crystals. Hydrothermal growth of ZnO was elaborated at Bell Labs in the early 1960s [92, 93]. Laudise et al. pointed out important factors to achieve good growth, i.e. base concentration, temperature difference between feed and growth zone, presaturation to avoid dissolution of seeds, improved warm-up procedure, addition of Li^+ to the solution to suppress dendrite formation, etching of seeds to remove defects generated during mechanical treatment, thermal pretreatment of the nutrient to control particle size. Recent developments led to growth technology capable to produce large ZnO crystals of dimensions exceeding 2 inches [124]. In meter-sized autoclaves more than 100 crystals with masses of a few hundred grams each can be grown simultaneously at temperatures between 300 °C and 430 °C and pressures between 700 and 2500 bar [54].

First melting of zinc oxide was observed by Fritsch [61]. Trying to grow crystals via solid state reaction, he heated ZnO sintered ceramic cylinders by electric current until the material started to evaporate extensively. When heating-up was done very

fast, he observed isolated melting channels which he explained by local exceeding the melting temperature of 1975°C . Burmeister [33] melted ZnO by inductively heating ceramic rings with a 12 kW generator working at 1 MHz. He obtained small crystals of brown color that was changed to pale yellow after annealing in oxygen. Probably knowing Burmeister's experiments, Nause designed a process for growing ZnO single crystals from the melt contained in a cold crucible [116, 115]. Large chunks of pressed and sintered ZnO are placed in the center of a water-cooled induction coil driven by a radio frequency generator. Heated up by eddy currents the material in the center of the batch melts while that near the coil remains solid thus forming a melt container, the so-called cold crucible or skull. Addition of small pieces of metallic zinc may be gainful to initiate efficient heating at low temperature implying low conductivity of the ZnO powder. After melting, when the heating power is reduced the material cools down slowly, and crystals start to form inside the batch. The apparatus constructed by Cermet can be operated at pressures up to 100 atm [115] which prevents evaporation of volatile components. Additionally, it allows to dip the melt from top with a seed crystal to perform pulling like in a Czochralski arrangement. This option, however, seems not to be used in practice. The great advantage of the cold crucible technique is that there is no crucible of foreign material needed. The benefits for designing a crystal growth process are obvious since (i) a crucible material that can withstand very high temperatures *and* chemically aggressive melt *and* oxidizing atmosphere is hard to find, and (ii) contamination of melt and growing crystals by impurities stemming from crucible production process or the crucible itself are excluded. The main drawback of the technique arrives from the way of heating. As the conductivity of ZnO increases with temperature and must be expected to soar upon melting, parts of the batch that are already hottest are heated most. This leads to unusually steep temperature gradients in the material which are disadvantageous for crystal quality because they introduce colossal thermal stress. As a result, the size of individual crystals grown is rather limited. Against these odds, Nause claimed that crystals up to 2 inch can be grown from batches larger than 5 inch. Interestingly, using this technique Nause et al. were able to melt AlN [115].

6.1 Zn–O and Ir–O predominance diagrams

Fig. 6.1 shows the calculated stability fields of Ir/IrO₂ and Zn/ZnO. At low temperature and high oxygen fugacity (north-west corner of the diagram) both oxides are stable. In the opposite south-east corner of the diagram, i.e. at high temperature and low oxygen fugacity, ZnO dissociates according to Eq. 6.1. None of these two regions is usable for crystal growth since either Ir metal is not stable or Zn metal emerges increasing the risk of alloying and finally destroying the Ir crucible drastically. Fig. 6.1 shows that at melting temperature of ZnO, solid and liquid ZnO is in equilibrium with iridium metal for $-5.431 \leq \log [p_{\text{O}_2}/\text{bar}] \leq 1.831$. Along this melting isotherm of ZnO, zinc fugacity p_{Zn} drops from 214 bar at the triple point with liquid zinc (point B) to 0.051 bar at the upper limit of the Ir stability field (point A). The line between points A and B marks the oxygen fugacity range where melt growth of ZnO from Ir crucibles is possible. With respect to the high zinc fugacity – from Eq. 6.1 follows that p_{Zn} increases by an order of magnitude if p_{O_2} is lowered by two orders of magnitude – the high oxygen fugacity side near point A should be preferred. The figure also shows that it is impossible to find a mixture of O₂ with an inert gas that is able to keep both, ZnO and Ir chemically stable for the whole crystal growth process. At temperatures approaching the melting temperature of ZnO, pure Ar gas yields an oxygen fugacity resulting mainly from residual impurities that would force dissociation of ZnO. On the other hand, mixtures containing large amounts of O₂ would easily oxidize constructive parts made of Ir that are at moderate temperatures in the range between 1000 and 1500°C. Thanks to thermal decomposition according to Eq. 2.6 carbon dioxide yields an oxygen fugacity that is well inside the desired range (green dashed curve in Fig. 6.1 calculated for a total pressure of 10 bar).

6.2 Bridgman growth of ZnO

ZnO crystals were grown by the Bridgman method from the melt contained in an iridium crucible. The crucible was surrounded by zirconia and alumina insulating ceramics and heated inductively. An oriented seed was attached to the small channel at the end of the conical bottom of the crucible to initiate growth in the desired

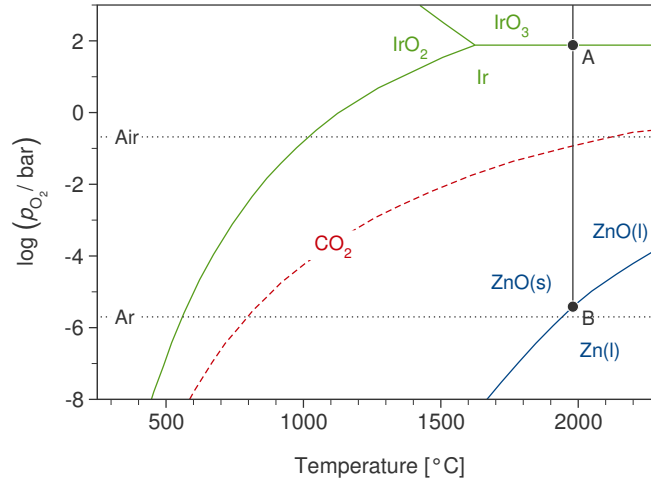


Figure 6.1: Calculated stability fields of Ir/IrO₂ and Zn/ZnO. The green dashed line represents oxygen fugacity of CO₂ at 10 bar.

direction. Approximate temperature of this part of the crucible was monitored by a Ir/IrRh thermocouple fixed at a distance of a few millimeters below the tip. Growth was carried out in an water-cooled steel chamber filled with CO₂ to a pressure of 20 bar.

In contrast to Bridgman configurations involving resistive heating, in the inductively heated variant described here the crucible itself acts as the heating element. When the crucible is translated in axial direction of the induction coil, distribution of the electromagnetic field in the crucible changes and with that the spatial distribution of heat input. As a result temperature gradients in melt and crystal strongly depend on the crucible position. Moreover, the actual growth velocity, i.e. the displacement velocity of the interface, may significantly vary from the imposed mechanical translation velocity. Therefore instead of moving the crucible the entire arrangement was slowly cooled down by lowering the heating power, thus moving the thermal gradient through the stationary crucible.

A typical temperature program for growing ZnO is shown in Fig. 6.2. Here, the temperature measured by the thermocouple near the seed channel versus time is drawn. After heating up, the power was further increased until melting indicated by

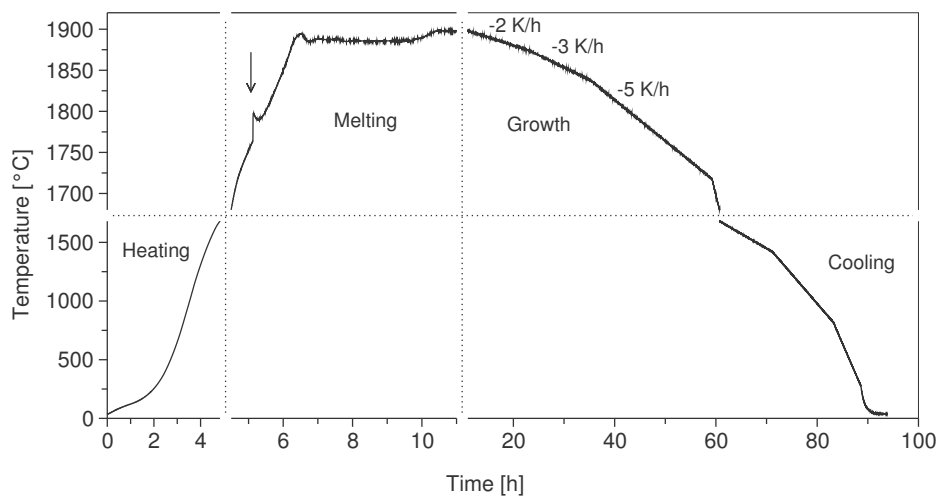


Figure 6.2: Temperature program for ZnO growth.

a small peak (arrow in Fig. 6.2) was observed. The increase in signal was probably caused by the suddenly improved thermal contact between melt and the conical crucible bottom. After keeping the melt somewhat above the assumed melting temperature for homogenization, the heating power was slowly reduced and thus the crucible temperature decreased at a rate of typically a few degrees per hour. In the experiment shown in the figure the cooling rate was increased stepwise from -2 to -5 K/h. After the expected end of growth, the crucible was cooled to room temperature within one day.

After growth, the solidified melt formed a solid bulk tightly sticking to the crucible so that core drilling was necessary to retrieve the crystal. The as-grown crystals were of orange to dark brown color, approximately 1.5 inch in diameter and up to a few centimeters long. Growth experiments without seed resulted in polycrystals and there was no preferential orientation for the individual grains. Only slight enlargement of some grains could be observed with increasing crystal length. But even if seeding was successful, most ingots showed more than one crystal orientation. Usually, the grain of the seed orientation covered more than two third of the cross-sectional area. Contact between crucible and melt caused spontaneous nucleation and appearance of parasitic grains of different orientation. Most successful was

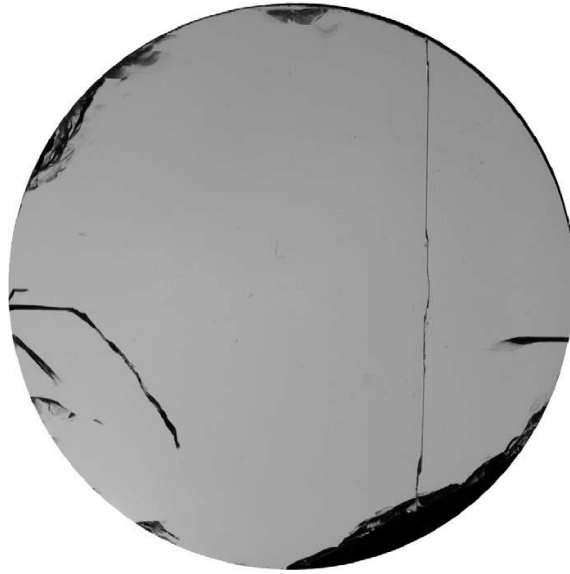


Figure 6.3: Optical micrograph of an ZnO $\{11\bar{2}0\}$ wafer between crossed polarizers. Bended black lines are cracks. The diameter of the sample is 1.5 inch.

growth on seeds along $[10\bar{1}0]$ (x direction) yielding wafers showing almost homogeneous extinction when viewed between crossed polarizers (Fig. 6.3). But also the best crystals contained cracks which most probably were caused by thermal stress.

Relating the crystallization duration from the process data (temperature, power) to length of the obtained crystals gives a estimate of the mean growth rate to be of the order of 1 mm/h. Since impurity striations could not be found in the grown crystals, a precise determination of the growth rate was not possible.

Crystalline perfection was verified by X-ray rocking curve measurements at different positions of a mechanically polished wafer. For the 0002 reflection full-width at half-maximum values (FWHM) between 22 and 47 arcsec were found (Fig. 6.4). Different peak positions result from wafer bending emerging during the preparation procedure. The FWHM values are of the order of those reported for ZnO grown by the hydrothermal method [124] indicating similar crystalline perfection.

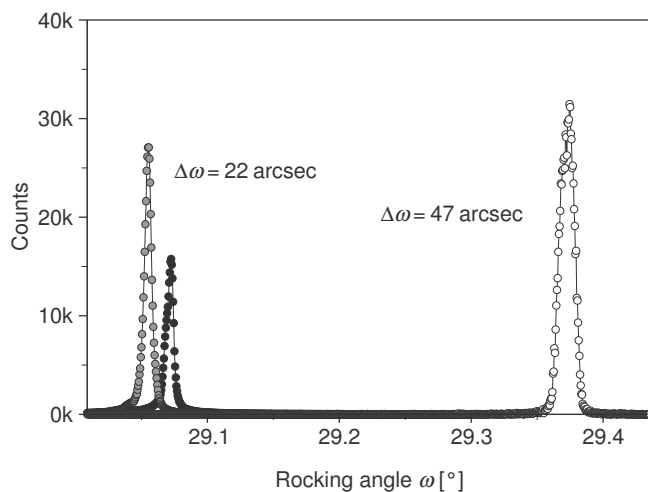


Figure 6.4: X-ray rocking curves of the 0002 reflection at three different positions on a mechanically polished $\{11\bar{2}0\}$ wafer.

6.3 Alloying with Mg

Modulation of band gap and/or lattice parameter is an essential issue for constructing various electronic and optical devices using compound semiconductors. For $\text{Zn}_{1-x}\text{Mg}_x\text{O}$ solid solutions the band gap increases linearly with Mg concentration from 3.3 eV to about 4.0 eV at $x = 0.33$ measured on films grown by pulsed laser deposition on sapphire targets [125]. At higher Mg concentrations the grown films contained MgO as an impurity phase that arises from exceeding the solid solubility. Since the end members ZnO (“zincite”) and MgO (“periclase”) are not isostructural their mutual miscibility must be limited. On the periclase side, solid solutions were found down to $x \approx 0.62$ [186]. Under hydrothermal conditions (650 °C, 1...1.5 kbar) Wang et al. obtained solid solutions with Mg concentrations up to $x = 0.055$ [175]. On the basis of lattice parameter measurements on $\text{Zn}_{1-x}\text{Mg}_x\text{O}$ samples prepared by solid state reaction, Segnit & Holland constructed a phase diagram of the MgO–ZnO system constituting a simple eutectic system with broad solid solution range on the MgO side, a wide miscibility gap, and tiny solid solution range on the ZnO side [152]. However, the authors state that no melting was observed up to the maximum temperature of 1750 °C even in the vicinity of the expected eutectic com-

position. Therefore all features of this phase diagram above this temperature, in particular the drawn *liquidus* lines, must be regarded tentative and treated with caution.

To investigate incorporation of Mg into ZnO during melt solidification, three different initial $\text{Zn}_{1-x}\text{Mg}_x\text{O}$ compositions, $x_0 = 0.01, 0.02,$ and $0.03,$ were used in Bridgman growth experiments. ZnO and MgO powders were mixed in the appropriate ratios, pressed in a cold isostatic press at about 2000 bar, and annealed at 1000°C for 1 day. The procedure yielded dense cylindrical blanks approaching about 95% of the theoretical density. These blanks were used as starting material for crystal growth following the procedure described above. Single crystals of the solid solution with up to 35 mm length and a diameter of 33 mm were obtained. For $x_0 = 0.03$ the obtained boule was polycrystalline; for the other compositions the appearance was similar to that of pure ZnO.

The amount of Mg in the grown crystals was determined with ICP OES. Samples from different axial positions corresponding to different solidified mass fractions of the melt were dissolved in hydrochloric acid at room temperature. The ICP OES spectrometer was calibrated with synthetic standard solutions.

Fig. 6.5 shows the measured normalized Mg concentration x_S/x_0 in dependence on the solidified mass fraction of the melt. Obviously, Mg concentration is higher than in the initial melt (x_0) in the first-grown part of the crystal but drops with advancing growth. From such concentration profile follows that Mg is preferentially incorporated, i.e. the Mg distribution coefficient is greater than unity, $k_{\text{Mg}} > 1.$ This conclusion is in opposition to the proposed phase diagram of the MgO–ZnO system [152]. To get a credible numerical value of $k_{\text{Mg}},$ all data points for the three crystals with $x_0 = 0.01, 0.02,$ and 0.03 were gathered into a single data set. This can be done as long as the distribution coefficient does not depend on composition. At least for the limited range regarded here this assumption seems to be well fulfilled. Data fitting yields a value of $k_{\text{Mg}} = 1.34.$ The corresponding idealized Mg profile is represented by the solid curve in Fig. 6.5.

The experimentally observed Mg distribution coefficient cannot be explained assuming a simple eutectic system MgO–ZnO. Hence, the previously published phase diagram cannot be true. Without further investigation Schulz et al. [150] proposed a phase diagram that is in accordance with the assured experimental evidence com-

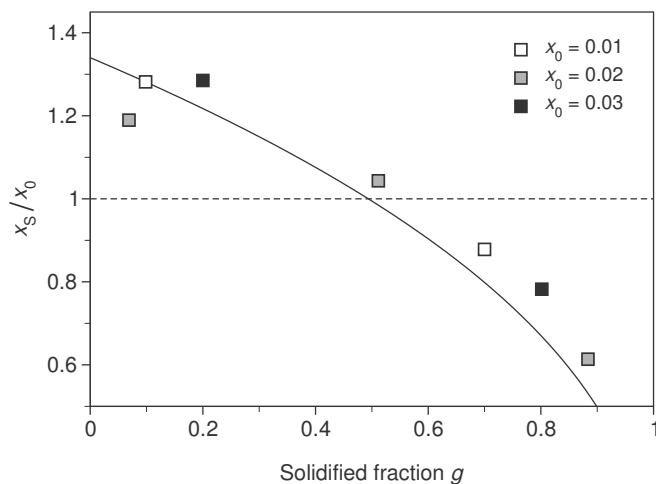
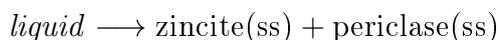


Figure 6.5: Normalized Mg distribution in $\text{Zn}_{1-x}\text{Mg}_x\text{O}$ solid solution crystals.

prising a peritectic reaction



at 2020°C . Assuming ideal behavior for the liquid phase and for zincite solid solutions a *solidus* can be calculated that corresponds to a maximum solubility of Mg in zincite of $x = 0.07$ and a equilibrium distribution coefficient $k_{\text{Mg}} \approx 1.75$ that is of the same order as the experimentally determined effective distribution coefficient.

6.4 Conclusions

Zinc oxide (ZnO) single crystals have been grown from the melt at elevated pressure. Contrary to what had been believed so previously, a ZnO melt could be held in an (inductively heated) iridium crucible. The key is the use of a CO_2 atmosphere that is practically inert at lower temperature but yields a significant oxygen fugacity at high temperature capable to suppress decomposition of ZnO. Crystalline perfection of the grown crystals was comparable to that reported for hydrothermally grown material. The main disadvantage of the latter is probably the unwanted incorporation of

mineralizers and OH^- ions absent in melt growth processes. Compared to growth methods employing crystallization from the gas phase, melt growth comprises higher growth rates and expectable crystals sizes. Main issue of the Bridgman growth of ZnO is thermo-mechanical stress in the crystals growing in intimate contact with the crucible, sensitivity of the thermal field to the crucible position in the induction coil, and control of actual growth rate. Mg-doping was achieved within the range of solubility. Contrary to the published phase diagram of the MgO–ZnO system the distribution coefficient of Mg was found to be larger than unity, $k_{\text{Mg}} \approx 1.3$. A tentative phase diagram involves peritectic melting of zinc-rich $\text{Zn}_{1-x}\text{Mg}_x\text{O}$ solid solutions.

7 Summary

Oxygen fugacity of the growth ambient is a thermochemical parameter with great impact on the outcome of oxide crystal growth experiments. A typical melt growth process involves a large number of different components including the melt and crystal to be grown, the crucible and other heating items, thermal insulation and various constructive parts. The variety of different materials employed simultaneously and the large temperature range passed in a typical process impose severe constraints to the growth atmosphere to be really inert. Oxygen fugacity must be confined to a sometimes narrow, temperature-dependent range in order to avoid unwanted oxidation and/or reduction. Chemical thermodynamics provides a set of easy to use relations that can be utilized to calculate the stability fields of different phases. The necessary thermochemical data of the involved phases can be found in textbooks, relevant data compilations, or electronic databases. These results can be arranged in form of predominance diagrams that allow to select a suitable ambient composition.

In this work, single crystals of three different oxides, namely iron(II) oxide, aluminum oxide doped with chromium, and zinc oxide, were grown from the melt using growth techniques that appeared best suited for that purpose. In all instances, stability fields of involved oxides prone to oxidation or reduction were calculated and growth atmosphere chosen to yield an oxygen fugacity fitting the stability fields over a wide temperature range.

Wüstite single crystals of near-eutectoid composition ($\text{Fe}_{0.944}\text{O}$) were successfully grown using the micro-pulling-down technique in an atmosphere composed of 5 vol% CO , 10 vol% CO_2 , and 85 vol% Ar . Thermoanalytical measurements verified that such ambient stabilizes iron in the Fe^{2+} valence state in which it occurs in FeO . At sufficiently high pulling rate of 50 mm/min entailing a high cooling rate, eutectoid decomposition was successfully hindered so that those crystals were free of magnetite precipitates. X-ray diffraction analysis of crystals grown at lower pulling

speed disclosed the presence of *two* wüstite phases. One of those was nearly stoichiometric (approximately $\text{Fe}_{0.981}\text{O}$), the other more iron-deficient than the single phase wüstite grown under identical conditions but higher pulling rate ($\text{Fe}_{0.909}\text{O}$). Appearance of two distinct wüstite phases supports the model of spinodal type decomposition of wüstite.

Ruby single crystals were grown in different atmospheres yielding different oxygen fugacities at melting temperature using the Czochralski technique. From simulation of the $\text{Al}_2\text{O}_3\text{-Cr}_2\text{O}_3\text{-CrO}$ ternary system it was predicted that the chromium distribution coefficient increases with increasing oxygen fugacity. Analysis of the grown crystals confirmed the relation also quantitatively with satisfactory accuracy. At low oxygen fugacity, $p_{\text{O}_2} < 10^{-7}$ bar, chromium is barely incorporated into the growing crystal due to a significant amount of CrO in the melt. In such reducing conditions the effective distribution coefficient is much less than unity, $k \approx 0.3$. With increasing oxygen fugacity the amount of CrO lessens and the effective distribution coefficient exceeds unity, $k \approx 1.5$ for $p_{\text{O}_2} \approx 5 \times 10^{-3}$ bar. With regard to an intended high dopant homogeneity the oxygen fugacity at which chromium segregation vanishes and k becomes unity is of great interest. From the calculated dependence $k(p_{\text{O}_2})$ a value of $p_{\text{O}_2} \approx 2.5 \times 10^{-5}$ bar can be estimated. The experimentally obtained effective distribution coefficient for an only slightly higher oxygen fugacity ($p_{\text{O}_2} \approx 3.3 \times 10^{-5}$ bar) was $k \approx 1.1$ and the crystal grown in such ambient was distinguished by an extraordinarily homogeneous chromium macro and micro distribution.

For long time, melt growth of zinc oxide, ZnO, single crystals by well established techniques was believed to be impossible due to the lack of a suitable container material that could thermally and chemically withstand the aggressive conditions at the melting point. Thermodynamic calculations and growth experiments using directional solidification in a cylindrically shaped crucible (Bridgman configuration) disproved this conjecture. The key to successful melting and solidification of ZnO was the use of a combination of an inductively heated iridium crucible with a CO_2 atmosphere at 10...20 bar. At temperatures below approximately 1500°C oxygen fugacity of CO_2 is negligible so that oxidation of iridium is practically averted. Thermal decomposition of CO_2 at high temperatures approaching 2000°C yields an oxygen fugacity large enough to greatly suppress the decomposition of ZnO. The

growth experiments gave crystals of 33 mm diameter with crystalline perfection comparable to that of hydrothermally grown material. However, cracking was frequently observed due to thermo-mechanical stress resulting from the intimate contact between crucible and crystal. The crystals could be doped with Mg within the limits of solid solubility. From the observed Mg distribution follows that contrary to the published phase diagram the system ZnO–MgO cannot be a simple eutectic system.

Bibliography

- [1] ACerS-NIST Phase equilibria diagrams, CD-Rom database version 3.0.1, 2004.
- [2] N. V. ABROSIMOV, Mosaic and gradient SiGe single crystals for gamma ray Laue lenses, *Exp. Astronomy* **20** (2005), 185–194.
- [3] I. ADAMS, J. W. NIELSEN, and M. S. STORY, Growth of broad linewidth ruby crystals, *J. Appl. Phys.* **37** (1966), 832–836.
- [4] J. A. ADAMSKI, R. C. POWELL, and J. L. SAMPSON, Growth of uncommon Verneuil crystals and their characterization by light scattering, *J. Crystal Growth* **3–4** (1968), 246–249.
- [5] B. ANDERSSON and J. O. SLETNES, Decomposition and ordering in Fe_{1-x}O , *Acta Cryst. A* **33** (1977), 268–276.
- [6] J. O. ANDERSSON, T. HELANDER, L. HÖGLUND, P. F. SHI, and B. SUNDMANN, Thermo-Calc and DICTRA, Computational tools for materials science., *Calphad* **26** (2002), 273–312.
- [7] Y. ANZAI, S. KIMURA, T. SAWADA, T. RUDOLPH, and K. SHIGEMATSU, Measurement of density, viscosity and surface tension of molten lithium niobate, *J. Crystal Growth* **134** (1993), 227–234.
- [8] P. W. ATKINS, *Physikalische Chemie*, VCH, 1990.
- [9] G. I. BABKIN, E. A. BRENER, and V. A. TATARCHENKO, Crystallization stability during capillary shaping: II. Capillary stability for arbitrary small perturbations, *J. Crystal Growth* **50** (1980), 45–50.

- [10] C. W. BALE and E. BÉLISLE, Fact-Web suite of interactive programs, 2014, www.factsage.com.
- [11] C. W. BALE, E. BÉLISLE, P. CHARTRAND, S. A. DECTEROV, G. ERIKSSON, K. HACK, I. H. JUNG, Y. KANG, J. MELANÇON, A. D. PELTON, C. ROBÉLIN, and S. PETERSEN, FactSage thermochemical software and databases - recent developments, *Calphad* **33** (2009), 295–311.
- [12] S. BALINT, S. EPURE, T. DUFFAR, and L. BRAESCU, Dewetted Bridgman crystal growth: Practical stability over a bounded time period in a forced regime, *J. Eng. Math.* **75** (2012), 191–208.
- [13] I. BARIN, *Thermochemical data of pure substances*, Wiley-VCH, Weinheim, 1995.
- [14] J. BAUD, A. FERRIER, and J. MANENC, Study of magnetite film formation at metal-scale interface during cooling of steel products, *Oxidation of Metals* **10** (1978), 331–342.
- [15] M. BERKOWSKI, K. ILIEV, V. NIKOLOV, P. PESHEV, and W. PIEKARCZYK, Conditions of maintenance of a flat crystal/melt interface during Czochralski growth of bismuth germanium oxide single crystals, *J. Crystal Growth* **108** (1991), 225–232.
- [16] V. BERMÚDEZ, M. D. SERRANO, and E. DIÉGUEZ, Bulk periodic poled lithium niobate crystals doped with Er and Yb, *J. Crystal Growth* **2000** (1999), 185–190.
- [17] J. BERTHON, A. REVCOLEVSCHI, H. MORIKAWA, and B. TOUZELIN, Growth of wustite (Fe_{1-x}O) crystals of various stoichiometries, *J. Crystal Growth* **47** (1979), 736–738.
- [18] R. BERTRAM and D. KLIMM, Assay measurements of oxide materials by thermogravimetry and ICP-OES, *Thermochimica Acta* **419** (2004), 189–193.
- [19] N. BIRKS, G. H. MEIER, and F. S. PETTIT, *High Temperature Oxidation of Metals*, 2nd ed., Cambridge University Press, 2006.

-
- [20] H. K. BOWEN and W. D. KINGERY, Growth of wustite (FeO) single crystals by chemical vapor deposition, *J. Crystal Growth* **21** (1974), 69–73.
- [21] C. D. BRANDLE, Simulation of fluid flow in $\text{Gd}_3\text{Ga}_5\text{O}_{12}$ melts, *J. Crystal Growth* **42** (1977), 400–404.
- [22] C. D. BRANDLE, V. J. FRATELLO, A. J. VALENTINO, and S. E. STOKOWSKI, Effects of impurities and atmosphere on the growth of Cr-doped gadolinium scandium gallium garnet. I, *J. Crystal Growth* **85** (1987), 223–228.
- [23] C. D. BRANDLE and A. J. VALENTINO, Czochralski growth of rare earth gallium garnets, *J. Crystal Growth* **12** (1972), 3–8.
- [24] S. BRANDON and J. J. DERBY, Heat transfer in vertical Bridgman growth of oxides: Effects of conduction, convection, and internal radiation, *J. Crystal Growth* **121** (1992), 473–494.
- [25] I. BRANSKY and A. Z. HED, Thermogravimetric determination of the composition-oxygen partial pressure diagram of wustite (Fe_{1-y}O), *J. Am. Ceram. Soc.* **51** (1968), 231–232.
- [26] R. BRDIČKA, *Grundlagen der Physikalischen Chemie*, Deutscher Verlag der Wissenschaften, Berlin, 1961.
- [27] J. C. BRICE, *The Growth of Crystals from Liquids*, North-Holland, Amsterdam, London, 1973.
- [28] J. C. BRICE, T. M. BRUTON, O. F. HILL, and P. A. C. WHIFFIN, The Czochralski growth of $\text{Bi}_{12}\text{SiO}_{20}$ crystals, *J. Crystal Growth* **24/25** (1974), 429–431.
- [29] P. W. BRIDGMAN, The compressibility of thirty metals as a function of pressure and temperature, *Proc. Amer. Acad. Arts Sci.* **58** (1923), 165–242.
- [30] P. W. BRIDGMAN, Certain physical properties of single crystals of tungsten, antimony, bismuth, tellurium, cadmium, zinc, and tin, *Proc. Amer. Acad. Arts Sci.* **60** (1925), 303–383.

- [31] F. J. BRUNI, *Gadolinium gallium garnet*, pp. 53–70, Springer, Berlin/Heidelberg/New York, 1978.
- [32] E. N. BUNTING, Phase equilibria in the system $\text{Al}_2\text{O}_3\text{--Cr}_2\text{O}_3$, *J. Res. Natl. Bur. Stand. (U.S.)* **6** (1931), 947–949.
- [33] J. BURMEISTER, Schmelzen von Zinkoxyd durch Hochfrequenzerhitzung, *Phys. Stat. Sol. (b)* **10** (1965), K1–K2.
- [34] J. BURMEISTER, Kristallzüchtung von Wüstit, Fe_{1-x}O , *Mat. Res. Bull.* **1** (1966), 17–26.
- [35] J. A. BURTON, R. C. PRIM, and W. P. SLICHTER, The distribution of solute in crystals grown from the melt. Part I. Theoretical, *J. Chem. Phys.* **21** (1953), 1987–1991.
- [36] J. R. CARRUTHERS, *Crystal Growth from the Melt*, New York – London, 1975.
- [37] J. R. CARRUTHERS, Flow transitions and interface shapes in the Czochralski growth of oxide crystals, *J. Crystal Growth* **36** (1976), 212–214.
- [38] L. CASTELLIZ, W. DE SUTTER, and F. HALLA, Über den Zerfall der Wüstit-Phase, *Monatshefte F. Chemie* **85** (1954), 487–490.
- [39] V. I. CHANI, A. YOSHIKAWA, H. MACHIDA, T. SATOH, and T. FUKUDA, Growth of $\text{Tb}_3\text{Ga}_5\text{O}_{12}$ fiber and bulk crystals using micro-pulling-down apparatus, *J. Crystal Growth* **210** (2000), 663–669.
- [40] W. K. CHEN and N. L. PETERSON, Effect of the deviation from stoichiometry on cation self-diffusion and isotope effect in wüstite, Fe_{1-x}O , *J. Phys. Chem. Solids* **36** (1975), 1097–1103.
- [41] B. COCKAYNE, The melt growth of oxide and related single crystals, *J. Crystal Growth* **42** (1977), 413–426.
- [42] B. COCKAYNE, M. CHESSWAS, and D. B. GASSON, Single-crystal growth of sapphire, *J. Mater. Science* **2** (1967), 7–11.

-
- [43] B. COCKAYNE, M. CHESSWAS, and D. B. GASSON, Facetting and optical perfection in Czochralski grown garnets and ruby, *J. Mater. Sc.* **4** (1969), 450–456.
- [44] R. COLLONGUES, Nonstoichiometry in oxides, *Progr. Crystal Growth Charact.* **25** (1992), 203–240.
- [45] J. CZOCHRALSKI, Ein neues Verfahren zur Messung der Kristallisationsgeschwindigkeit der Metalle, *Zeitschr. Phys. Chemie* **92** (1918), 219–221.
- [46] L. S. DARKEN and R. W. GURRY, The system iron–oxygen. I. The wüstite field and related equilibria, *J. Am. Chem. Soc.* **45** (1945), 1398–1412.
- [47] L. S. DARKEN and R. W. GURRY, The system iron–oxygen. II. Equilibrium and thermodynamics of liquid oxide and other phases, *J. Am. Chem. Soc.* **68** (1946), 798–816.
- [48] S. DEGTEROV and A. D. PELTON, Critical evaluation and optimization of the thermodynamic properties and phase diagrams of the CrO–Cr₂O₃, CrO–Cr₂O₃–Al₂O₃, and CrO–Cr₂O₃–CaO systems, *J. Phase Equilibria* **16** (1996), 476–487.
- [49] J. J. DERBY, L. J. ATHERTON, and P. M. GRESHO, An integrated process model for the growth of oxide crystals by the Czochralski method, *J. Crystal Growth* **97** (1989), 792–826.
- [50] J. J. DERBY and Q. XIAO, Some effects of crystal rotation on large-scale Czochralski oxide growth: Analysis via a hydrodynamic thermal-capillary model, *J. Crystal Growth* **113** (1991), 575–586.
- [51] R. R. DILS, G. W. MARTIN, and R. A. HUGGINS, Chromium distribution in synthetic ruby crystals, *Appl. Phys. Lett.* **1** (1962), 75–76.
- [52] E. R. DOBROVINSKAYA, L. A. LYTVYNOV, and V. PISHCHIK, Sapphire – material, manufacturing, applications, in *Sapphire*, Springer, New York, 2009.

- [53] T. DUFFAR, P. BOITON, P. DUSSERRE, and J. ABADIE, Crucible de-wetting during Bridgman growth in microgravity. II. Smooth crucibles, *J. Crystal Growth* **179** (1997), 397–409.
- [54] D. EHRENTAUT, H. SATO, Y. KAGAMITANI, H. SATO, A. YOSHIKAWA, and T. FUKUDA, Solvothermal growth of ZnO, *Progr. Crystal Growth Charact. Mater.* **52** (2006), 280–335.
- [55] K. EICKHOFF and K. GÜRS, Tiegfreeses Zonenschmelzen von Rubinkristallen durch Aufheizen der Schmelzzone mittels Laser, *J. Crystal Growth* **6** (1969), 21–25.
- [56] J. J. FAVIER and L. O. WILSON, A test of the boundary layer model in unsteady Czochralski growth, *J. Crystal Growth* **58** (1982), 103–110.
- [57] Y. W. FEI and S. K. SAXENA, A thermochemical data base for phase equilibria in the system Fe–Mg–Si–O at high pressure and temperature, *Phys. Chem. Minerals* **13** (1986), 311–324.
- [58] R. S. FEIGELSON, 50 years of progress in crystal growth, *J. Crystal Growth* **264** (2004), XI–XVI.
- [59] K. FISCHER and E. SINN, On the preparation of ZnO single crystals, *Cryst. Res. Technol.* **16** (1981), 689–694.
- [60] V. J. FRATELLO and C. D. BRANDLE, Physical properties of a $Y_3Al_5O_{12}$ melt, *J. Crystal Growth* **128** (1993), 1006–1010.
- [61] O. FRITSCH, Elektrisches und optisches Verhalten von Halbleitern. X Elektrische Messungen an Zinkoxyd, *Annalen der Physik* **414** (1935), 375–401.
- [62] Z. GAŁĄZKA, S. GANSCHOW, P. REICHE, and R. UECKER, Experimental study of interface inversion of $Tb_3Sc_xAl_{5-x}O_{12}$ single crystals grown by the Czochralski method, *Cryst. Res. Technol.* **37** (2002), 407–413.
- [63] S. GANSCHOW, D. KLIMM, B. M. EPELBAUM, A. YOSHIKAWA, T. DORSCHER, and T. FUKUDA, Growth conditions and composition of terbium

- aluminum garnet single crystals grown by the micro pulling down technique, *J. Crystal Growth* **225** (2001), 454–457.
- [64] S. GANSCHOW, P. REICHE, M. ZIEM, and R. UECKER, Controlling the axial temperature gradient in inductively heated Czochralski systems, *Cryst. Res. Technol.* **38** (2003), 42–46.
- [65] J. P. GARANDET, Microsegregation in crystal growth from the melt: An analytical approach, *J. Crystal Growth* **131** (1993), 431–438.
- [66] R. A. GIDDINGS and R. S. GORDON, Review of oxygen activities and phase boundaries in wüstite as determined by electromotive-force and gravimetric methods, *J. Am. Ceram. Soc.* **56** (1973), 111–116.
- [67] B. GLEESON, S. M. M. HADAVI, and D. J. YOUNG, Isothermal transformation behavior of thermally-grown wüstite, *Materials at High Temperatures* **17** (2000), 311–319.
- [68] J. G. GRABMAIER, Die Schmelzfilmdicke bei der Rubin-Synthese nach Verneuil und ihr Einfluss auf die Kristallperfektion, *J. Crystal Growth* **5** (1969), 105–110.
- [69] K. GRASZA, P. SKUPIŃSKI, A. MYCIELSKI, E. ŁUSAKOWSKA, and V. DOMUKHOVSKI, ZnO bulk growth in hydrogen atmosphere, *J. Crystal Growth* **310** (2008), 1823–1826.
- [70] D. C. HARRIS, A century of sapphire crystal growth, in *Proceedings of the 10th DoD Electromagnetic Windows Symposium*, Norfolk, Virginia, May 2004.
- [71] M. HAYAKAWA, J. B. COHEN, and T. B. REED, Measurement of the lattice parameter of wüstite at high temperatures, *J. Am. Ceram. Soc.* **55** (1972), 160–164.
- [72] A. HAYES and J. CHIPMAN, Mechanism of solidification and segregation in a low-carbon rimming-steel ingot, *Trans. AIME* **139** (1939), 85–125.
- [73] R. HELBIG, Über die Züchtung von grösseren reinen und dotierten ZnO-Kristallen aus der Gasphase, *J. Crystal Growth* **15** (1972), 25–31.

- [74] A. HOFFMANN, Der Zerfallsmechanismus des Wüstits Fe_{1-x}O unterhalb 570°C , *Z. Elektrochemie* **63** (1959), 207–213.
- [75] Y. P. HONG, D. G. CHEN, Z. B. ZHAN, X. Z. CHEN, P. W. LV, F. B. YAN, F. HUANG, and J. K. LIANG, Subsolidus phase relations in the system $\text{ZnO-P}_2\text{O}_5\text{-MoO}_3$, *J. Alloys Comp.* **482** (2009), 49–52.
- [76] B. ILSCHNER and E. MLITZKE, Ausscheidungskinetik in wüstit (Fe_{1-x}O), *Acta Metallurgica* **13** (1965), 855–867.
- [77] INTERNATIONAL CENTRE FOR DIFFRACTION DATA, Powder Diffraction File, PDF-2, Release 2014 RDB, 2014.
- [78] R. JEANLOZ, The nature of the Earth’s core, *Ann. Rev. Earth Planet. Sc.* **18** (1990), 357–386.
- [79] R. JEANLOZ and T. LAY, Der Grenzbereich zwischen Erdkern und Erdmantel, *Spektr. D. Wiss.* **7/1993** (1993), 48–55.
- [80] L. N. JI, J. B. LI, J. K. LIANG, Y. H. L. B. J. SUN, J. Y. ZHANG, and G. H. RAO, Phase relations and flux research for ZnO crystal growth in the $\text{ZnO-B}_2\text{O}_3\text{-P}_2\text{O}_5$ system, *J. Alloys Comp.* **459** (2008), 481–486.
- [81] L. N. JI, J. B. LI, J. LUO, J. K. LIANG, Y. H. LIU, J. Y. ZHANG, and G. H. RAO, Phase relations and flux research for zinc oxide crystal growth in the $\text{ZnO-K}_2\text{O-P}_2\text{O}_5$ system, *J. Alloys Comp.* **470** (2009), 336–339.
- [82] P. KAPITZA, The study of the specific resistance of bismuth crystals and its change in strong magnetic fields and some allied problems, *Proc. Royal Soc. London A* **119** (1928), 358–442.
- [83] T. KATSURA, B. IWASAKI, S. KIMURA, and S. AKIMOTO, High-pressure synthesis of the stoichiometric compound FeO , *J. Chem. Phys.* **47** (1967), 4559–4560.
- [84] B. KESZEI, J. PAITZ, J. VANDLIK, and A. SÜVEGES, Control of nd and cr concentrations in $\text{Nd,Cr:Gd}_3\text{Ga}_5\text{O}_{12}$ single crystals grown by Czochralski method, *J. Crystal Growth* **226** (2001), 95–100.

-
- [85] T. KITASHIMA, L. LIU, K. KITAMURA, and K. KAKIMOTO, Numerical analysis of continuous charge of lithium niobate in a double-crucible Czochralski system using the accelerated crucible rotation technique, *J. Crystal Growth* **266** (2004), 109–116.
- [86] N. KOBAYASHI, Hydrodynamics in Czochralski growth-computer analysis and experiments, *J. Crystal Growth* **52** (1981), 425–434.
- [87] F. KOCH and J. B. COHEN, The defect structure of Fe_{1-x}O , *Acta Cryst.* **25** (1969), 275–287.
- [88] J. KVAPIL, B. PERNER, and J. KVAPIL, The influence of the quality of ruby on the parameters of the q-switched laser, *Czech. J. Phys.* **28** (1978), 465–471.
- [89] J. KVAPIL and J. K. B. PERNER, Verteilung von Aktivatoren in Laser-Kristallen, *Cryst. Res. Technol.* **9** (1974), 503–510.
- [90] S. KYROPOULOS, Ein Verfahren zur Herstellung großer Kristalle, *Z. Anorg. Allg. Chemie* **154** (1926), 308–313.
- [91] W. E. LANGLOIS, Digital simulation of Czochralski bulk flow in microgravity, *J. Crystal Growth* **48** (1980), 25–28.
- [92] R. A. LAUDISE and A. A. BALLMAN, Hydrothermal synthesis of zinc oxide and zinc sulfide, *J. Phys. Chem.* **64** (1960), 688–691.
- [93] R. A. LAUDISE and A. J. C. E. D. KOLB, Hydrothermal growth of large sound crystals of zinc oxide, *J. Am. Ceram. Soc.* **47** (1964), 9–12.
- [94] N. I. LEONYUK, A. V. LYUTIN, V. V. MALTSEV, S. N. BARILO, G. L. BYCHKOV, L. A. KURNEVICH, G. A. EMELCHENKO, V. M. MASALOV, and A. A. ZHOKHOV, Growth and morphology of ruby crystals with unusual chromium concentration, *J. Crystal Growth* **280** (2005), 551–556.
- [95] R. L. LEVIN and J. B. WAGNER, JR., Lattice-parameter measurements of undoped and chromium-doped wustite, *Trans. AIME* **236** (1966), 516–519.

- [96] R. C. LINARES, Properties and growth of flux ruby, *J. Phys. Chem. Solids* **26** (1965), 1817–1818.
- [97] D. C. LOOK, D. C. REYNOLDS, J. R. SIZELOVE, R. L. JONES, C. W. LITTON, G. CANTWELL, and W. C. HARSCH, Electrical properties of bulk ZnO, *Solid State Comm.* **105** (1998), 399–401.
- [98] Y. L. LU, Y. Q. LU, X. F. CHENG, G. P. LUO, C. C. XUE, and N. B. MING, Formation mechanism for ferroelectric domain structures in a LiNbO₃ optical superlattice, *Appl. Phys. Lett.* **68** (1996), 2642–2644.
- [99] D. MAIER, *Segregation effects in single-crystal fibers grown by the micro-pulling-down method*, Ph.D. thesis, Humboldt-Universität zu Berlin, Mathematisch-Naturwissenschaftliche Fakultät I, Berlin, 2009.
- [100] D. MAIER, D. RHEDE, R. BERTRAM, D. KLIMM, and R. FORNARI, Dopant segregations in oxide single-crystal fibers grown by the micro-pulling-down method, *Opt. Mater.* **30** (2007), 11–14.
- [101] T. H. MAIMAN, Optical and microwave-optical experiments in ruby, *Phys. Rev. Lett.* **4** (1960), 564–566.
- [102] T. H. MAIMAN, Stimulated optical radiation in ruby, *Nature* **187** (1960), 493–494.
- [103] M. MARUYAMA, Ruby crystals grown by the Czochralski technique, *Jap. J. Appl. Phys.* **5** (1966), 1026–1028.
- [104] D. C. MILLER, A. J. VALENTINO, and L. K. SHICK, The effect of melt flow phenomena on the perfection of Czochralski grown gadolinium gallium garnet, *J. Crystal Growth* **44** (1978), 121–134.
- [105] Y. MIMURA, Y. OKAMURA, Y. KOMAZAWA, and C. OTA, Growth of fiber crystals for infrared optical waveguides, *Jap. J. Appl. Phys.* **19** (1980), L269.
- [106] N. B. MING, J. F. HONG, and D. FENG, The growth striations and ferroelectric domain structures in Czochralski-grown LiNbO₃ single crystals, *J. Mater. Sc.* **17** (1982), 1663–1670.

-
- [107] S. MIYAZAWA, Fluid-flow analysis in a Czochralski simulation, *J. Crystal Growth* **53** (1981), 636–638.
- [108] S. MIYAZAWA and S. KONDO, Preparation of paratellurite TeO₂, *Mat. Res. Bull.* **8** (1973), 1215–1221.
- [109] S. MROWEC and A. PODGÓRECKA, Defect structure and transport properties of non-stoichiometric ferrous oxide, *J. Mater. Sc.* **22** (1987), 4181–4189.
- [110] A. MUAN, Equilibrium relations in systems containing chromium oxide, with a bearing on refractory corrosion in slagging coal gasifiers, *High Temp. – High Press.* **16** (1982), 654–660.
- [111] R. NACKEN, Kristallzüchtungsapparate, *Z. Instrumentenkunde* **36** (1916), 12–20.
- [112] K. NASSAU, "Reconstructed" or "Geneva" ruby, *J. Crystal Growth* **5** (1969), 338–344.
- [113] K. NASSAU, Dr. A. V. L. Verneuil: The man and the method, *J. Crystal Growth* **13–14** (1972), 12–18.
- [114] K. NASSAU and L. G. VAN UITERT, Preparation of large calcium-tungstate crystals containing paramagnetic ions for maser applications, *J. Appl. Phys.* **31** (1960), 1508.
- [115] J. NAUSE and B. NEMETH, Pressurized melt growth of ZnO boules, *Semicond. Sci. Technol.* **20** (2005), S45–S48.
- [116] J. E. NAUSE, ZnO broadens the spectrum, *III-Vs Review* **12** (1999), 28–31.
- [117] D. F. NELSON and J. P. REMEIKA, Laser action in a flux-grown ruby, *J. Appl. Phys.* **35** (1964), 522–529.
- [118] D. NGUYEN, Méthode de dopage au chrome dans la préparation du rubis hydrothermal, *J. Crystal Growth* **12–13** (1972), 545–548.
- [119] J. W. NIELSEN and E. F. DEARBORN, The growth of large single crystals of zinc oxide, *J. Phys. Chem.* **64** (1960), 1762–1763.

- [120] J. M. NTEP, M. BARBÉ, G. COHEN-SOLAL, F. BAILLY, A. LUSSON, and R. TRIBOULET, ZnO growth by chemically assisted sublimation, *J. Crystal Growth* (1998), 1026–1030.
- [121] J. M. NTEP, S. S. HASSANI, A. LUSSON, A. TROMSON-CARLI, D. BALLETAUD, G. DIDIER, and R. TRIBOULET, ZnO growth by chemical vapour transport, *J. Crystal Growth* **207** (1999), 30–34.
- [122] J. R. O’CONNOR, P. S. SCHAFFER, and R. A. BRADBURY, Laser properties of vapor-grown ruby, *Appl. Phys. Lett.* **8** (1966), 336–337.
- [123] S. O’HARA, Some interface growth features of Czochralski sapphire crystals, *J. Crystal Growth* **2** (1968), 145–148.
- [124] E. OHSHIMA, H. OGINO, I. NIIKURA, K. MAEDA, M. SATO, M. ITO, and T. FUKUDA, Growth of the 2-in-size bulk ZnO single crystals by the hydrothermal method, *J. Crystal Growth* **260** (2004), 166–170.
- [125] A. OHTOMO, M. KAWASAKI, T. KOIDA, K. MASUBUCHI, H. KOINUMA, Y. SAKURAI, Y. YOSHIDA, T. YASUDA, and Y. SEGAWA, $Mg_xZn_{1-x}O$ as a II–VI widegap semiconductor alloy, *Appl. Phys. Lett.* **72** (1998), 2466–2468.
- [126] Y. OKANO, A. HATANO, and A. HIRATA, Natural and marangoni convections in a floating zone, *J. Chem. Eng. Jpn.* **22** (1989), 385–388.
- [127] Y. I. OL’SHANSKII and V. K. SHLEPOV, The system Cr–Cr₂O₃, *Dokl. Akad. Nauk SSSR* **91** (1953), 561–564.
- [128] A. G. OSTROGORSKY and G. MÜLLER, A model of effective segregation coefficient accounting for convection in the solute layer at the growth interface, *J. Crystal Growth* **121** (1992), 587–598.
- [129] N. OTSUKA, T. DOI, Y. HIDAKA, Y. HIGASHIDA, Y. MASAKI, N. MIZUI, and M. SATO, In-situ measurements of isothermal wüstite transformation of thermally grown FeO scale formed on 0.048 mass% Fe by synchrotron radiation in air, *ISIJ International* **53** (2013), 286–293.

-
- [130] A. E. PALADINO and B. D. ROVER, Czochralski growth of sapphire, *J. Am. Ceram. Soc.* **47** (1964), 465.
- [131] O. PÄTZOLD, K. JENKNER, S. SCHOLZ, and A. CRÖLL, Detached growth behaviour of 2-in germanium crystals, *J. Crystal Growth* **277** (2005), 37–43.
- [132] A. D. PELTON, Thermodynamics and phase diagrams of materials, in *Materials science and technology, vol. 5* (P. HAASEN, ed.), VCH, Weinheim, 1991, pp. 1–73.
- [133] B. PERNER, J. KVAPIL, J. KVAPIL, and Z. PLEŠTIL, The influence of protective atmosphere on the growth of ruby single crystals by Czochralski method, *J. Crystal Growth* **52** (1981), 552–555.
- [134] A. G. PETROSYAN and K. S. BAGDASAROV, Faceting in stockbarger grown garnets, *J. Crystal Growth* **34** (1976), 110–112.
- [135] P. REICHE, B. HERMONEIT, and D. SCHULTZE, A modified heater system for rf-Czochralski equipments, *Cryst. Res. Technol.* **20** (1985), 845–849.
- [136] A. E. RINGWOOD, Composition of the core and implications for origin of the Earth, *Geochem. Journal* **11** (1977), 111–136.
- [137] F. ROSENBERGER and G. MÜLLER, Interfacial transport in crystal growth, a parametric comparison of convective effects, *J. Crystal Growth* **65** (1983), 91–104.
- [138] W. L. ROTH, Defects in the crystal and magnetic structures of ferrous oxide, *Acta Cryst.* **13** (1960), 140–149.
- [139] J. J. RUBIN and L. G. VAN UITERT, Growth of sapphire and ruby by the Czochralski technique, *Mat. Res. Bull.* **1** (1966), 211–214.
- [140] P. RUDOLPH and T. FUKUDA, Fiber crystal growth from the melt, *Cryst. Res. Technol.* **34** (1999), 3–40.
- [141] P. RUDOLPH, A. YOSHIKAWA, and T. FUKUDA, Studies on meniscus and diameter stability during the growth of fiber crystals by the micro-pulling-down method, *Jap. J. Appl. Phys.* **39** (2000), 5966–5969.

- [142] P. A. SACKINGER, R. A. BROWN, and J. J. DERBY, A finite element method for analysis of fluid flow, heat transfer and free interfaces in Czochralski crystal growth, *Int. J. Heat Mass Transfer* **9** (1989), 453–492.
- [143] M. SAITO, Growth process of gas bubble in ruby single crystals by floating zone method, *J. Crystal Growth* **74** (1986), 385–390.
- [144] G. SAMANTA, A. YECKEL, P. DAGGOLU, H. FANG, E. D. BOURRET-COURCHESNE, and J. J. DERBY, Analysis of limits for sapphire growth in a micro-pulling-down system, *J. Crystal Growth* **335** (2011), 148–159.
- [145] N. SCHÄFER, T. YAMADA, K. SHIMAMURA, H. J. KOH, and T. FUKUDA, Growth of $\text{Si}_x\text{Ge}_{1-x}$ crystals by the micro-pulling-down method, *J. Crystal Growth* **166** (1996), 675–679.
- [146] E. SCHAROWSKY, Optische und elektrische Eigenschaften von ZnO-Einkristallen mit Zn-überschuß, *Z. Physik* **135** (1953), 318–330.
- [147] H. J. SCHEEL, Historical aspects of crystal growth technology, *J. Crystal Growth* **211** (2000), 1–12.
- [148] E. SCHEIL, Bemerkungen zur Schichtbildung, *Z. Metallkunde* **34** (1942), 70–72.
- [149] H. SCHMALZRIED and A. NAVROTSKY, *Festkörperthermodynamik, Chemie des festen Zustandes*, 2 ed., Verlag Chemie, Weinheim, 1975.
- [150] D. SCHULZ, R. BERTRAM, D. KLIMM, T. SCHULZ, and E. THIEDE, Segregation of Mg in $\text{Zn}_{1-x}\text{Mg}_x\text{O}$ single crystals grown from the melt, *J. Crystal Growth* **334** (2011), 118–121.
- [151] D. SCHWABE, R. UECKER, M. BERNHAGEN, and Z. GALAZKA, An analysis of and a model for spiral growth of Czochralski-grown oxide crystals with high melting point, *J. Crystal Growth* **335** (2011), 138–147.
- [152] E. R. SEGNET and A. E. HOLLAND, The system MgO-ZnO-SiO_2 , *J. Am. Ceram. Soc.* **48** (1965), 409–413.

-
- [153] W. SEIFERT, Zur Züchtung von Rubinen für Laser nach einem verbesserten Verneuil-Verfahren, *J. Crystal Growth* **12** (1972), 17–20.
- [154] G. P. SINGH, S. RAM, J. ECKERT, and H. J. FECHT, Synthesis and morphological stability in CrO₂ single crystals of a half-metallic ferromagnetic compound, *J. Phys.: Conf. Series* **144** (2009), 012110.
- [155] C. SONG, Y. HANG, C. T. XIA, J. XU, and G. Q. ZHOU, Characteristics of large-sized ruby crystal grown by temperature gradient technique, *Opt. Mater.* **27** (2005), 699–703.
- [156] S. STØLEN, R. GLÖCKNER, and F. GRØNVOLD, Nearly stoichiometric iron monoxide formed as a metastable intermediate in a two-stage disproportionation of quenched wüstite. thermodynamic and kinetic aspects, *Thermochimica Acta* **256** (1995), 91–106.
- [157] B. SUNDMANN, An assessment of the Fe–O system, *J. Phase Equilibria* **12** (1991), 127–140.
- [158] T. SUREK, Theory of shape stability in crystal growth from the melt, *J. Appl. Phys.* **47** (1976), 4384.
- [159] T. SUREK, B. CHALMERS, and A. I. MLAVSKY, The edge-defined film-fed growth of controlled shape crystals, *J. Crystal Growth* **42** (1977), 453–465.
- [160] T. SUREK, S. R. CORIELL, and B. CHALMERS, The growth of shaped crystals from the melt, *J. Crystal Growth* **50** (1980), 21–32.
- [161] K. TAKAGI, T. FUKAZAWA, and M. ISHII, Inversion of the direction of the solid-liquid interface on the Czochralski growth of GGG crystals, *J. Crystal Growth* **32** (1976), 89–94.
- [162] E. TAKAYAMA and N. KIMIZUKA, Thermodynamic properties and subphases of wüstite field determined by means of thermogravimetric method in the temperature range of 1100°–1300°c, *J. Electrochem. Soc.* **127** (1980), 970–976.

- [163] V. A. TATARCHENKO, Capillary shaping in crystal growth from melts: I. Theory, *J. Crystal Growth* **37** (1977), 272–284.
- [164] V. A. TATARCHENKO and E. A. BRENER, Crystallization stability during capillary shaping: I. General theory of capillary and thermal stability, *J. Crystal Growth* **50** (1980), 33–44.
- [165] V. A. TATARCHENKO and G. A. SATUNKIN, Capillary shaping in crystal growth from melts. II. Experimental results for sapphire, *J. Crystal Growth* **37** (1977), 285–288.
- [166] W. A. TILLER, K. A. JACKSON, J. W. RUTTER, and B. CHALMERS, The redistribution of solute atoms during the solidification of metals, *Acta Metallurgica* **1** (1953), 428–437.
- [167] K. TOKUMITSU and T. NASU, Preparation of lamellar structured α -Fe/Fe₃O₄ complex particle by thermal decomposition of wüstite, *Scripta Materialia* **44** (2001), 1421–1424.
- [168] T. TSUKADA, M. HOZAWA, and N. IMAISHI, Global analysis of heat transfer in Cz crystal growth of oxide, *J. Chem. Eng. Japan* **27** (1994), 25–31.
- [169] S. UDA, J. KON, K. SHIMAMURA, and T. FUKUDA, Analysis of ge distribution in Si_{1-x}Ge_x single crystal fibers by the micro-pulling down method, *J. Crystal Growth* **167** (1996), 64–73.
- [170] S. UDA, J. KON, K. SHIMAMURA, J. ICHIKAWA, K. INABA, and T. FUKUDA, Interface field-modified solute partitioning during Mn:LiNbO₃ crystal fiber growth by micro-pulling down method, *J. Crystal Growth* **182** (1997), 403–415.
- [171] R. UECKER, B. VELICKOV, D. KLIMM, R. BERTRAM, M. BERNHAGEN, M. RABE, M. ALBRECHT, R. FORNARI, and D. G. SCHLOM, Properties of rare-earth scandate single crystals (Re = Nd–Dy), *J. Crystal Growth* **310** (2008), 2649–2658.

- [172] R. UECKER, H. WILKE, D. G. SCHLOM, B. VELICKOV, P. REICHE, A. POLITY, M. BERNHAGEN, and M. ROSSBERG, Spiral formation during Czochralski growth of rare-earth scandates, *J. Crystal Growth* **295** (2006), 84–91.
- [173] T. VOLK and M. WÖHLECKE, *Lithium niobate: Defects, photorefraction and ferroelectric switching*, Springer, Berlin Heidelberg, 2009.
- [174] A. C. WALKER, Hydrothermal synthesis of quartz crystals, *J. Am. Ceram. Soc.* **36** (1953), 250–256.
- [175] B. WANG and M. J. CALLAHAN, Hydrothermal growth and photoluminescence of $\text{Zn}_{1-x}\text{Mg}_x\text{O}$ alloy crystals, *Crystal Growth & Design* **6** (2006), 1256–1260.
- [176] Y. WANG, L. L. REGEL, and W. R. WILCOX, Influence of contact angle, growth angle and melt surface tension on detached solidification of InSb, *J. Crystal Growth* **209** (2000), 175–180.
- [177] B. M. WANKLYN, The growth of ZnO crystals from phosphate and vanadate fluxes, *J. Crystal Growth* **7** (1970), 107–108.
- [178] D. F. WEIRAUCH and R. KUNG, The hydrothermal growth of Al_2O_3 in HCl solutions, *J. Crystal Growth* **19** (1973), 139–140.
- [179] P. A. C. WHIFFIN, T. M. BRUTON, and J. C. BRICE, Simulated rotational instabilities in molten bismuth silicon oxide, *J. Crystal Growth* **32** (1976), 205–210.
- [180] K. T. WILKE and J. BOHM, *Kristallzüchtung*, Deutscher Verlag der Wissenschaften, Berlin, 1988.
- [181] L. O. WILSON, A new look at the Burton, Prim, and Slichter model of segregation during crystal growth from the melt, *J. Crystal Growth* **44** (1978), 371–376.

- [182] L. O. WILSON, On interpreting a quantity in the Burton, Prim and Slichter equation as a diffusion boundary layer thickness, *J. Crystal Growth* **44** (1978), 247–250.
- [183] L. O. WILSON, Analysis of microsegregation in crystals, *J. Crystal Growth* **48** (1980), 363–366.
- [184] Q. XIAO and J. J. DERBY, The role of internal radiation and melt convection in Czochralski oxide growth: Deep interfaces, interface inversion, and spiraling, *J. Crystal Growth* **128** (1993), 188–194.
- [185] Q. XIAO and J. J. DERBY, Heat transfer and interface inversion during the Czochralski growth of yttrium aluminum garnet and gadolinium gallium garnet, *J. Crystal Growth* **139** (1994), 147–157.
- [186] W. YANG, S. S. HULLAVARAD, B. NAGARAJ, I. TAKEUCHI, R. P. SHARMA, T. VENKATESAN, R. D. VISPUTE, and H. SHEN, Compositionally-tuned epitaxial cubic $\text{Mg}_x\text{Zn}_{1-x}\text{O}$ on Si(100) for deepultraviolet photodetectors, *Appl. Phys. Lett.* **82** (2003), 3424–3426.
- [187] D. H. YOON and T. FUKUDA, Characterization of LiNbO_3 micro single crystals grown by the micro-pulling-down method, *J. Crystal Growth* **144** (1994), 201–206.
- [188] D. H. YOON, P. RUDOLPH, and T. FUKUDA, Morphological aspects of potassium lithium niobate crystals with acicular habit grown by the micro-pulling-down method, *J. Crystal Growth* **144** (1994), 207–212.
- [189] D. H. YOON, I. YONENAGA, T. FUKUDA, and N. OHNISHI, Crystal growth of dislocation-free LiNbO_3 single crystals by the micro-pulling-down method, *J. Crystal Growth* **142** (1994), 339–343.
- [190] K. ZIMIK, R. R. CHAUHAN, R. KUMAR, K. MURARI, N. MALHAN, and H. V. THAKUR, Study on the growth of $\text{Nd}^{3+}:\text{Gd}_3\text{Ga}_5\text{O}_{12}$ (Nd:GGG) crystal by the Czochralski technique under different gas flow rates and using different crucible sizes for flat interface growth, *J. Crystal Growth* **363** (2013), 76–79.

Danksagung

Die vorliegende Arbeit wurde am Leibniz-Institut für Kristallzüchtung in der Themengruppe Oxide & Fluoride angefertigt. Für die Unterstützung möchte ich meinen Kolleginnen und Kollegen herzlich danken. Ganz besonderer Dank gilt Herrn PD Dr. habil. Detlef Klimm für zahlreiche Anregungen, Ausführung der Factsage-Rechnungen und stete Bereitschaft zur Diskussion der Ergebnisse. Herrn Dr. Rainer Bertram sei für die nasschemischen Analysen gedankt. Bedanken möchte ich mich bei Herrn Mario Brützam, der mich tatkräftig bei der Czochralski-Züchtung unterstützt hat. Herrn Dr. Detlev Schulz danke ich für die gute Zusammenarbeit bei der Züchtung von Zinkoxid-Einkristallen und die bereitwillige Übernahme eines Teils meiner anderweitigen Verpflichtungen. Herrn Dr.-Ing. Peter Reiche, Herrn Dr. Reinhard Uecker und Frau Margitta Bernhagen danke ich für die Einarbeitung in die Kristallzüchtung und die mir über viele Jahre zuteil gewordene Unterstützung.

Herrn Dipl.-Phys. Albert Kwasniewski und Herrn PD Dr. Martin Schmidtbauer danke ich für Röntgenbeugungsuntersuchungen, Herrn Dipl.-Ing. Jörg Nissen (ZELMI, TU Berlin) für Messungen mit der Elektronenstrahl-Mikrosonde.

Herrn Prof. Dr.-Ing. Matthias Bickermann möchte ich herzlich für die Unterstützung bei der Anfertigung der Dissertation danken. Herrn Prof. Dr. Martin Lerch (Institut für Chemie, TU Berlin) danke ich für die Bereitschaft zur Begutachtung derselben. Mein Dank gilt weiterhin Herrn Prof. Dr. Dietmar Siche für das sorgfältige Korrekturlesen und zahlreiche Hinweise.

Nicht zuletzt möchte ich meiner Frau Elżbieta für ihre stete Ermutigung und Unterstützung dieses Vorhabens und meinem Sohn Felix für die tolle Idee danken.